PROCESS DEVELOPMENT FOR NON-RE, IRON BASED HARD MAGNETIC POWDERS

PER-OLOF ANDERSSON

Master Thesis
Faculty of Engineering at Lund University (LTH)
March - 2014

Supervisor: Björn Skårman, PhD
Examination: Prof. Srinivasan Iyengar, PhD

LUNDS UNIVERSITET
Lunds Tekniska Högskola

ISRN LUTFD2/TFMT --14/5045-- SE

Abstract

An experimental study was performed, aimed at finding a way to produce single crystalline powder of pure $(Fe_{0.7}Co_{0.3})_2B$ with a particle size of 100-200nm. This was done with the ultimate goal of producing a hard magnetic ferrite powder for powder metallurgical production of permanent magnets. For this study, eight different compositions of iron, cobalt and boron were atomized using atomization by water and a gas-water combination atomization (GA/W). The atomization type was found to have a limited impact on the particle morphology and GA/W atomization also showed a slight reduction in the oxygen contents.

X-Ray Diffraction (XRD) was used to characterize the phase composition in conjuncture with Simultaneous Thermal Analysis (STA) and dilatometry to find the temperature of any phase transitions. One of the alloys was also analyzed using XRD, STA and Light Optical Microscopy (LOM) at different stages of milling and heat treatment under different atmospheres so as to determine the best way to treat the powder for crystal growth.

Representatives from all eight alloys was analyzed in a Vibrating Sample Magnetometer (VSM) to produce hysteresis loops and determine the magnetic characteristics. In these analyses the composition, heat treatment and milling was varied in an attempt to discover any dependencies. Two samples that were heat treated for this purpose, were also coated with SiO_2 using tetra-ethyl-orto-silicate (TEOS) in an attempt to hinder sintering normally accompanied with long heat treatments.

A SEM analysis indicated that the grain growth is a slow process but was unable to quantify a growth rate due to a large variance. The equivalent LOM analysis was inconclusive but suggested an estimation of the grain size. These analyses were also used to estimate the number of grains per particle but vary heavily between 10 and 1'000'000.

All but two of the alloys were, with their stoichiometric composition, found to contain >80% Fe_2B with the remainder being FeB. Trace amounts of other phases could exist but was not possible to resolve in the XRD analyses. The remaining two alloys, having a non-stoichiometric composition, were found to contain mostly $(Fe,Co)_3B_2$ (>50%) with the remainder being FeCo. Thus it's concluded that the stoichiometric composition is more beneficial to the project.

Heat treatment of these materials was beneficial in the transformation of (Fe,Co)B into $(Fe,Co)_2B$ regardless if the atmosphere is N_2 or H_2.

A phase transition between an $(Fe,Co)_2B$ type phase and another phase has been detected around $550^{O}C$ using DSC. This is confirmed by phase diagram comparison, reference measurement of pure Fe in DSC and is consistent with DSC of etched samples.

The best hard magnetic properties has been found to be in the least heat treated and least milled G336 sample. Heat treatments and milling both, consistently, showed a deleterious effect on the hard magnetic properties. The heat treatment having this effect remains unexplained but the milling introduced defect in the material that could have acted as nucleation points for magnetic sub-domains.

The SiO_2 coating worked well as a coating to prevent sintering but had a deleterious effect on the magnetic properties of the material. The reasons for this are discussed.

Some of the alloys were found to contain a large fraction of particles containing bubbles, mainly from the water atomizing process. These have not been seen to have any effect on the magnetic properties.

Keywords: Crystalline metals, Magnetic materials, Hard magnetic materials, Electro-magnetic applications, Single crystalline powder, Powder metallurgy, Fe_2B, FeB, Water atomization, Gas/Water atomization, non-RE hard magnetic material,

Acknowledgements

I would like to extend my sincerest thanks to my supervisor Björn Skårman and Hilmar Vidarsson, for their support and encouragement during this project. It's people like you that makes Höganäs AB the great workplace that it is. I would also like to thank Srinivasan Iyengar for his patience and support over the past few years.

There are a few other people at Höganäs AB that deserve some special recognition for accepting me into the fold, showing me the ropes and supporting me in the daily work. People like Jingjing Cai, Eva Dinh, Haike Heinrich and others, too numerous to recount.

A special thanks goes out to Sofia Kontos, Klas Gunnarsson and Martin Sahlberg at the Ångström Laboratory at Uppsala University, for their dedicated work on this project and their aid in my own work, to Mikkel Fought Hansen at Denmark's Technical University, DTU for his assistance with the magnetic measurements and to Sven Lidin at the Depatement of Material Chemistry, LTH for his patient assistance with the understanding of crystallography basics.

Finally I would like to extend my heartfelt thanks to Live Borrebæk for her invaluable support, inspiration and never ending encouragement.

Thank you all!

Nomenclature

P/M	Powder Metallurgical Method
H_c	Coercive field
M_R	Remanent magnetization
M_S	Saturation magnetization
B_R	Residual induction
B_S	Saturation flux density
χ	Magnetic susceptibility
μ_0	Permeability of vacuum
$(BH)_{max}$	Energy product (actual)
$(BH)_{MAX}$	Energy product (theoretical)
RE	Rare Earth metals
GA/W	Gas atomization with water quenching

Contents

1. Introduction

In the 1980-ies the neodymium based magnets where introduced to the world as the culmination of many years of research into strong permanent magnets and were intensively studied for many years. Being so superior in strength, the neodymium magnets quickly took over large market shares and allowed for the advent of new products such as the laptop and is now instrumental in the creation of electric cars. None of the other candidates of the time can match the Nd magnets for field strength and, even today, the NdFeB magnets are regarded as the most ideal magnets.[1]

Over the last couple of decades, however, the world has changed. With the reduction of poverty across the globe and the need for resources that follow industrialization, mineral prices have fluctuated heavily from being relatively low to skyrocketing over night making the price on magnets and all subsequent products unstable.[2] This, combined with the excessive environmental impact from the mineral extraction of Nd, has motivated an upswing for the research into alternative hard magnetic materials that are more cost effective and has a more stable price. Even if the field strength is lower, a significant drop in production cost and a stable mineral price is motivation enough to use a cheaper material so long as it's good enough for the application.

Several studies have pointed out iron – cobalt – boron alloys as interesting materials for magnetic applications.[3-6,24] The anisotropic properties of $(Fe_{(1-x)}Co_x)_2B$ is especially interesting as this makes it a candidate for hard magnetic applications and the possibility of producing it by means of P/M makes it of special interest to Höganäs AB which is the purpose of the pre-study of which this work is a part. A. Iga[5] and M.D. Kuzmin et.al.[24] suggests that x=0.3 would yield the best anisotropy and C. Jo[3] suggests that the best hard magnetic characteristics can be found around x=0.2-0.25. This is thus the composition that is explored in this thesis.

For optimal hard magnetic properties the material must be able to maintain a global (i.e. throughout the finished magnet product) anisotropy in order to maximize the resistance to demagnetization (coercivity), as well as hold a high saturation magnetization so as to make it as strong as possible. To obtain a global magnetocrystalline anisotropy, the material must be prevented from creating magnetic sub-domains that will negate the effects of the anisotropy (*see Theory section*). To accomplish this, the grains of the material should not exceed 100-200nm[7], be mono-crystalline and be electrically insulated from the other grains so as to avoid the nucleation of sub-domains and losses due to eddie currents. The production of near-single-crystalline particles in the correct size range is thus the main focus of this thesis. Heavy emphasis is also placed on the purity of the $(Fe_{(1-x)}Co_x)_2B$ phase.

2. Goals and objectives

As previously stated, the optimal particle size for the creation of a hard magnetic material using P/M is in the range 100-200nm with each particle being a single crystal. Any larger and the particles will begin to form sub-domains that are detrimental to the *stray field* of the material. The main objective of this thesis is to attempt to develop a process for obtaining a powder that is of the correct size range and as close as possible to single-crystalline yet easily handled so as to be adaptable to large scale production.

The strategy is to mill the powder to roughly the correct particle size range and then induce crystal growth by heat treatment. This should allow for large crystals to form and, given enough time, form (near) single crystal particles. A variation of this strategy is also implemented in which the material is heat treated in the furnace under a hydrogen atmosphere, possibly allowing hydrogen to penetrate the grain boundaries making the metal brittle. It is then milled to reduce particle size more efficiently and finally relaxed and heat treated in an attempt to remove crystal strain and obtain a more rapid crystal growth. A second strategy involving Hydrogen Decrepitation Crushing (HDC) was also considered but as FeCoB alloys are not known to form hydrides, this method was rejected.[10]

Another goal of this project (of which this thesis is a part) is to find a way to electrically insulate each grain in the finished product so as to minimize losses due to large eddie currents. Thus a non-conductive coating must be

developed for the powder that will persist through heat treatments so as to prevent sintering as the crystals grow.

The ultimate goal for the magnetic properties for the project has been determined to be a coercivity, H_C, of around 500-1000 kA/m and an energy product, $(BH)_{max}$ of 150 kJ/m^2.[7] While this might not be reached in this thesis, it remains the ultimate goal here as well.

3. Theory

In the following subsections, the theory of the main concepts considered is explained so as to give the reader a quick introduction to the subject.

3.1. Magnetism

For any magnetic field with *magnetic flux density,* **B,** there is a *magnetizing field,* **H,** related through

$$\boldsymbol{B} = \mu_0(\boldsymbol{H} + \boldsymbol{M}) \quad \ldots (1)$$

and can normally be rewritten with the linear equation

$$\boldsymbol{M} = \chi \boldsymbol{H} \quad \ldots (2)$$

where $\boldsymbol{M}$ is the *magnetization*, χ is the *magnetic susceptibility* and μ_0 the *permeability of vacuum*.

There are several types of magnetism in nature. Paramagnetism (*see fig. 1b*), diamagnetism (*see fig. 1a*), ferromagnetism, ferrimagnetism (*see fig. 1c*) and anti-ferromagnetism (*see fig. 1b*) are some examples of the more common ones. Paramagnetism can be defined as a material with positive magnetic susceptibility χ, whereas diamagnetism can be defined as a material with negative susceptibility. Neither of these, however, are relevant for this project as ferromagnetism is what is sought after.

Ferromagnetism cannot be defined by a certain χ but has instead a nonlinear χ and allows for a magnetization **M** to exist without an external magnetizing field **H**. This is what is commonly referred to as permanent magnets. Here the magnetic moments of the atoms within the material are constructively aligned so that they form an external magnetic field often referred to as the *stray field*.

Ferrimagnetism and anti-ferromagnetism are similar in that they both have a magnetic field without the presence of an external magnetizing field but, unlike the ferromagnetic material have anti-aligned magnetic moments that cancel each other out. Ferrimagnetism differs from anti-ferromagnetism in that its magnetic moments do not completely cancel as the magnetic moments within are of varying strength. Another difference is that anit-ferromagnetism, much like paramagnetism, has a constant positive χ whereas ferrimagnetism has a varying χ like ferromagnetism.

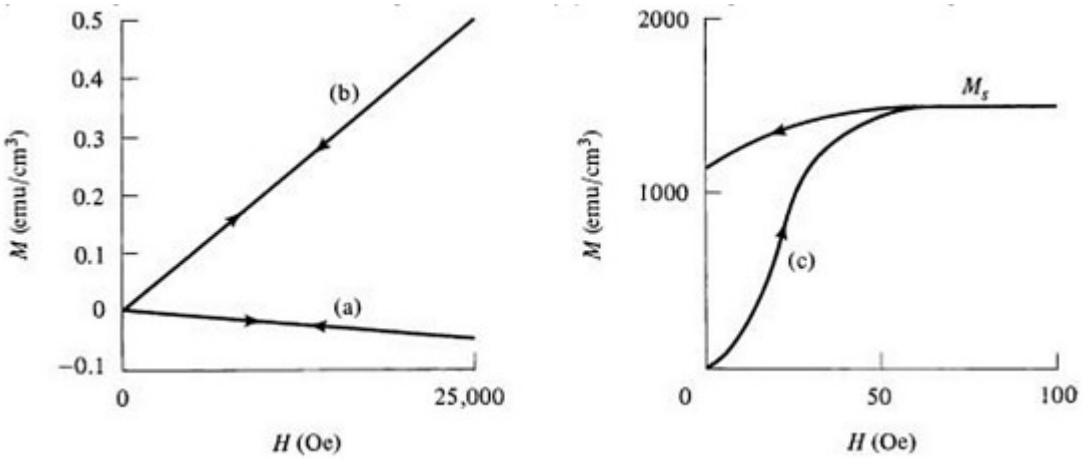

Figure 1: Differences in magnetization behavior, typical for (a) diamagnetic, (b) para- or anti-ferromagnetic and (c) ferro- or ferrimagnetic, materials. [B. D. Cullity & C. D. Graham, Introduction to Magnetic Materials, Wiley (2009), p.14]

Now, for ferromagnets, two different types are commonly defined. Soft and hard magnets, originally so named because of the mechanical properties of magnetic steels. The soft magnet has a magnetization that can easily be reversed by an applied external field whereas the hard magnetic material requires a much stronger external field to be reversed. This attribute is called *coercivity* and is measured in *Gauss*, *G* (cgs), in *Oersted*, *Oe* (cgs), in *Teslas*, *T* (SI) or in *A/m* (SI).

3.1.1. Magnetic domain structure

Within all crystalline metallic materials, there exists regions that have a unified direction of their electron spins. These regions are known as *magnetic domains*. The concept of *magnetic domains* was originally thought of by James Ewing around the turn of the last century. They are defined by Cullity & Graham[8] as

"... a ferromagnet in the demagnetized state is divided into a number of small regions called domains. *Each domain is spontaneously magnetized to the saturation value M_s, but the directions of magnetization of the various domains are such that the specimen as a whole has no net magnetization."*

Adjacent domains are spontaneously aligned in opposite directions and between these regions there are narrow areas called *domain walls*. These are regions of gradually changing magnetization from the magnetization direction of the domain on one side to the direction on the other.

In a ferromagnetic metal the domains align in opposite directions throughout each individual grain in such a way that the domains cancel and the net field remains zero. The direction of the domains depend on the crystallography in that a *magnetocrystalline anisotropy* can be found parallel to the crystallographic directions of the material.[11]

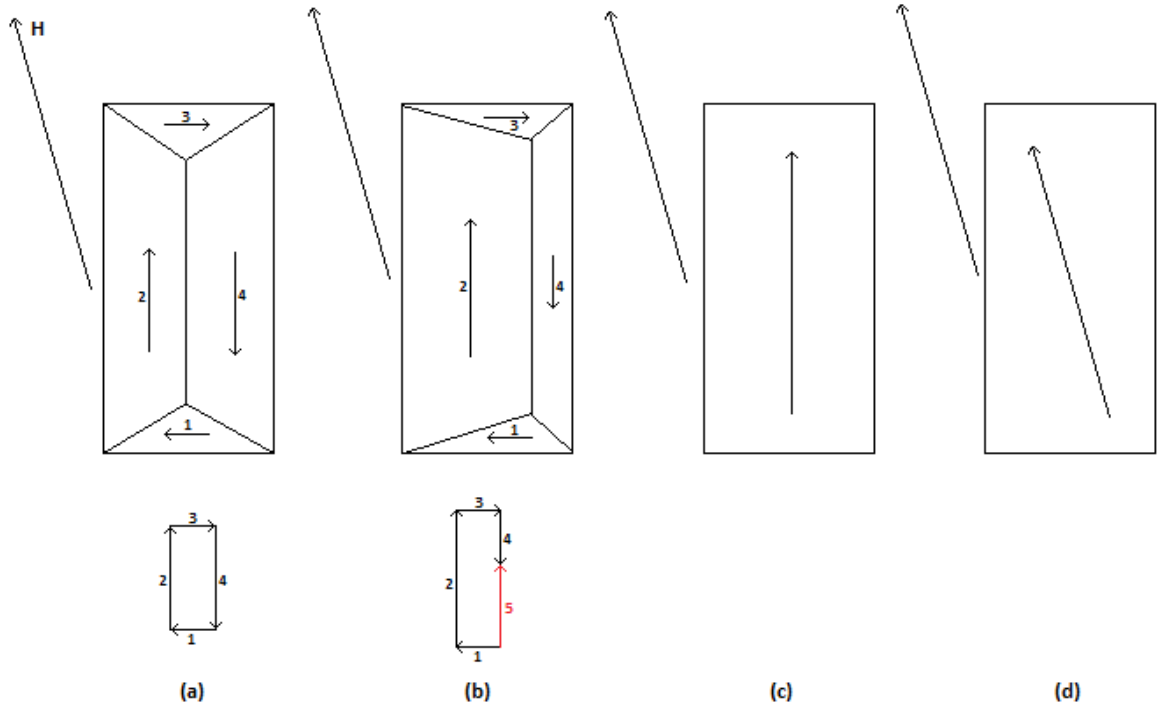

Figure 2: A domain structure in an external field H (a) initially has no resulting stray field. As the domain walls move (b) to find the lowest energy state, a dominant domain emerges and gives rise to a stray field. This domain eventually takes over completely (c) and then proceeds to rotate (d) to align perfectly with the external field.

In order to obtain a microstructure, in which each grain is so small that they spontaneously only contain a single

domain, the grains must have a diameter on the order of a domain wall width which are on the order of 10-100nm. [11] This can be strayed from to some extent as the domain wall should be the minor part of the grains domain structure and theoretical calculations place the maximum domain diameter at ~200nm.

3.1.2. Magnetic measurements

A hysteresis loop is usually measured as a means of finding, among other things, the coercivity. It is measured by applying a gradually increasing magnetizing field until the sample reaches saturation and measuring the induced magnetic moment, m [A m²] (or [emu] in cgs). The magnetization $\boldsymbol{M}$ [A/m] is defined as the magnetic moment per unit volume and the *specific magnetic moment*, σ [Am²/kg], is defined as the magnetic moment per unit mass.

Initially, a ferromagnetic material produces no external field, or *stray field*, as a result of a majority of the domains canceling. When an external field $\boldsymbol{H}$ *is* applied to the material, however, the domain walls *(*that separate the domains) begin to shift so that the domains aligned with the applied field grow at the expense of domains with the opposite direction.

When this process is completed, some misalignement will most likely remain due to the *easy axis* of the domains that remain are somewhat misaligned with the applied field. With a growing external field, the magnetic domains will rotate from their *easy axis* and align with the applied field. This point is known as the *saturation magnetization*, M_S.

When the saturation magnetization is reached, the magnetizing field is reversed and the material begins to reverse its alignment. First, the rotation of the domains from their *easy axis* will return as the easy axis represents a lower energy state. When the applied field is removed, the rotation is lost completely and what remains is the domain wall movement. As it requires an application of energy to reinstate the domain walls, the magnetization remaining at this point is defined as the *remanent magnetization*, M_R.

The applied field will then begin to reverse and the domain walls begin to appear again. At the point the domains again cancel each other out and the magnetization is zero, the domains begin to grow again but this time in the opposite derection as a stronger reverse field is applied. The reverse field required for this is called the *coercivity* or *coercive field*, H_C. The magnetization will then go through the reverse process and magnetize in the opposite direction. The magnetizing field is then reversed once more to complete the loop.[8-9][11]

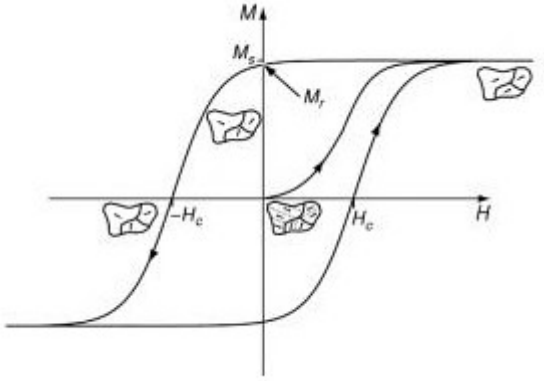

Figure 3: Typical hysteresis loop with saturation magnetization, M_S, Magnetic remanence, M_R and coercive field, H_C. [J. M. D. Coey Magnetism and magnetic Materials; Cambridge University Press (2010)]

Coercivity is a variable that strongly depends on the microstructure of the material as domain wall movement is required to completely cancel the magnetization and the movement itself is a process that is hindered by defects and crystal structure of the grains, requireing energy to overcome.

The remanent magnetization can be dependent on both the material properties and of the microstructure of the material. The magnetocrystalline anisotropy (*see section 3.1.5*) affects the rotation of the magnetic domains and a stronger anisotropy will allow for less rotation (or demand a stronger external field). The domain structure will be more strongly affected as a result, allowing for more of the saturation magnetization to remain, pinned in the domain structure.

The saturation magnetization provides little useful information on the material but is an important factor in many applications. It can, however, be compared to the remanent magnetization and if there is a large difference, the material is poorly optimized as a hard ferromagnet as it looses magnetization when the external field is removed.

All these measurements are dependent on the saturation of the magnetization. If this is not reached, something called minor loops are measured instead and are generally undesirable as they do not allow for any relevant measurements of the variables described in this section. (*see fig. 4*)

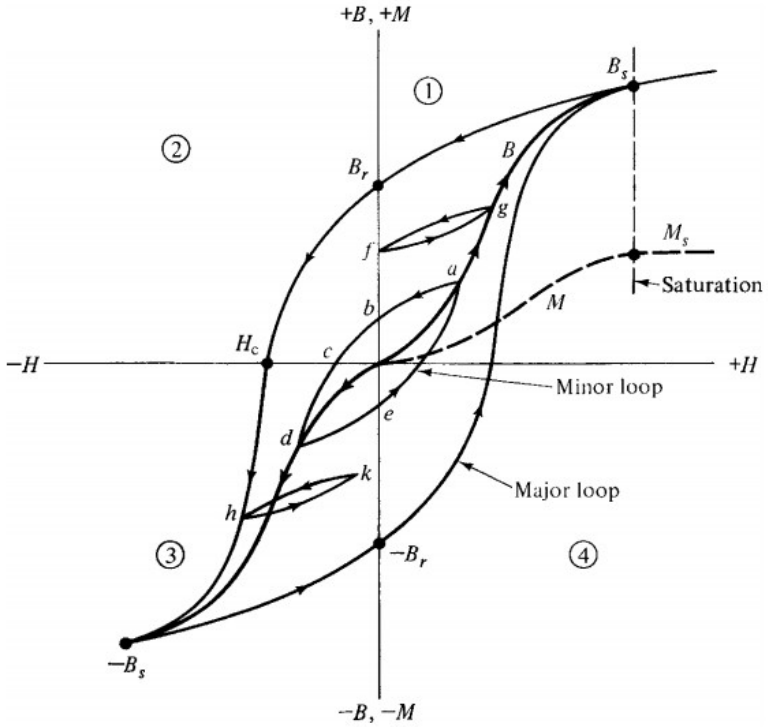

Figure 4: Hysteresis loop including major and minor loops. The minor loop (abcde) represents a loop produced when MS is not reached. [B.D. Cullity & C. D. Graham, Introduction to Magnetic Materials, Wiley (2009)]

3.1.3. Demagnetizing field

A *demagnetizing field* arises in a magnetic material due to emergence of the two magnetic poles and is, just like the stray field, directed from the north pole to the south pole but within the material itself. This counteracts the magnetization and must, for more careful calculations, be compensated for.

Thus, for an applied $\boldsymbol{H_{ext}}$, there is a demagnetizing field, $\boldsymbol{H_d}$, that must be compensated for as

$$\boldsymbol{H}_i = \boldsymbol{H}_{ext} + \boldsymbol{H}_d \quad \ldots (3)$$

where $\boldsymbol{H_i}$ is the measured value for the coercivity. Assuming an approximately ellipsoidal shaped sample, H_C can be approximated as

$$\boldsymbol{H}_i \simeq \boldsymbol{H}_{ext} - \mathrm{N}\,\boldsymbol{M} \quad \ldots (4)$$

where N is the demagnetizing tensor, here simplified to be a scalar. For irregular particles that can be approximated as spheres, N is well approximated as $N = 1/3$. In a sufficiently anisotropic material, however, this effect is small and will in this project be neglected as N also depends on the geometry of the magnet component which is unknown here.[8-9]

3.1.4. Energy product

It is sometimes useful to translate the hysteresis loop from a relation between $\boldsymbol{H}$ and $\boldsymbol{m}$, into a relation between $\boldsymbol{H}$ and $\boldsymbol{B}$ by inserting

$$M = \frac{m}{V} = \frac{m \cdot \rho}{m'} \quad \ldots (5)$$

into equation 1. Here (in eqn. 5) $\boldsymbol{m}$ is the *magnetic moment*, m' is the mass of the sample in question and ρ is the theoretical density of the powder. This yields

$$B = \mu_0 \left(H + \frac{m \cdot \rho}{m'} \right) \quad \ldots (6)$$

This makes it possible to produce the so called B-H curve and can be useful in determining, among other things, the *energy product*, $(BH)_{MAX}$.

The energy product for a magnet under ideal conditions, is calculated as

$$(BH)_{MAX} = \frac{\mu_0 {M_S}^2}{4} \quad \ldots (7)$$

but this limit is never reached in practice. (Derivation of this can be found in Appendix J) In reality there are losses that prevent real magnets from reaching this theoretical value such as the magnetic softness.[9]

To determine the energy product of a real material, measured values for the magnetization is translated from $\boldsymbol{M}$ to $\boldsymbol{B}$ (by use of eqn. 1) and multiplied by the $\boldsymbol{H}$ -field. The maximum value of this is the $(BH)_{max}$.

$$(BH)_{max} = max(-\boldsymbol{BH}) \quad \ldots (8)$$

3.1.5. Anisotropy

The *magnetocrystalline anisotropy* is mostly a result of the anisotropy of the unit cell. In all crystalline materials, the minimizing of all free energy in the material defines the domain structure. Of the several contributors to the free energy, two of them, the anisotropy energy and the exchange energy, are governing in the formation of the so called easy axis and the domains that align with this axis.[9]

Coey[9] describes it as

"*The balance of exchange and anisotropy usually leads to a structure in domains where magnetization lies along an easy axis, separated by narrow domain walls, where the magnetization rotates from one easy direction to another*"

3.1.6. Eddy currents

Eddy currents are small, curling currents that arise as a result of induction from a magnetic field in a conductive material and can, for example, be used as a non-destructive testing for microcracks. In a magnetic material, however, it has the negative effect of working against the magnetizing field (being a result of induction) and thus work against the magnetization of the material, although only transitionally in the magnetization process. It would also have a detrimental effect in an application of the resulting magnet, like linear generators as the magnet then is in a constantly changing field and thus the eddy currents will work much as a demagnetizing field would.[8]

3.1.7. The Curie temperature

The magnetic behavior of any material, specifically the susceptibility of the material, is dependent on the operating temperature. As the operating temperature rises, the susceptibility drops and thus also the magnetization until it eventually turns from ferromagnetic to paramagnetic and the magnetization is completely destroyed.

For the $(Fe_{0.7}Co_{0.3})_2B$, the curie temperature is found around 900K[18] making it perfectly suitable for generator design.

3.1.8. Hard and soft magnetic products

As described earlier, a hard magnetic material differs from a soft magnetic material in that it has a high coercivity. This allows the hard magnetic material to be used as magnetic cores in, for example linear generators without being demagnetized by the induced magnetic fields. Other common applications for hard magnetic materials include driving component in loudspeakers, refrigerator magnets, magnetic hard drive components etc.

The electric PM motors are one of the major applications and is steadily growing as modern, ever greener society, demands more and more electrical motors. Electric and E-hybrid cars, electric bicycles, scooters, advanced wind turbines and, potentially, wave power generators.

Soft magnetic materials also have a large and growing market, for the same reasons. Products like induction generators, transformers, inductors and so on, all rely on the soft magnetic materials and with the advent of so called smart grids, it is destined to be a growing market.[12]

3.2. Single crystal powder production

As previously described, this project focuses on production of a single crystal powder by heat treating a poly-crystalline material to obtain a crystal growth significant enough to at least get close to single crystal particles.

When the particles are heated, the crystals grow as a result of the *Ostwald Ripening Effect*. With sufficient time and sufficient temperature the grains should grow and eventually (ideally) form a microstructure close to single crystals.

3.2.1. Ostwald Ripening

Without delving too deeply into the thermodynamics, Ostwald Ripening can be most easily described as a diffusion of the material that make up the vapor pressure of the grains.

All matter has a vapor pressure; a certain concentration of material floating around its immediate surroundings. The concentration of this vapor depends on, among other things, the curvature of the surface of the material meaning; the smaller the object, the larger the vapor pressure.

The second law of thermodynamics states that[13]

"Specifically stated, in every volume element of any system and surroundings that may be experiencing change, at every instant of time, the entropy production is positive"

This implies that the disorder, or mixing, of a system will always increase when ever possible. This, in turn, implies that a higher concentration in one region is going to transport material to a region of lesser concentration until the concentration gradient is zero. This diffusion process is also highly dependent on the difference in concentration, meaning the effect will slow down as the concentrations level out and accelerate should the difference grow. In Ostwald ripening, the diffusion rate increases over time as the shrinking particles will have a steadily increasing vapor pressure and the growing particles subsequently a decreasing one, all due to the change in particle curvature.

This means that small grains will give up bulk material to sustain a vapor pressure that is continuously absorbed by larger grains that in turn will grow at the expense of the smaller grains as they absorb the material diffusing to them.

3.2.2. Single crystal materials

There are several applications in the world that require single crystal materials to function properly. Probably the most common single crystal material is the silicon wafers that make up the foundation in processors, transistors, microchips and so on. These applications rely on the electrically insulating ability of the silicon as well as non-varying conductive properties when doped with other species.[14]

In the more macroscopic world of single crystals, the best example is turbine blades that require each blade to be formed as a single crystal and of significant size. This requirement is a result of the high temperature creep that occur in normal, poly-crystalline materials an that a single crystal has a high level of resistance against. [16]

3.2.3. Macroscopic manufacturing

Although silicon wafers are used in small scale applications down to the microscopic level, the wafers are produced on a very macroscopic level through the Czochralski method. Silicon is melted along with dopants in the correct concentration in a large vat and a small seed crystal is lowered into the melt. The silicon begins to crystallize on the seed crystal when the temperature is just right and the seed crystal is slowly pulled out. The slower it is pulled out, the larger the radius of the crystal formed. Eventually a long ingot of perfectly crystalline silicon is formed from the melt that is allowed to cool before being sliced into the thin wafers that are later used to produce microchips etc.. [14]

Turbine blades are produced through a type of selective crystal growth were a small amount of the material is quenched in a directional manner, producing a few large grains. Material is then added to the grain that is of the correct crystal orientation that will yield the best creep resistance until the entire blade is formed. [16]

3.2.4. Microscopic manufacturing

On the microscopic level the sole means of producing single crystal particles is to heat treat the powder and allow the grains to grow by means of Ostwald Ripening. This process is based on diffusion and should, considering the increasing difference in concentration, be an accelerating process and thus the most rapid growth should occur at the end of a heat treatment. The effect is, however, tempered by the complexity of real particles as they normally have a certain amount of porosity, inclusions, defects etc..

4. Powder compositions

Earlier work[3-6] has shown that an alloy of iron, cobalt and boron, in the relation $(Fe_{0.7},Co_{0.3})_2B$ could yield very desirable magnetic properties. For this project, eight different melts have been produced with slight variations in chemistry and using different types of atomization *(see Materials & Methods section)*, to find what process of atomizing would be most beneficial to the microstructure of the resulting powder. Below follows a table of the different melts, their compositions and the atomizing method used. The "*Trial*" column represents the atomization type with *"WA"* being water atomization and *"GA/W"* being gas atomization with water quenching.

The first of the melts, G336, was found to have an excess of boron that could potentially result in an excess of (Fe,Co)B. The rest of the melts were an attempt at getting a higher concentration of $(Fe,Co)_2B$ by having a more accurate composition. The G400 and G408 melts, however, were composed to fit the eutectic composition (*see fig. 7*) as this shows a more pure $(Fe,Co)_2B$ at room temperature.

In addition, the silicon contents, manganese contents and oxygen levels, vary between the later melts. The main purpose of the silicon was to produce a surface coating of the particles that could act as an electrical insulation between grains in the finished product. Oxygen on the other hand, is a byproduct of the atomization process.

Table 1: All alloys and their compositions except Fe which is the remainder to 100%

Trial	Name	wt%B	wt%Co	wt%Si	wt%Mn	wt%C	wt%O	Bubbles	$(Fe,Co)_yB$
WA	G336	9.20	29.70	0.98	0.13	0.15	0.45	Yes	1.91
WA	G399	8.41	28.40	1.01	0.12	0.16	0.43	Yes	2.03
WA	G400	4.19	29.50	1.00	0.05	0.11	0.37	Yes	4.28
WA	G401	8.45	28.40	0.25	0.12	0.16	0.34	Yes	2.04
GA/W	G398	8.37	28.30	1.03	0.12	0.17	0.20	No	2.05
GA/W	G406	8.70	28.10	0.23	0.12	0.18	0.21	No	1.98
GA/W	G407	8.27	28.02	1.02	0.12	0.16	0.28	No	2.07
GA/W	G408	3.85	28.66	0.99	0.05	0.10	0.22	No	4.69

4.1. Phases and microstructures

As the material is an intermetallic compound of three components, a ternary phase diagram is required to get a fully comprehensible image of the possible phases and their transitions. A complete ternary phase diagram of this compound, however, has not been found in the literature but in recent publications by O. Fabrichnaya[18] and Y. Q. Liu[6], an attempt is made to summarize a number of studies and create a unified image of the phase relations. Similar work has also been done by J. Nowacki[19,20] that appears to be in agreement with them.

To complement these, a quasi binary phase diagram has been produced using Thermo-Calc using a fixed amount of Co of 28.4 wt%. (*see fig. 7*)

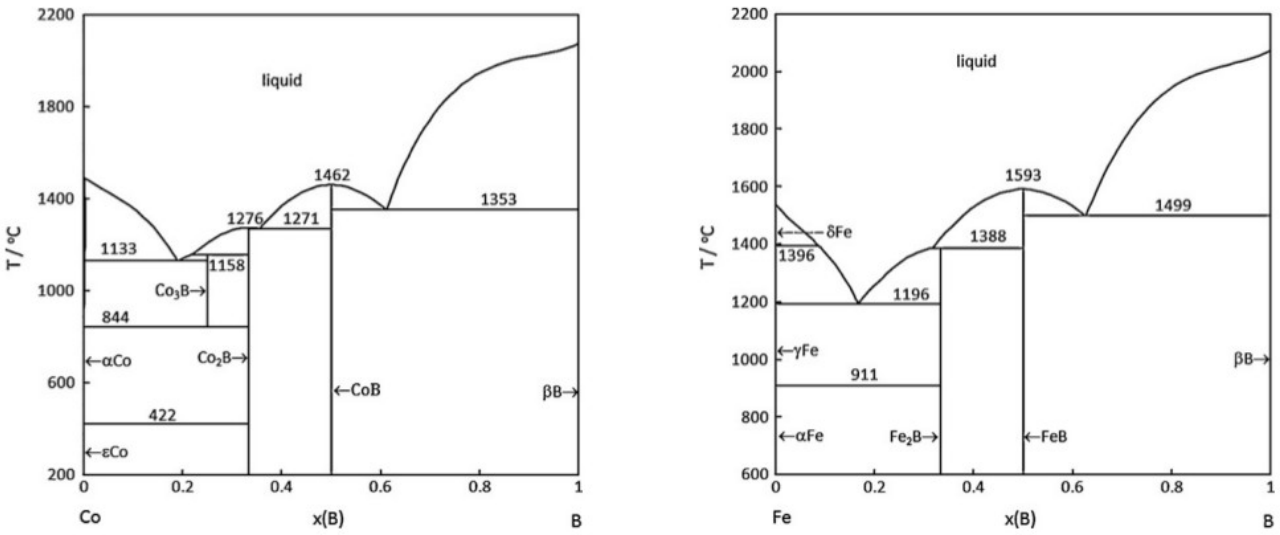

Figure 5: Binary phase diagrams of Co vs. B (left) and Fe vs. B (right), in at%. [Y. Q. Liu et. al., Journal of Alloys and Compounds; 509 (2011), p. 4806.]

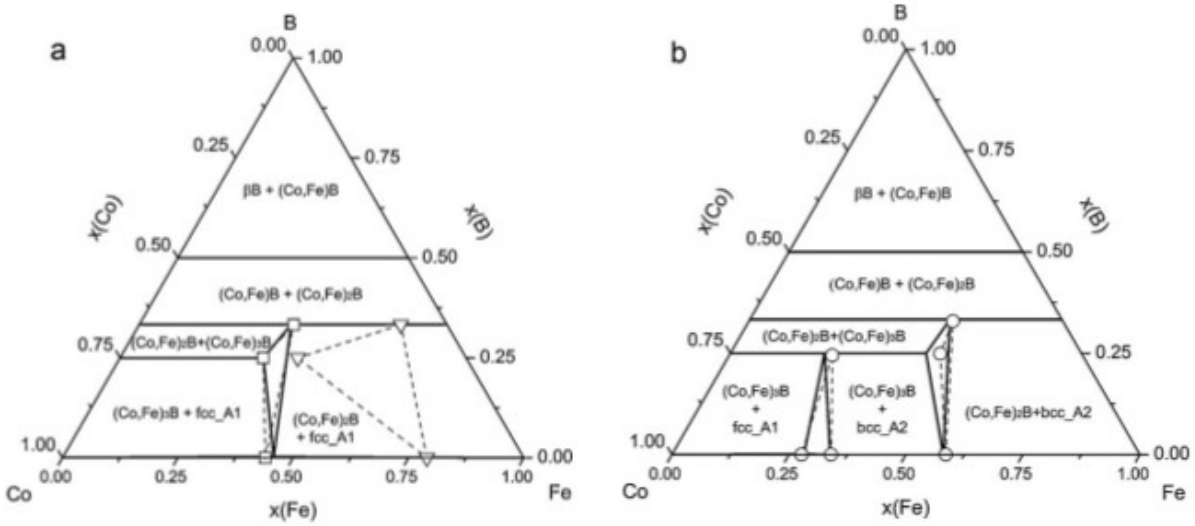

Figure 6: Isothermal sections of ternary phase diagrams at (a) 1000^{O}C and (b) 900^{O}C. Dashed lines indicate measurements form other publications for comparison. [Y. Q. Liu et. al., Journal of Alloys and Compounds; 509 (2011), p. 4809.]

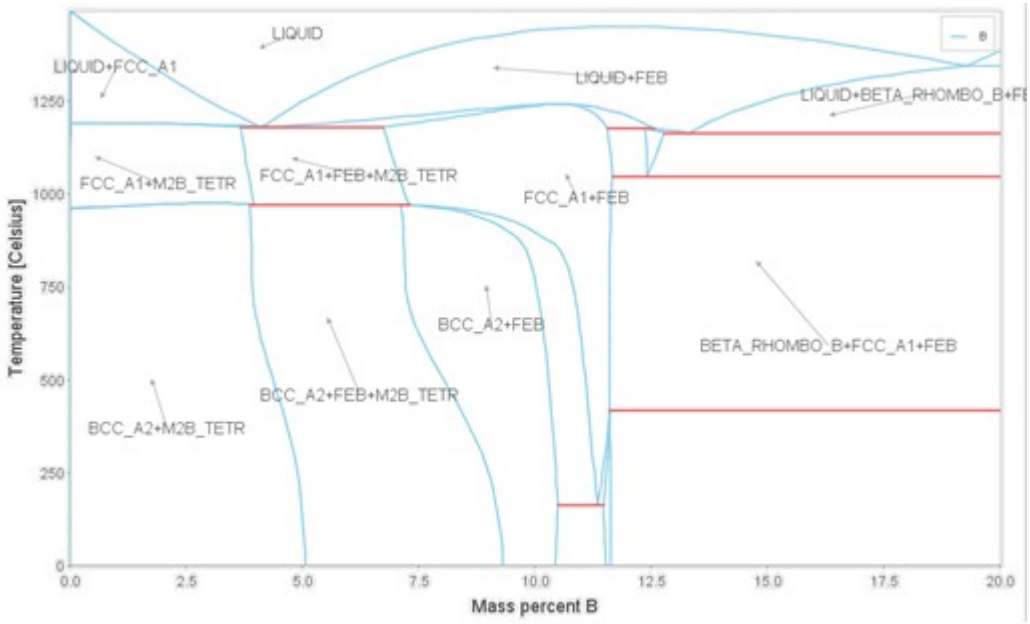

Figure 7: Binary phase diagram of Fe – B, theoretically calculated in Thermo-Calc with a fixed amount of Co at 28.4 wt%.

5. Materials and methods

The following sections explain what equipment and analysis methods have been used and under what conditions.

5.1. Atomization

Atomization is a process in which a molten metal is broken up into small particles whose size, shape and general microstructure depends on the type of process and the conditions in the atomizer such as temperatures, pressures and nozzle geometries.

5.1.1. Water atomization

In water atomization, high pressure water jets are shot at a molten stream of metal to break up the melt and cool the droplets so that they form solid particles. The pressure, number of- and direction of jets, and temperature are the most important parameters that can be varied in order to achieve various sizes and shapes of particles. A protective gas can also be applied to guard against unwanted oxidations. This method is generally used when a high cooling rate is desired and tends to create irregularly shaped, dense particles.

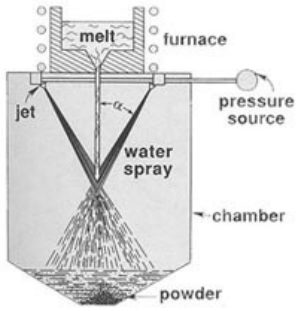

Figure 8: Conceptual image of the water atomization technology. [R.M. German, Powder Metallurgy Science; 2nd Ed., MPIF (1994)]

5.1.2. Gas atomization

Much like water atomization, the gas atomization shoots compressed gas at a stream of molten metal to break up the melt into droplets and then solid particles. The advantage to this method is that the lowered quench rate allows for more spherical particles to form. It is, thus, normally used when a lower rate of cooling is desired and has not been employed as such in this project. Gas atomization also has the added advantage of producing less oxide which is important for high alloy melts. It has, however, not been a problem in the materials used in this work.

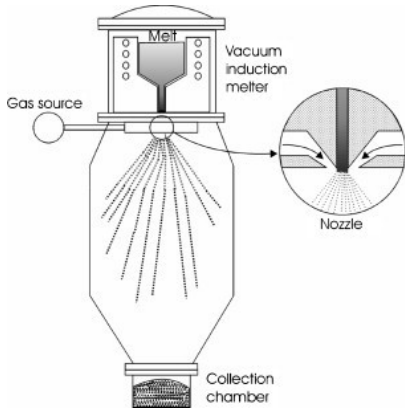

Figure 9: Conceptual image of the water atomization technology.
[W. R. Osório et. al., Electrochimica Acta, 69 (2012), p.372]

5.2.3. Gas & water atomization

Water and gas can also be combined so that the roundness of the gas atomized particles is preserved as well as the high cooling rate of the water atomization. This process is called Gas Atomized – Water Quenched (GA/W) and is done by allowing gas atomized particles/droplets fall into water in order to quench them rapidly. This combines the elevated quench rate of the water atomizing with the initially low cooling rate of the gas atomization allowing for spherical particles that are still quenched at a relatively high rate.

5.2. Sieving and particle size distributions

Sieving was done several times to differentiate the size distribution so that a potential size dependence could be revealed as well as to give a greater homogeneity in the milled powders. Using an analytical sieve shaker stack with the mesh sizes 36µm, 63µm, 75µm and 106µm, these sieving sessions resulted in distributions as found in Appendix B. Larger particles should, theoretically, be the result of a lower cooling rate and lower nozzle pressure compared to the smaller particles.

5.3. Ball milling

Milling has been done using a ball milling machine (Retch PM 200) that mills by rotating balls of stabilized zirconia in a cup of the same material. The optimal rotational speed and duration was previously optimized by S. Kontos for the powder type in question[23] and subsequently set to 3h @ 400rpm with a directional change every 5 minutes. Each milling sample was also suspended in 1g of n-Hexane (so called “wet milling”) to get a more homogeneous milling. Different levels of milling was obtained by using three 20mm balls for a coarser milling (denoted 5/20 -milling) and a large number of 5mm balls for finer milling (denoted 5/5 -milling). The exact number of 5mm balls is not known but was kept at ~1/3 filled and constant by weight to avoid variations in the result. An even finer milling was obtained by milling in two steps; first 5/20 and then 5/5. (The notation 5/5 and 5/20 is due to the amount of powder each time being 5g.)

5.4. Heat treatments

The heat treatments in this lab scale research has been done in a furnace designed by engineers at Höganäs and the specific design is a trade secret. It can, however, be revealed that it relies on an overpressure of the atmospheric gas to sustain the desired environment in the furnace. For the experiments in this work, the gases used has been N_2 and H_2 or mixtures thereof.

5.5. Etching

An attempt was made to etch away a potential oxide coating from milled G336 powder (5/20+5/5) by allowing small amounts of the powder to react in a premixed concentrations of hydrochloric acid (HCl). To abort the reaction and dry the powder, the mix was poured over a filter paper, rinsed in water and acetone (99.999%), and then placed in an oven at 70^{O}C for 10 minutes.

The specific series of concentrations and reaction times was set up using a trial planning software (MODDE 9.1 from Umetrics) in which the results of the subsequent chemical analysis were analyzed to find a potential correlation between the time, concentration and oxygen contents. It does this by doing a mathematical fitting to find a statistical correlation.

The factors investigated were

- Reaction time in the acid. Outer limits set to range from 1-10 minutes.
- Acid concentration. Outer limits set to to range from 0.5-1 mol/l
- Rinse time in water. Outer limits set to to range from 0-120 seconds.
- Rinse time in acetone. Outer limits set to to range from 30-120 seconds.

The response was taken to be the relative amount of oxygen found in the powder after treatment by combustion IR detection analysis (LECO).

An additional analysis was made in the STA so as to see if a difference could be seen compared to the STA done on the non-etched powder previously.

5.6. Analysis methods

5.6.1. Light Optical Microscopy (LOM)

The LOM analysis was a qualitative analysis aimed at characterizing the general structure of the G336 powder and relating it to the particle size distribution. This was done at three levels of heat treatment to also obtain a qualitative understanding of the grain growth rate.

Table 2: Description of all twelve samples made.

Untreated		700^{O}C, 8h		700^{O}C, 16h (8h+8h)	
Pellet 1	<36µm	**Pellet 5**	<36µm	**Pellet 9**	<36µm
Pellet 2	36-63µm	**Pellet 6**	36-63µm	**Pellet 10**	36-63µm
Pellet 3	63-75µm	**Pellet 7**	63-75µm	**Pellet 11**	63-75µm
Pellet 4	75-150µm	**Pellet 8**	75-150µm	**Pellet 12**	75-106µm

In order to get a cross section of the particles that could be viewed in the LOM and bind them to a surface, a small amount of powder from each size distribution and heat treatment was baked into a plastic pellets (*see tab. 2*) using Backlite. (Full recipe for casting, polishing and etching can be found in Appendix C.1.)

The microscope used is a Leica DMRE using bright field with an auxiliary camera connected to a computer. Using the *Leica Qwin Pro* software, images were captured and analyzed using a macro that can distinguish between different levels of light and highlight the areas that are brighter or darker than a set level. The macro then drew horizontal lines over the image that were then manually erased in the grain boundaries. What then remained was a number of lines representing the diameter of the grains intersected by the lines.

With these lines, the macro could then calculate the average length of the line segments (grain diameters) for each particle. While these lines did not find and include every grain in a particle and, consequently, could not be

used to get reliable absolute values, it could be used to get a quantification reliable enough for a qualitative comparison. (*see fig. 36*)

The particle structures were tentatively quantified by choosing areas of similar particle densities for each size distribution and temperature, and manually counting the particles of each type. An overlaying grid was added to facilitate counting although some images have not retained the grid when saved.

By using the grain counting macro on similarly sized particles a simplified average of the number of grains per particle could be obtained for each particle size distribution and temperature.

5.6.2. Simultaneous Thermal Analysis (STA)

STA is a combination of Thermogravimetric Analysis (TGA) and Differential Scanning Calorimetry (DSC). It has the advantage of being able to compare the two analysis easily but with a slightly lowered accuracy.

TGA is based on measuring the sample weight along with its container and compare the weight to an identical, empty container while heating the two in a gas. If the gas contains oxygen the TGA can, for example, detect at what temperature oxidization takes place by the increased sample wight from the added oxygen. For the purposes of this work, however, the experiments were performed in an atmosphere of pure Ar.

DSC is based on the measuring of the temperature of the two containers. One holding the sample being measured, and one empty reference container. The containers are then heated individually and the input energy is carefully measured. The difference of the required energy input to keep the two containers at equal temperature forms the basis for the DSC.

The STA used in this work is a Netzsch STA-449 (“Jupiter”) and the atmosphere is pure Ar obtained after purging the air three times by alternating pure Ar and vacuum >99%.

STA analysis was performed on the G336 powder in an attempt to understand what happens in the material when it is heat treated. An STA should reveal any phase transitions as well as any chemical reaction that might occur. To get a comparison for the result with a known phase transition, pure iron was also analyzed.

5.6.3. Dilatometry

The dilatometer (Netzsch DIL-402C) measures the length of a cylindrical solid sample with great accuracy while the sample is heated in a vacuum. This allows the dilatometer to detect if there is any dimensional changes during the heating, such as crystallographic transformations or unexpected thermal expansion without the influence of oxidations or other chemical reactions. A reference sample is used to define the expected thermal expansion.

For these measurements, cylindrical pellets were compacted from the powder of interest with diameter and length as close as possible to the reference samples so as to avoid discrepancies in the thermal expansion measurements. Measurements were performed in pure Ar after purging the air with pure Ar twice by alternating pure Ar and vacuum >99%.

Dilatometry analysis was performed on a few of the G336 samples in an attempt to confirm that the peak seen in the STA is indeed a phase transition. The powders were pressed in a hydraulic press to a pressure of 600 MPa in a mold and a cylindrical pellet with a length of 7.078 mm was produced.

5.6.4. Chemical analysis

The chemical analysis was made by professionals at Höganäs AB by use of combustion IR detection using a LECO setup to determine the chemical composition of the various melts.

5.6.5. Scanning Electron Microscopy (SEM)

The SEM uses a stream of electrons, focused by electromagnetic constrictor coils, to bombard a very small part of the sample. In order to get good imaging of the different phases, the detection method has, for this work, been using the back scattered electron (BSE) detector. The SEM analysis in this project has been carried out at Höganäs AB by trained professionals using a Hitachi 6600 SEM.

The SEM imaging had several purposes. One was used to get enough resolution to determine the particle size and microstructure of milled powders that were beyond the resolving limit of the LOM. As some powders were very fine there were initially some issues with low conductivity in the plastic pellet the powder was pressed in. This issue was eventually overcome by mixing a small amount of Carbon Black in the powder mixture and some iron powder in the distance part of the pellet. A very fine surface preparation, including oxide polishing, was also required to get good imaging. (Full recipe can be found in Appendix E.1.)

The SEM was complemented with Energy-Dispersive x-ray Spectroscopy (EDS) that uses the characteristic x-ray responses of different elements to determine what elements are present and their dispersion in the material. This allowed for second use of the SEM; a tentative identification of the inclusions and other concentration variations found in the particles. Another use for the SEM imaging was to estimate the particle size of milled powders as the resolution limit of LOM is too low. This is not a qualitative method and is thus only usable as an estimation.

SEM was performed mostly on G336 as this is the primary powder investigated in this work. An analysis of the G398 was also started but due to time constraints, this was not completely finished.

5.6.6. X-ray diffraction (XRD)

Since most of the powders were milled to a level far beyond what can be seen in light microscopy and often close to the resolving limitations of the SEM, the only real way to characterize the crystal growth is by means of X-ray powder diffraction. It also provides a way of quantifying the crystal growth with minimal human error.

There are two main types of XRD; the transmission type and the reflection type. In this work the reflection type XRD has been used (Panalytical Xpert Pro). This is a method of analysis based on the constructive and destructive interference from reflections (scattering) of x-rays in the crystal planes. The pattern produced by this is determined by the lattice parameters of the crystal and is thus characteristic for each unique material.

In this pattern there will also be a certain level of broadening of the peaks (Scherrer broadening) that can be used to analyze the crystal size of a polycrystalline material as well as determining how much strain the lattice is under due to inherent imperfections or imperfections caused by ball milling.

To analyze the broadening and obtain a value for the crystal size and strain, the Highscore Plus software has been used and to determine the relative amounts of $(Fe,Co)_2B$ and (Fe,Co)B, the Fullprof software. Input parameters to the latter was taken from Pearson's Crystal Database from Crystal Impact.

The first XRD analyses were done to find accurate values for the crystallite size and determine the internal strain of the G336 material as well as provide some insight into the process of relaxation and crystal growth.

A second XRD series of the G336 material was also measured after 3h heat treatment in a 100% hydrogen atmosphere, after milling (5/20 + 5/5) and again after relaxation in an inert atmosphere of nitrogen gas for 1h at $700^{O}C$. The purpose of this was to find if the hydrogen heat treatment would embrittle the material and thereby allow for better milling and possibly a more rapid crystal growth as a consequence. Different temperatures of the hydrogen heat treatment was used and on two different particle size fractions.

The last XRD measurements were of a new series of melts (G398 – G408) to determine what phases were present and in what amounts.

5.6.7. Vibration Sample Magnetometer (VSM)

In order to analyze the resulting magnetic properties of the material, a VSM (Lake Shore; Modell 7407) was used. The VSM allows for a measurement of the magnetic moment in a small sample by applying a strong external field *(see chapter 3.1.2. Magnetic Measurements)* and plotting a hysteresis curve. The maximum external field *H* was set to 2T and the resolution to 3600 measuring points evenly distributed. The powders tested were as specified in the table found in the results section. *(see tab. 8)*

6. Results

In the following sections, the results of the various tests are presented and analyzed briefly.

6.1. LOM

The first image (*see fig. 10*) is a representative for the samples indicating the general structure of the powder including very round particles with a large number of them containing bubbles. More images can be found in Appendix C.2.

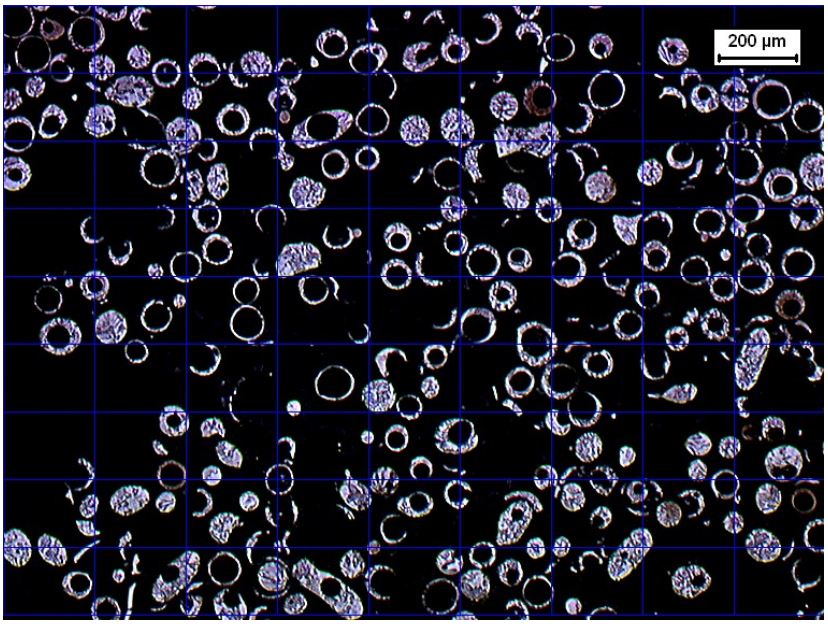

Figure 10: Light optical image of the particles in G336, 75-106µm, with overlay grid.

In the graphs below (*see fig. 11-14)*, particle type distribution is presented as a function of heat treatment done at $700^{O}C$ in a N_2 atmosphere. What can be seen is that the relative amount of undesired particles, such as those containing bubbles and those with sub-micron microstructure, is relatively high. The heat treatment, however, seems to have yielded no definite trends except one. The sub-micron particles appear to increase in number as the samples are heat treated. Tables of the data collected can be found in Appendix C.3.

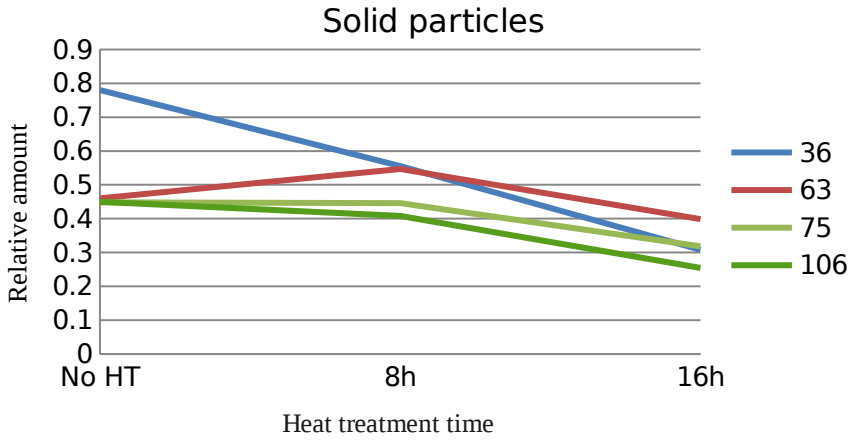

Figure 11: Change of relative amounts of solid particles in G336.

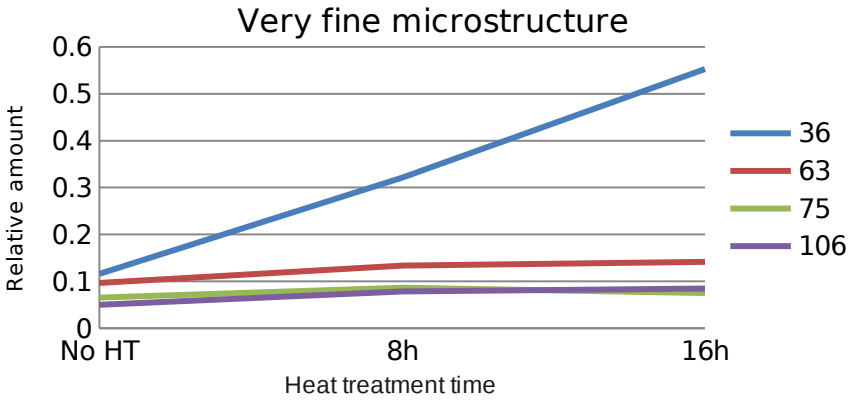

Figure 12: Change of relative amounts of very fine particles in G336.

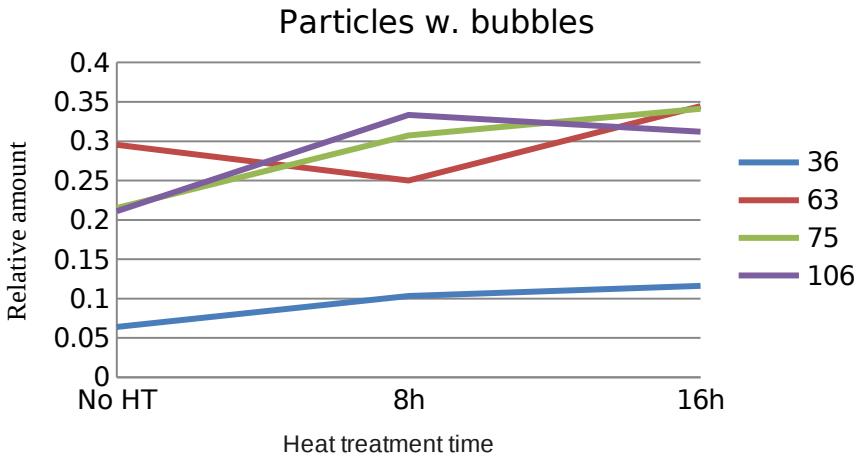

Figure 13: Change of relative amounts of bubbled particles in G336.

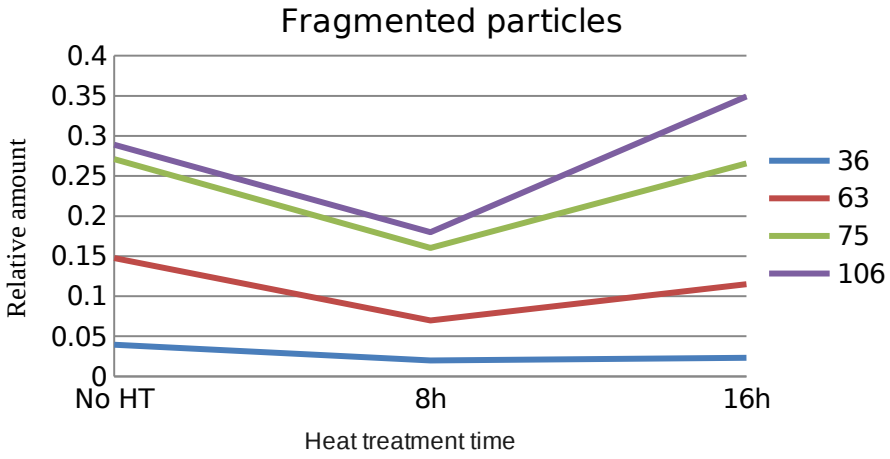

Figure 14: Change of relative amounts of fragmented particles in G336.

Data from the grain counting and grain size calculation can be seen below (*see fig. 15*) and is based on an average of 15 particles per sample. From this a number of particles per grain was estimated and can be seen to not yield any conclusive evidence of growth. (*see fig. 16*) data collected can be found in Appendix C.3.

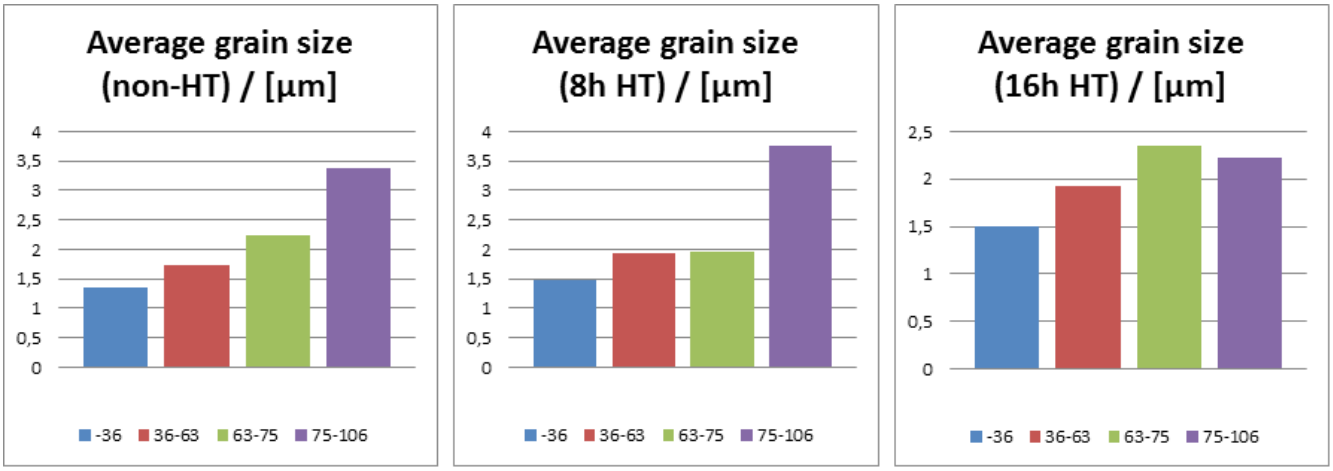

Figure 15: Average grain size as a result of the grain counting macro.

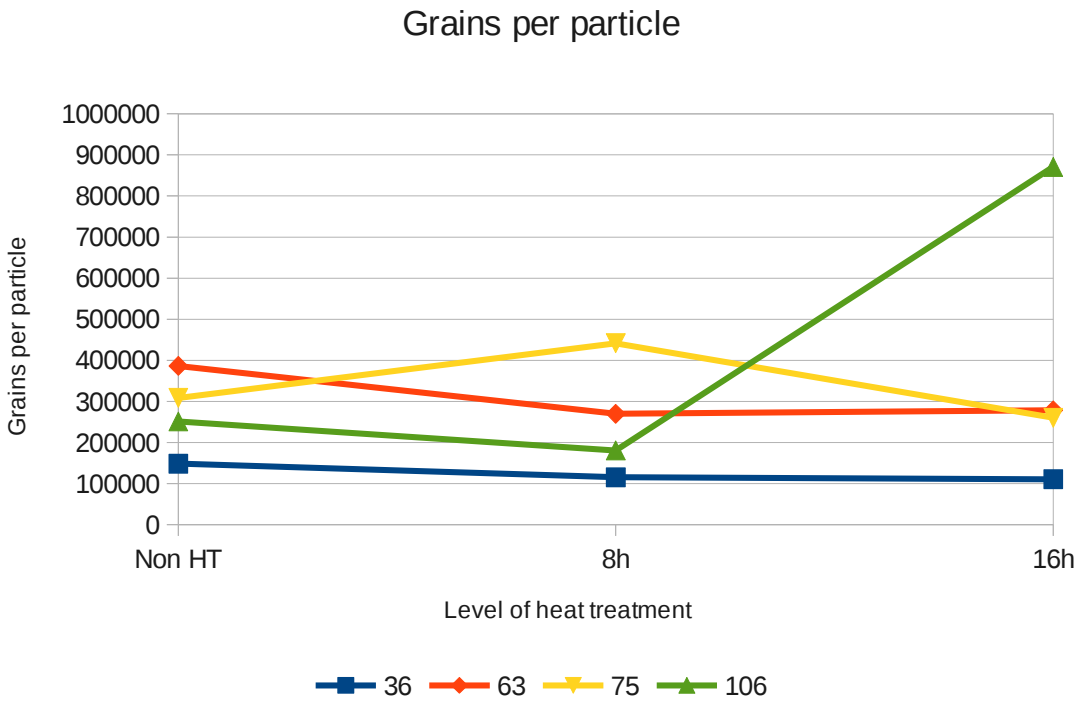

Figure 16: Estimated number of grains per particle.

6.2. STA

In an attempt at finding out precisely what takes place in the G336 material when it is heat treated, several samples with different milling and particle size distributions were analyzed in an STA. The figures below (*see fig. 17-18*) shows an overlay of the four powder fractions for non-milled powder and an overlay of the four powder fractions for milled powder (5/20 + 5/5 – milling). Only the DSC graphs have been plotted here as the TGA graphs show no real change in mass for any of the samples. The individual DSC graphs can be found in Appendix D with their respective TGA graphs.

What can be seen in these graphs is a small exothermic peak for the <36µm fraction for both the milled and non-milled powders, that does not clearly show up in the other particle size fractions for the overlay graphs. In the individual graphs, however, the peak shows up in most samples albeit very slightly in some cases. What can also be seen is a continuous slope that is different for the non-milled samples but seems to be very similar in the four milled samples.

The comparative DSC of the pure iron powder shows a similar behavior at the temperature for the expected phase transition in terms of the peak size and shape. The pure iron phase transition from α-Fe (ferrite) to γ-Fe (austenite) is expected at just over 900^{O}C. The exothermic peak for the pure iron can be found around 920^{O}C supporting the assumption that this peak is the phase transition. A small peak is also found around 770^{O}C. This coincides quite well with the curie temperature of pure iron at 768^{O}C.

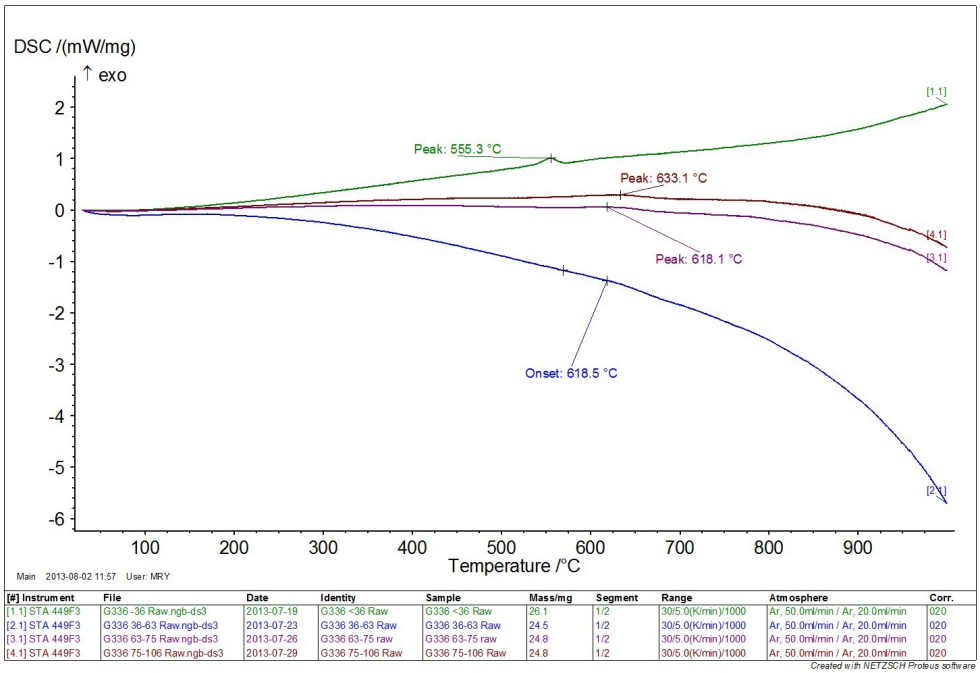

[#] Instrument	File	Date	Identity	Sample	Mass/mg	Segment	Range	Atmosphere	Corr.
[1.1] STA 449F3	G336 -36 Raw.ngb-ds3	2013-07-19	G336 <36 Raw	G336 <36 Raw	26.1	1/2	30/5.0(K/min)/1000	Ar, 50.0ml/min / Ar, 20.0ml/min	020
[2.1] STA 449F3	G336 36-63 Raw.ngb-ds3	2013-07-23	G336 36-63 Raw	G336 36-63 Raw	24.5	1/2	30/5.0(K/min)/1000	Ar, 50.0ml/min / Ar, 20.0ml/min	020
[3.1] STA 449F3	G336 63-75 Raw.ngb-ds3	2013-07-26	G336 63-75 raw	G336 63-75 raw	24.8	1/2	30/5.0(K/min)/1000	Ar, 50.0ml/min / Ar, 20.0ml/min	020
[4.1] STA 449F3	G336 75-106 Raw.ngb-ds3	2013-07-29	G336 75-106 Raw	G336 75-106 Raw	24.8	1/2	30/5.0(K/min)/1000	Ar, 50.0ml/min / Ar, 20.0ml/min	020

Created with NETZSCH Proteus software

Figure 17: DSC overlay of the four powder fractions of non-milled powders. <36 (green), 36-63 (blue), 63-75 (purple) and 75-106 (red).

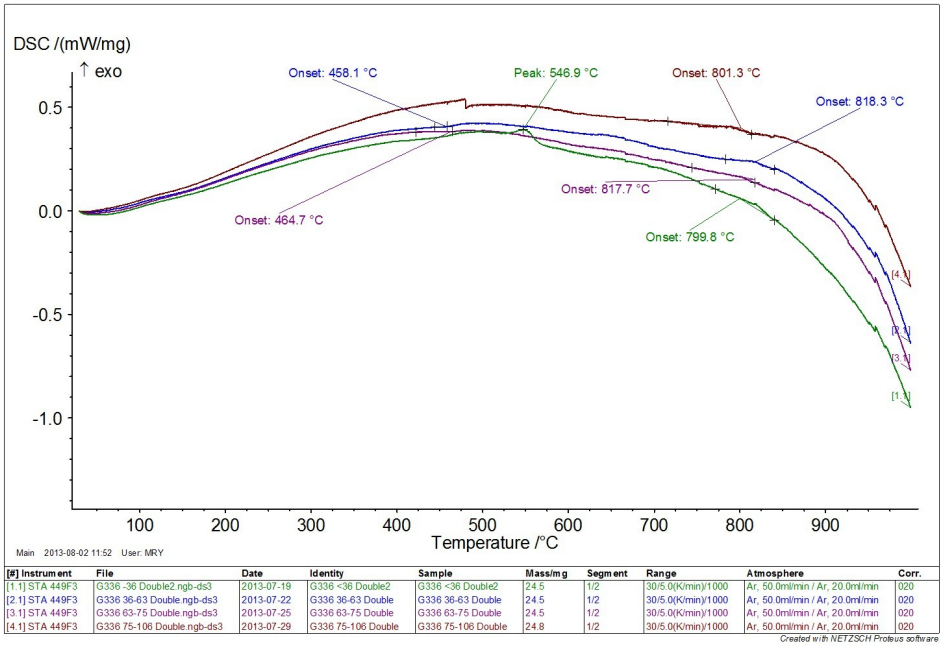

[#] Instrument	File	Date	Identity	Sample	Mass/mg	Segment	Range	Atmosphere	Corr.
[1.1] STA 449F3	G336 -36 Double2.ngb-ds3	2013-07-19	G336 <36 Double2	G336 <36 Double2	24.5	1/2	30/5.0(K/min)/1000	Ar, 50.0ml/min / Ar, 20.0ml/min	020
[2.1] STA 449F3	G336 36-63 Double.ngb-ds3	2013-07-22	G336 36-63 Double	G336 36-63 Double	24.5	1/2	30/5.0(K/min)/1000	Ar, 50.0ml/min / Ar, 20.0ml/min	020
[3.1] STA 449F3	G336 63-75 Double.ngb-ds3	2013-07-25	G336 63-75 Double	G336 63-75 Double	24.5	1/2	30/5.0(K/min)/1000	Ar, 50.0ml/min / Ar, 20.0ml/min	020
[4.1] STA 449F3	G336 75-106 Double.ngb-ds3	2013-07-29	G336 75-106 Double	G336 75-106 Double	24.8	1/2	30/5.0(K/min)/1000	Ar, 50.0ml/min / Ar, 20.0ml/min	020

Created with NETZSCH Proteus software

Figure 18: DSC overlay of the four powder fractions of milled powders. <36 (green), 36-63 (blue), 63-75 (purple) and 75-106 (red).

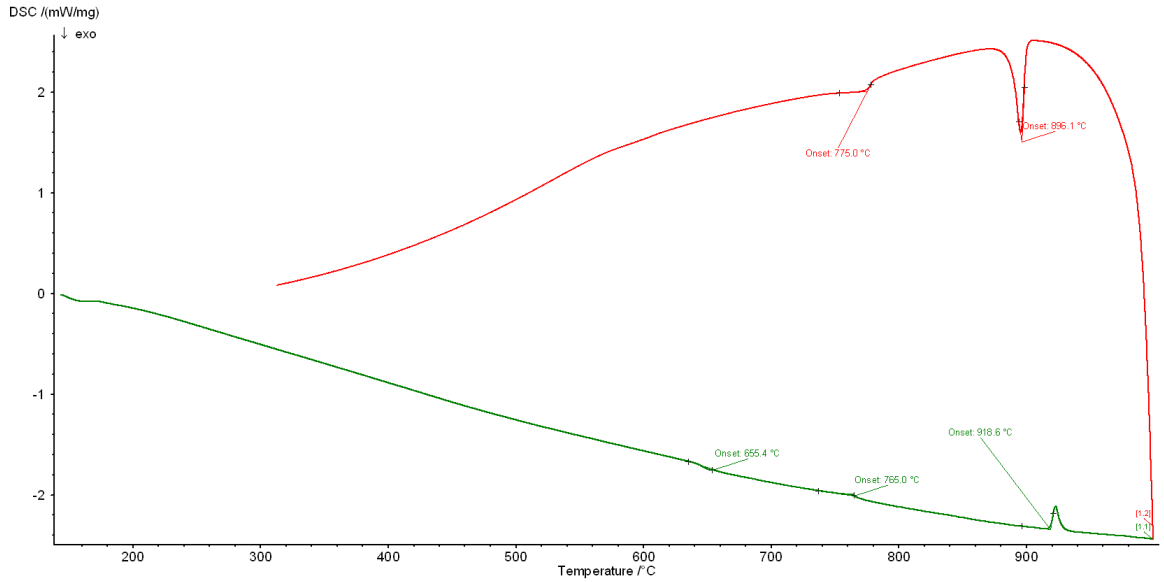

Figure 19: DSC of the pure iron powder with both heating (green) and cooling (red) included.

6.3. Dilatometry

The result of the dilatometry can be seen in the figure below along with two of the DSC graphs to get a correlative image of the DSC to dilatometry. The dilatometry graph show that there is indeed a dimensional change around the temperature of the onset temperature for the peaks in the DSC. Prior to this there is an expansion that can be attributed to normal thermal expansion. A correction file was used but this does not guarantee complete removal of all thermal expansion influences. After the more abrupt reduction in length, there is a continuous shortening of the sample that could be attributed to a sintering behavior as the expected onset of sintering is in this region. The breaking point around 800^{O}C could possibly represent an accelerated sintering making the first slope an initial stage of sintering, binding the particles together.

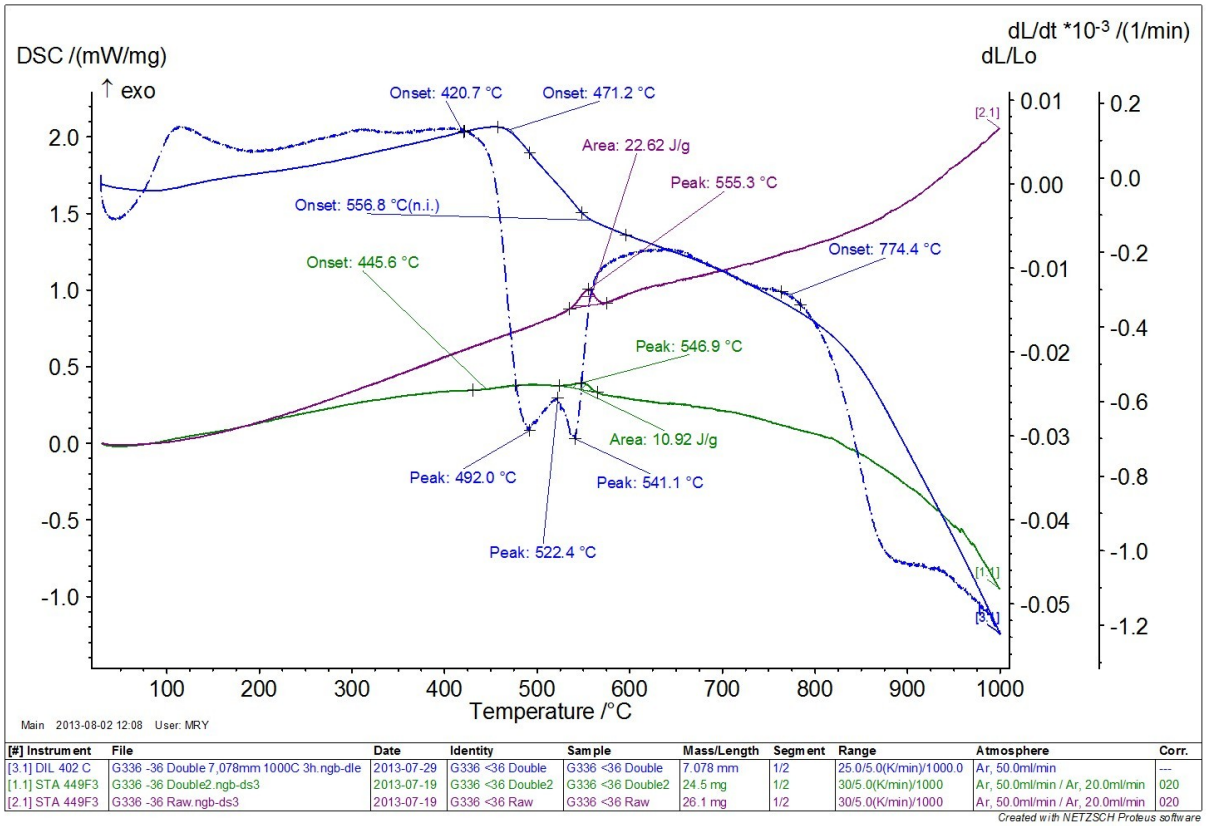

[#] Instrument	File	Date	Identity	Sample	Mass/Length	Segment	Range	Atmosphere	Corr.
[3.1] DIL 402 C	G336 -36 Double 7,078mm 1000C 3h.ngb-dle	2013-07-29	G336 <36 Double	G336 <36 Double	7.078 mm	1/2	25.0/5.0(K/min)/1000.0	Ar, 50.0ml/min	---
[1.1] STA 449F3	G336 -36 Double2.ngb-ds3	2013-07-19	G336 <36 Double2	G336 <36 Double2	24.5 mg	1/2	30/5.0(K/min)/1000	Ar, 50.0ml/min / Ar, 20.0ml/min	020
[2.1] STA 449F3	G336 -36 Raw.ngb-ds3	2013-07-19	G336 <36 Raw	G336 <36 Raw	26.1 mg	1/2	30/5.0(K/min)/1000	Ar, 50.0ml/min / Ar, 20.0ml/min	020

Created with NETZSCH Proteus software

Figure 20: Dilatometry results (solid blue) as compared to 5/20+5/5 -milled (green) and non-milled (purple) powder DSC. There is also a first derivative of the dilatometry plotted so as to give a more distinct expression of the dimensional change onset (blue dashed).

6.4. Chemical analysis

In the eight melts produced, variations were made in boron contents so as to get closer to the desired $(Fe,Co)_2B$ phase. Two of them, G400 and G408, were made with a boron deficiency (~4 wt%) in an attempt to compare the eutectic composition to the stoichiometrically (to $(Fe_{0.7},Co_{0.3})_2B$) calculated one. The eutectic composition is predicted by the phase diagram (*see fig. 7, p. 12*) to have a better purity of $(Fe,Co)_2B$.

Variations were also made in silicon contents and atomization technique. Silicon as it might be able to coat the particles and form an electrically insulation layer already form the atomizing and is thus an important factor. The atomization techniques could yield different microstructures and different phases depending on technique such as bubbles in the particles, oxygen levels general microstructure.

The results of the chemical analysis show the following (*see tab. 1, p. 10*):

- An excess of boron in G336
- A slight lowering of the oxide levels from the gas/water atomization compared to water atomization. Close to target composition for the eutectic compositions with a slight difference from the atomization technique in oxygen level.
- The two compositions without added silicon still have ~0.25 wt% Si.

6.5. Etching

In the table below, each etching experiment is detailed along with the oxygen analysis result. The Modde analysis of this showed no dependency of oxygen levels.

Table 3: The Modde experiment design and the measurement results.

Exp. no.	Reaction / [min]	Acid conc. / [mol / l]	Rinse – water / [sec]	Rince – Acetone / [sec]	Oxygen / [%]
4	10	1	0	30	0.292
5	1	0.5	120	120	0.432
1	1	0.5	0	30	0.423
3	1	1	0	120	0.974
9	5.5	0.75	60	75	0.108
8	10	1	120	120	0.115
6	10	0.5	120	30	0.119
2	10	0.5	0	120	0.108
7	1	1	120	30	0.167

The STA analysis of the G336 material (*see fig. 21*) revealed no new peaks compared to the earlier STA analysis but showed the peak for the suspected phase transition more clearly than the non-etched counterpart in the earlier STA analysis. (*compare fig. 18, p. 23*) The peak also appears at a lower temperature.

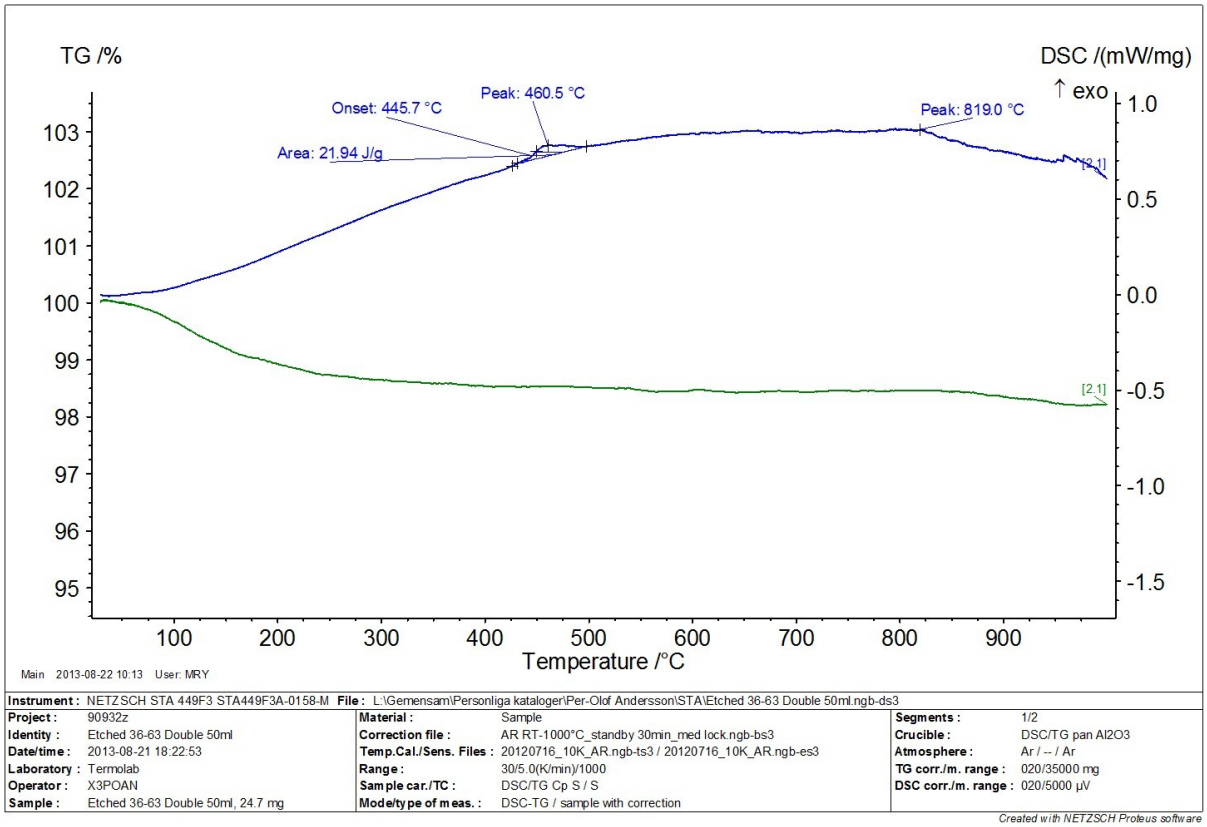

Figure 21: STA of etched G336 of the 36-63µm fraction. Green graph shows the TGA and blue graph show the DSC.

6.6. SEM

6.6.1. G336

The SEM was used as a means of determining the particle shape, particle size, crystallite size and, in some cases, to make an EDS mapping in order to determine the distribution of the constituent elements.

This was done for G336 to find the location of the oxygen that was earlier assumed to be a surface oxidation. In the figure series below, the results of the EDS mapping of the G336 powder is presented. (*see fig. 22*) What can be seen in these is an enrichment of Co and Si in the grain boundaries as well as an enrichment of B in the darker inclusions.

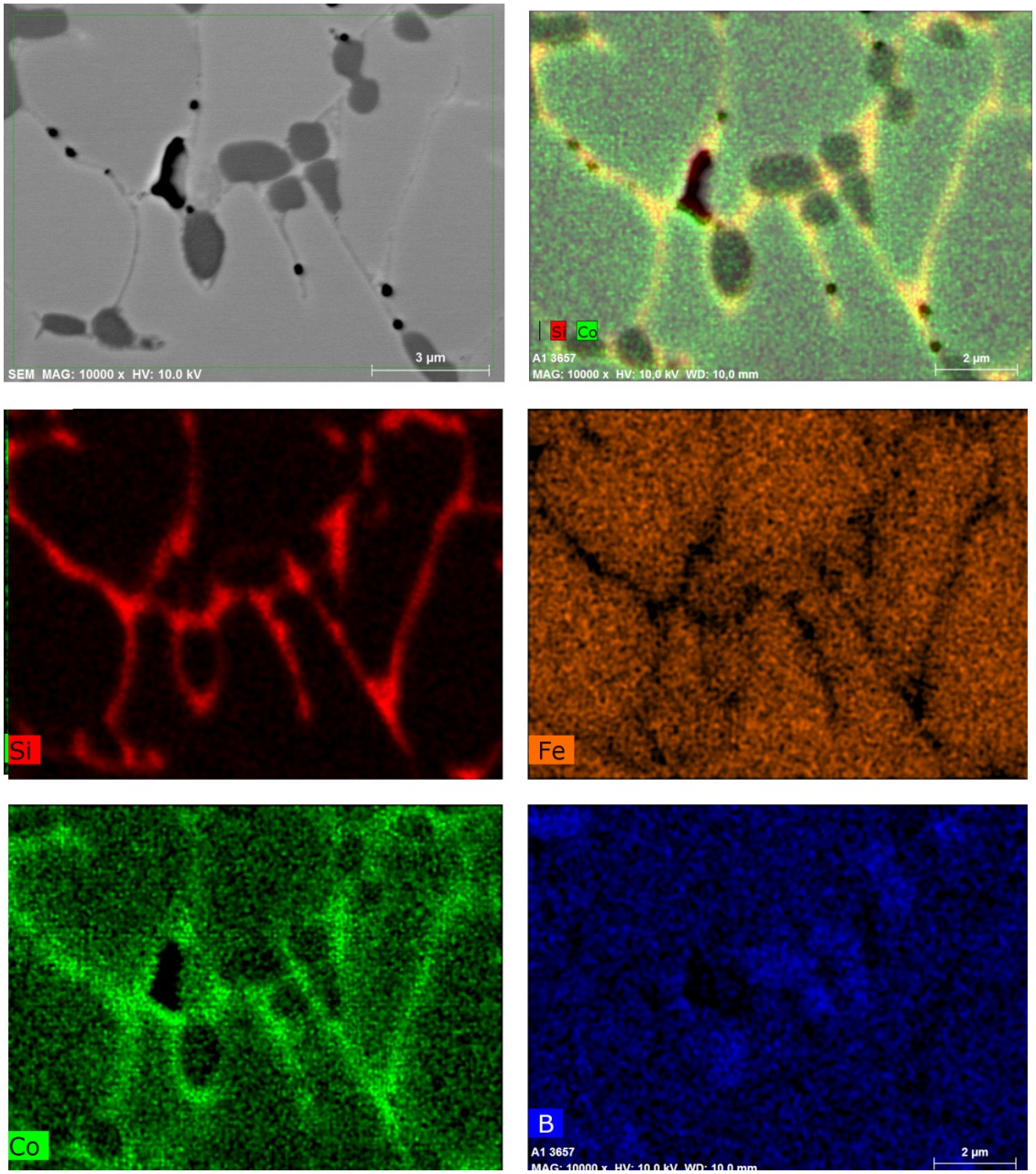

Figure 22: EDS mapping showing virgin image (top left), combined EDS response for Si and Co (top right) and EDS responses for Si (mid left), Fe (mid right), Co (bottom left) and B (bottom right).

A quantitative EDS was also done so as to highlight the differences between the grain boundaries, the dark precipitates and the gray mass. (*see fig. 23*) What can be seen here is an elevated level of Si in the dark precipitates.

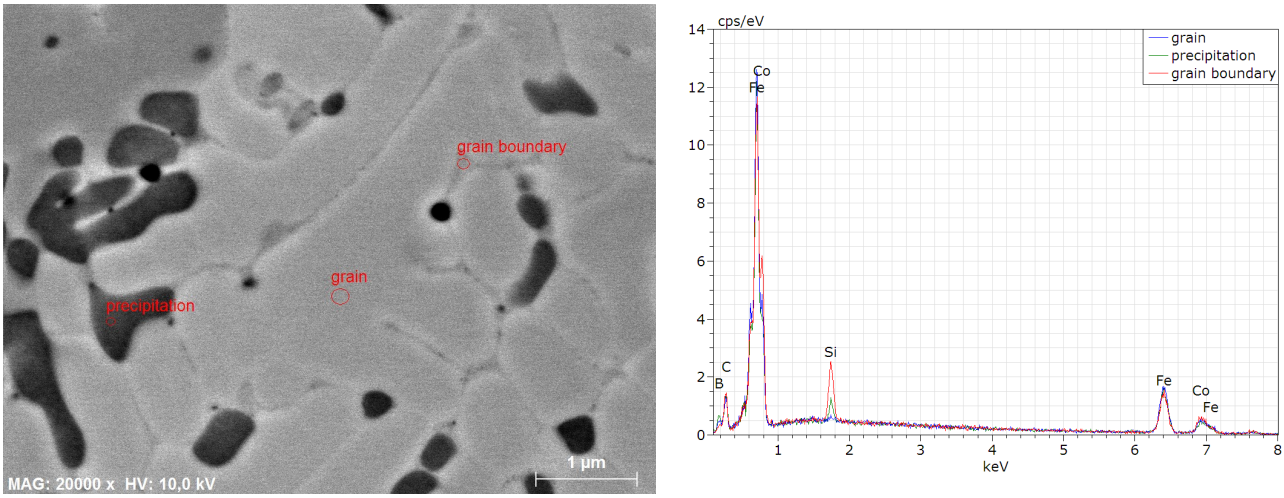

Figure 23: Quantitative EDS measurements in grain boundary, dark precipitate and gray mass.

Several images of the microstructure was also taken in an attempt to get resolution enough to see the microstructure of the particles with sub-micron grains that could not quite be resolved in the LOM. (*see fig. 37-38, p. 57*) In the image below, such an image can be seen where the microstructure can be seen to very similar to the microstructure of the other particles but on a much smaller scale. The slight shift in nuances of gray can be attributed to changing crystal directions of the different grains and the black dots are either pores or inclusions of a different phase. With the resolution being at its limit, it is difficult to deduce which.

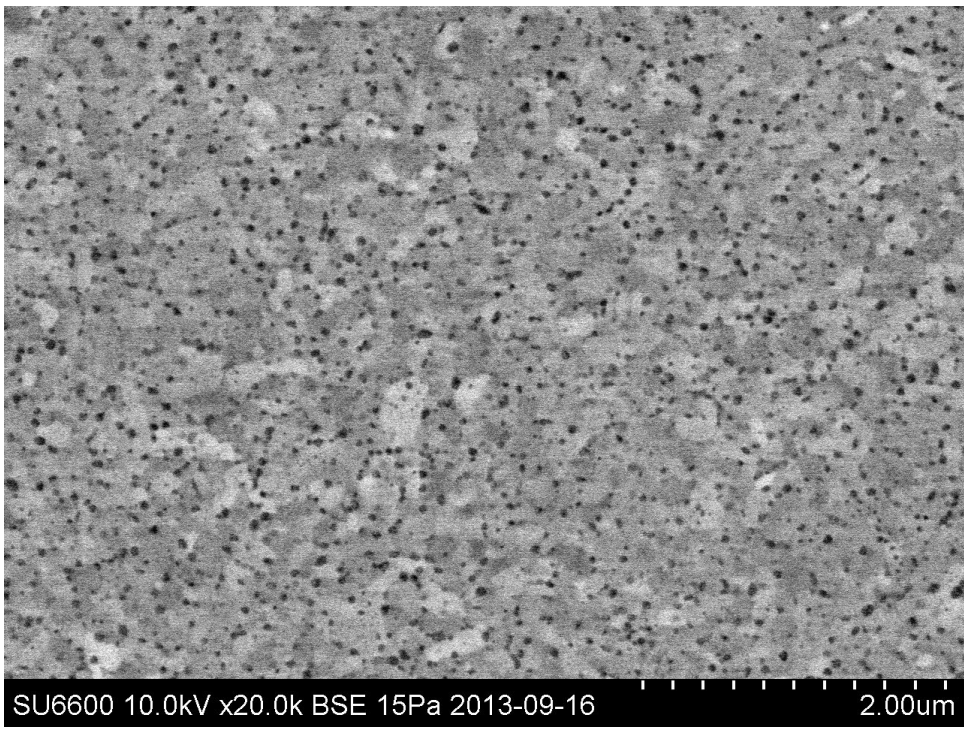

Figure 24: Cross sectional SEM image of a G336 particle with very fine microstructure and sub micron grains.

In order to get an idea of the particle shape of milled powders several SEM images were taken of the powder as this could be an important indicator to how quickly the morphology changes during a heat treatment. No significant change can, however, be seen in the morphology, possibly due to too short a heat treatment, but they still serve to show the morphology of double milled powders. (*see fig. 25-26*) As a comparison to this, SEM images of a single milled powder is presented showing less satellite particles and less agglomeration. (*see fig. 27*)

The SEM images were also used as a tool for approximatively determine the particle size of the milled powder. Form the images (*see fig. 27*) it can be determined that the particle size ranges from 300nm to 3µm for 5/20 -milled powders. The range of this is quite large as the particle size determination was made difficult by agglomeration. For the double milled powders (*see fig. 25-26*) the size range can be determined to be between 100nm and 5µm.

To compare the microstructure of the milled vs. the non-milled powder, several cross sectional SEM images were taken of milled powders. (*see fig. 28*) It can be seen here that the dark inclusions of the boron rich phase persist as well as significant fracturing of the particles with an abundance of satellites as a result. They also reaffirm the particle size ra1nge assessment from earlier.

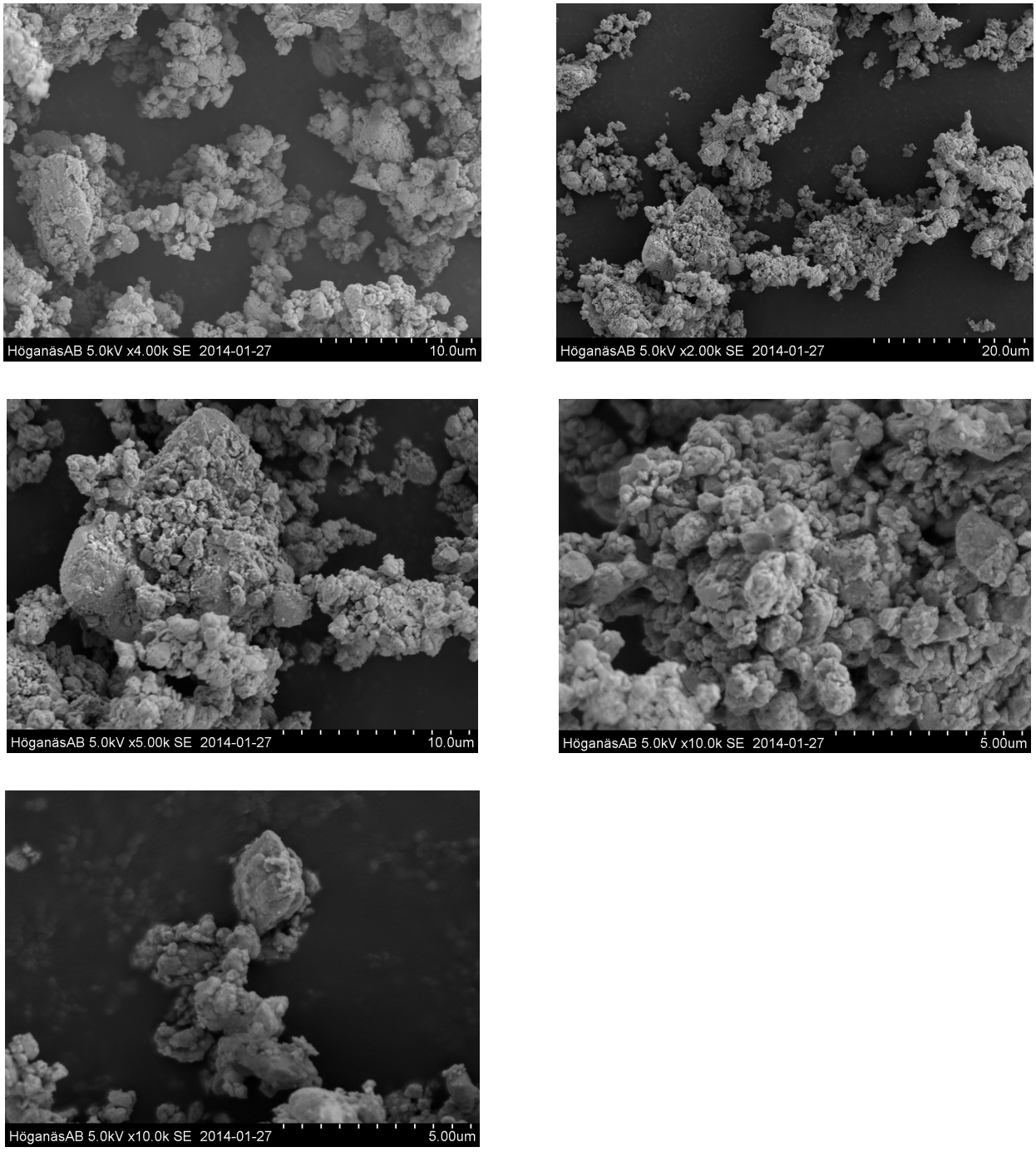

Figure 25: Milled (5/20 + 5/5) G336 powder of the <36µm fraction before annealing.

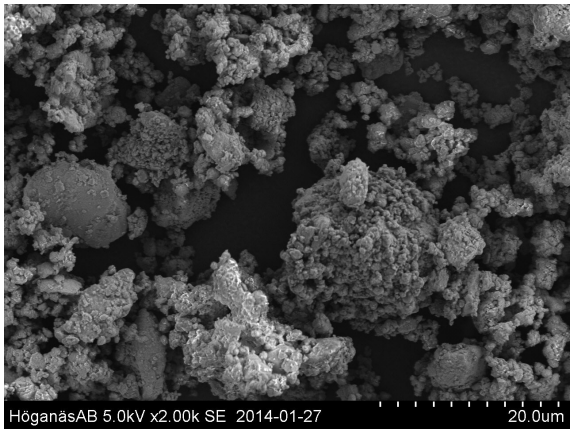

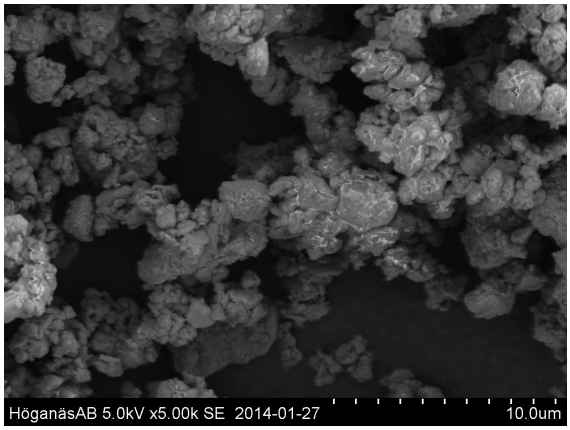

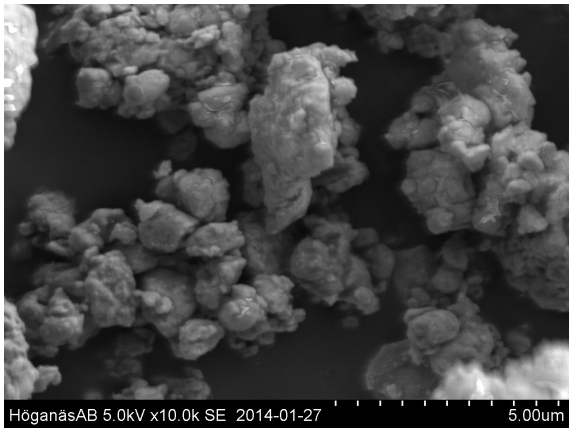

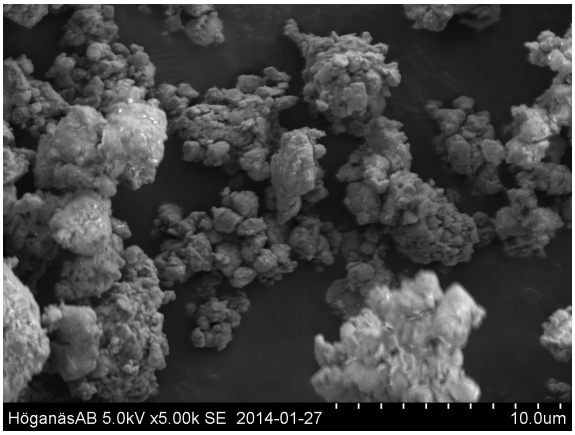

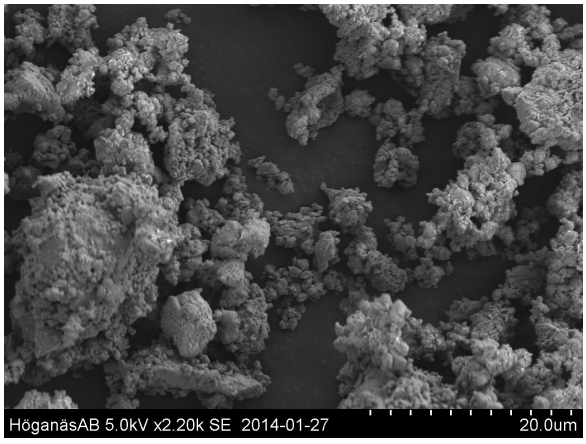

Figure 26: Milled (5/20 + 5/5) G336 powder of the <36µm fraction after annealing at 700^{O}C for 1h.

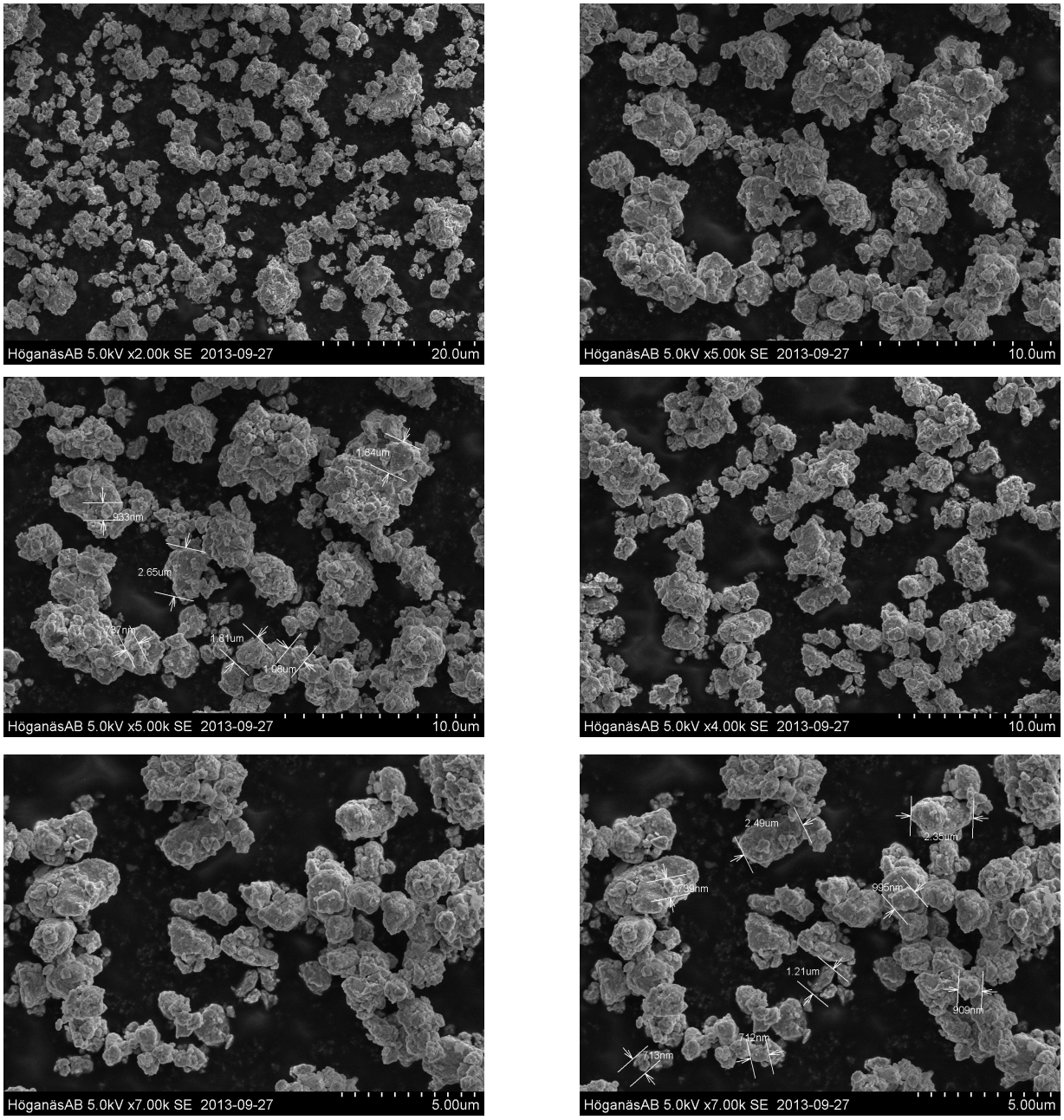

Figure 27: Milled (5/20) G336 powder of the 75-106µm fraction before annealing.

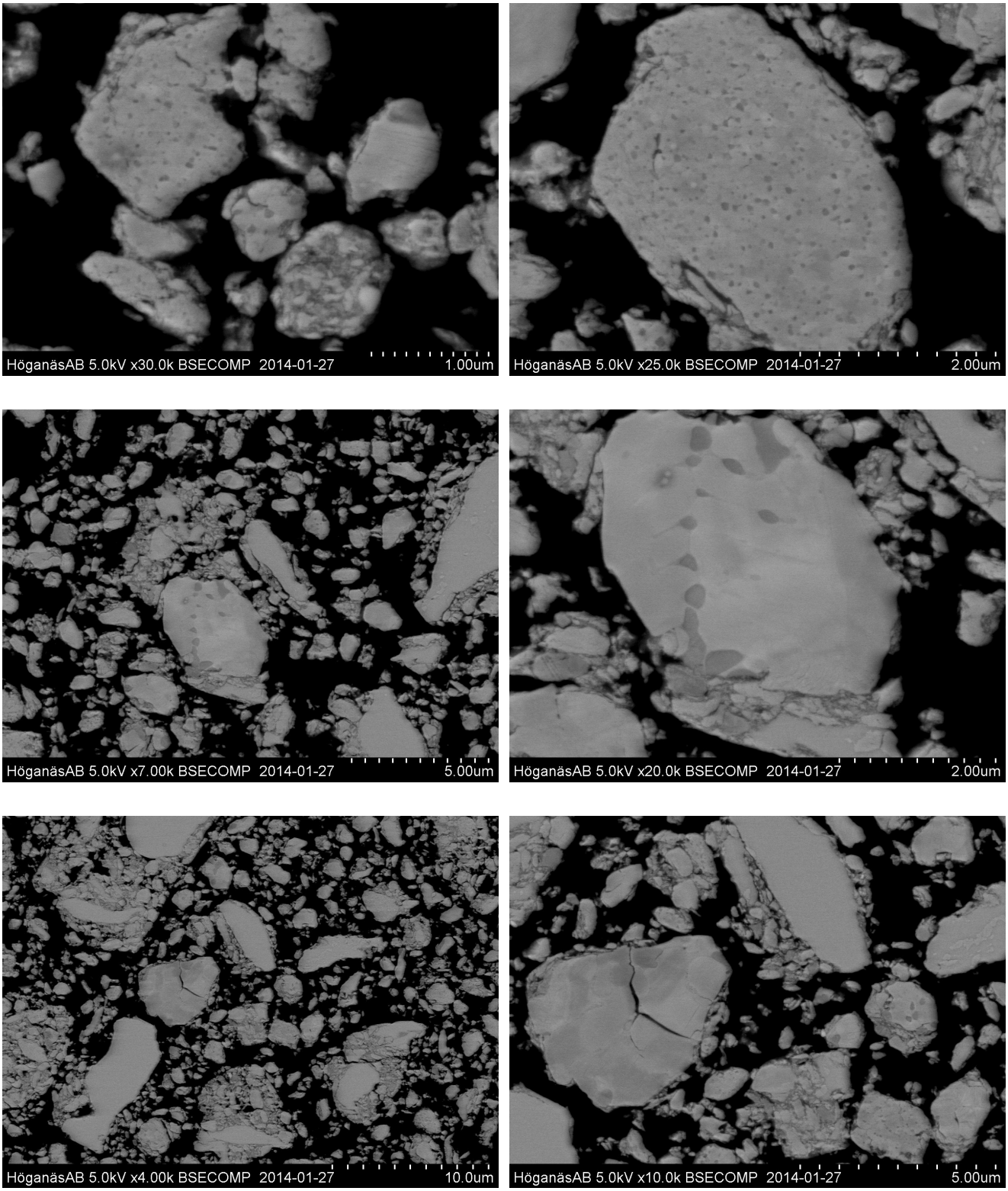

Figure 28: Cross sectional SEM images of double (5/20+5/5) milled G336.

6.6.2. G398

The more recent melts, G398 through G408, where less investigated in SEM due to lack of time but some analysis was made to get an idea of what the main characteristics of the powders was and how they differ from G336. As a representative of the newer powders, the G398 powder was chosen as this is atomized using the gas/water combined atomization method, has a slightly more accurate amount of boron in the melt and has a similar amount of silicon. What can be seen is a powder comprised of nearly perfectly spherical particles.

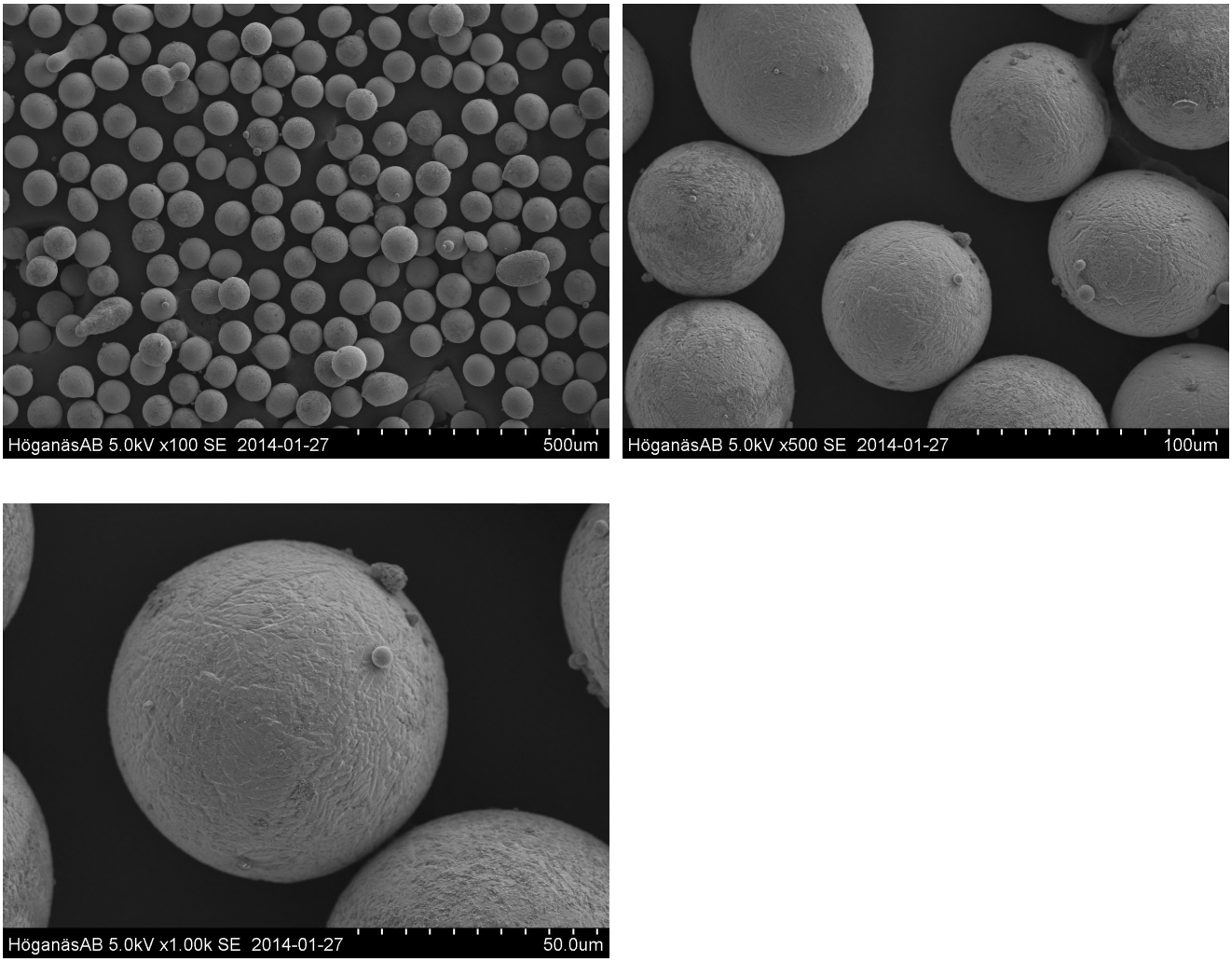

Figure 29: Particle view of the G398 powder of the 63-75µm fraction.

6.7. XRD

The results of the first analysis, aimed at illuminating the relaxation behavior and to determine the crystallite size and internal strain, can be seen in the table below. (Graphical representation can be found in the Appendix F.1.) They show distinct increase in crystallite size as well as a reduction in strain. This also gives some idea of what the crystallite size can be expected to be. One exception can be found in the relaxed 63-73µm sample.

Table 4: Results from the XRD measurements of the G336 powder.

	Milled					Relaxed			
Cryst Size	**<36µm**	**36-63µm**	**63-75µm**	**75-150µm**	**Cryst Size**	**<36µm**	**36-63µm**	**63-75µm**	**75-150µm**
[Å]					[Å]				
(020)	124	94	123	102	**(020)**	310	186	42	550
(002)	128	94	121	100	**(002)**	363	264	49	644
(121)	128	94	121	98	**(121)**	415	283	54	734
Strain	**<36µm**	**36-63µm**	**63-75µm**	**75-150µm**	**Strain**	**<36µm**	**36-63µm**	**63-75µm**	**75-150µm**
[%]					[%]				
(020)	1.02	1.35	1.03	1.24	**(020)**	0.41	0.87	3.02	0.23
(002)	0.82	1.12	0.87	1.05	**(002)**	0.29	0.40	2.12	0.16
(121)	0.78	1.06	0.82	1.02	**(121)**	0.24	0.35	1.85	0.14

The hydrogen heat treatment resulted in the crystal sizes presented in the figures below. It can be seen that the crystallite size go down with milling to less than 10nm in all cases regardless of the starting size. The relaxation process then allows them to grow again and to different sizes depending on relaxation temperature. This holds true for both particle size fractions.

The strain shows an inverse behavior to the crystallite size and in the data point spread. What can also be seen is that the initial strain is close to zero.

Compared to the previous relaxation experiment, the relaxation of the hydrogen treated samples appears to have an insignificant effect the grain growth. The increase in introduced strain can be attributed to the finer milling and is to be expected.

What can also be seen is a considerable spread in the data. The highest temperature heat treatment have not yielded the largest grains, nor has the lowest temperature yielded the smallest. This spread appears in both samples at all stages and appears to have an inverse relation between size and strain as well.

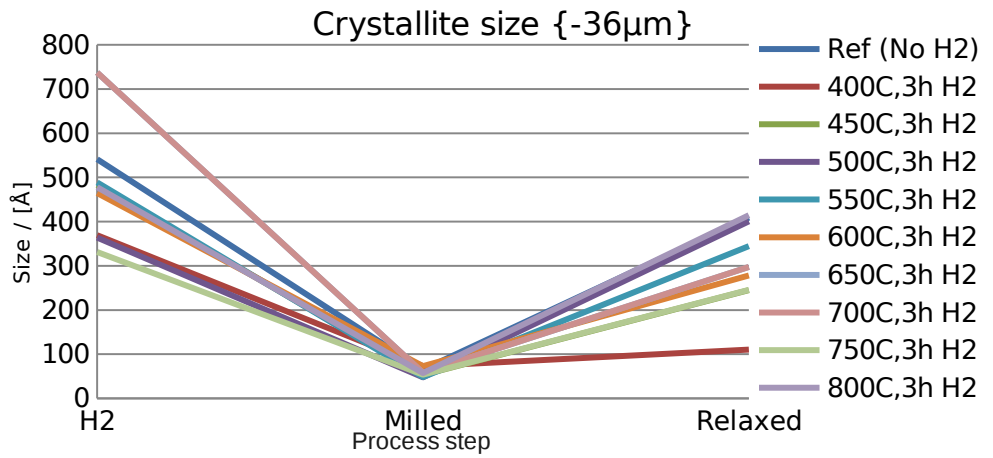

Figure 30: Crystallite size of the <36µm G336 material in each of the process steps.

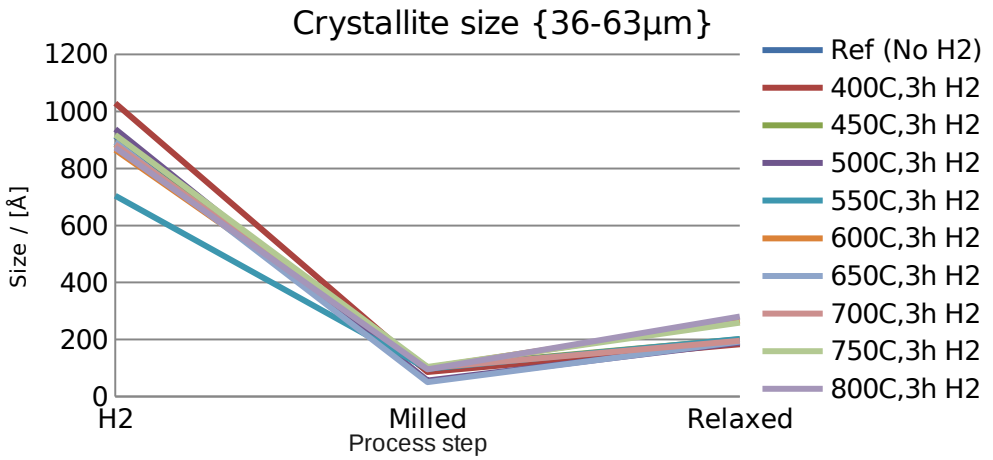

Figure 31: Crystallite size of the 36-63µm G336 material in each of the process steps.

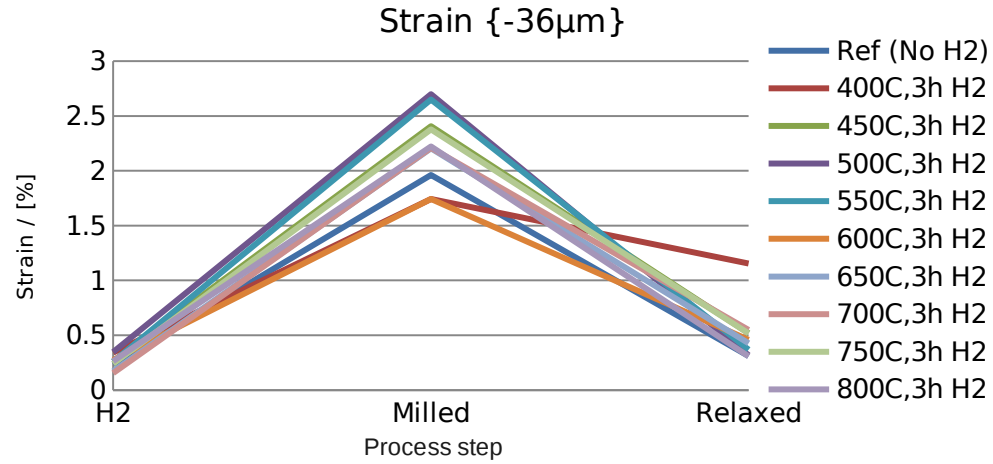

Figure 32: Internal strain in the <36µm G336 material in each of the process steps.

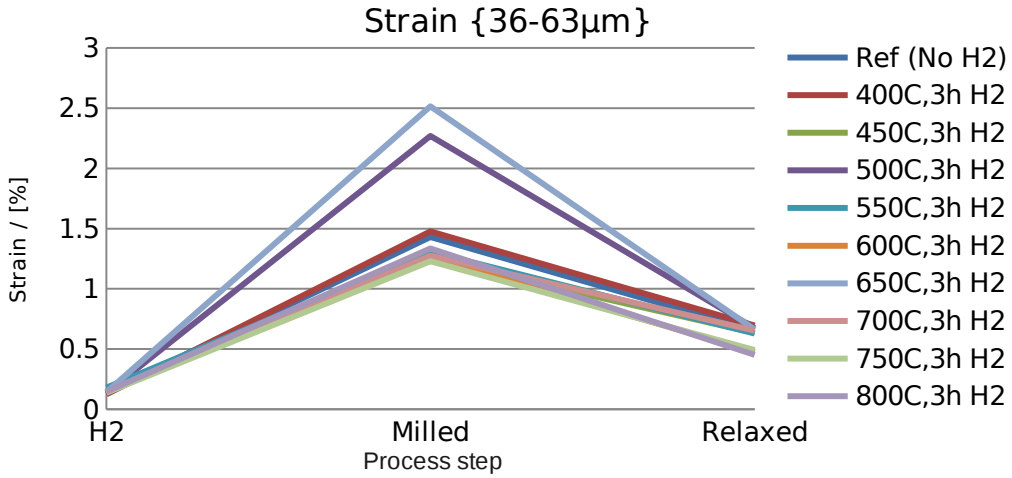

Figure 33: Internal strain in the 36-63µm G336 material in each of the process steps.

The XRD data for the hydrogen treatment tests were also used to determine the relation between the (Fe,Co)B and $(Fe,Co)_2B$ phases in G336. The results of this is presented in the tables below. (Profile fittings can be seen in Appendix F.2.) All cases of this show an increase in the desired phase $(Fe,Co)_2B$ and a decrease in (Fe,Co)B for hydrogen treated samples and after relaxation. It can also be seen that the milling and relaxation has yielded better results than hydrogen heat treatment only. The combination, however, yields the best results.

Table 5: Phase compositions as determined by XRD. 750°C is the hydrogen heat treatment temperature. Reference sample is not heat treated in H_2.

-36µm	**Hydrogenization of G336**		
After HT:		**Reference**	**750C**
	%Fe2B	85.96	91.82
	%FeB	14.04	8.18
After milling:			
	%Fe2B	58.99	80.94
	%FeB	41.01	19.06
After relaxation:			
	%Fe2B	93.33	98.44
	%FeB	6.67	1.56

Table 6: Phase compositions as determined by XRD. 750°C is the hydrogen heat treatment temperature. Reference sample is not heat treated in H_2.

36-63µm	**Hydrogenization of G336**		
After HT:		**Reference**	**750C**
	%Fe2B	86.84	92.75
	%FeB	13.16	7.25
After milling:			
	%Fe2B	83.92	91.71
	%FeB	16.08	8.29
After relaxation:			
	%Fe2B	95.77	96.78
	%FeB	4.23	3.22

A final XRD measurement series was performed on a new series of melts to determine what phases were present and in what amounts. The result of this is presented in the table below. (Profile fittings can be seen in Appendix F.2.) A significant part of this is the G400 and G408 material witch does not appear to contain any FeB or Fe_2B but is instead FeCo and $(Fe,Co)_3B_2$.

Table 7: Phase compositions as determined by XRD

	New melts						
-36µm	**G398**	**G399**	**G400**	**G401**	**G406**	**G407**	**G408**
%Fe_2B	96.27	98.07		93.64	95.73	95.53	
%FeB	3.73	1.93		6.36	4.27	4.47	
%FeCo			33.93				32.77
%$(Fe,Co)_3B_2$			66.07				67.23

6.8. VSM

Due to VSM availability, only a small selection of samples could be measured. In order to at least get an idea as to what the magnetic properties are for the different melts, a number of samples where selected, prepared and analyzed in a VSM. This yielded a number of hysteresis loops that where plotted and analyzed using MatLab.

In the table below, the coercive field, H_C, the remanent magnetization, M_R, and the saturation magnetization, M_S, are presented along with the energy product, $(BH)_{max}$. There is also a unit-less value of M_R/M_S that indicates, among other things, the hardness of the magnet and will be close to 100% for the theoretically perfect hard magnet. The plots of the hysteresis loops can be found in the appendix. (*see Appendix G*)

Table 8: Results of the VSM measurements, the sample description and treatment. Samples marked TEOS represents SiO_2 coated samples.

#	Material	Milling	Heat treatment	H_C / [kA/m]	M_R / [kA/m]	M_S / [kA/m]	$(BH)_{max}$ / [J/m³]	M_R/M_S
1	G336	5/20	3h @ 700°C	-27	117	1043	942.67	11.3%
2	G336	5/20 + 5/5	3h @ 700°C	-26	109	1103	796.42	9.9%
3	G336	5/20	3h @ 800°C	-22	83	1029	511.20	8.1%
4	G336	5/20 + 5/5	3h @ 800°C	-16	66	1146	389.93	5.7%
5	G336 (TEOS)	5/20 + 5/5	8h @ 800°C	-9	33	1225	99.25	2.7%
6	G336	5/20	3h @ 900°C	-13	51	1088	194.96	4.7%
7	G336	5/20 + 5/5	3h @ 900°C	-9	40	1208	118.89	3.3%
8	G336 (TEOS)	5/20 + 5/5	8h @ 900°C	-3	9	1388	15.28	0.7%
9	G399	5/20	1h @ 700°C	-19	84	1086	476.62	7.8%
10	G400	5/20	1h @ 700°C	-10	45	1423	144.80	3.2%
11	G401	5/20	1h @ 700°C	-16	63	1153	292.66	5.5%
12	G406	5/20	1h @ 700°C	-16	69	1129	342.23	6.1%
13	G407	5/20	1h @ 700°C	-21	89	1078	548.76	8.3%

In the hysteresis graphs (*see Appendix G*) it can be seen that all the samples show a soft magnetic behavior as both the remenance, M_R, and the coercivity, H_C, is low. (H_C > 400kA/m for hard magnets) The saturation magnetization, however, is high.

The samples with the lighter milling show degrading magnetic properties with increased heat treatment temperature. When compared to the heavily milled samples, it can be seen that the increased milling also degrades the magnetic properties.

The two samples treated with TEOS is expected to have a thin coating of SiO_2, intended to prevent sintering during the long heat treatments and worked perfectly to this effect. The results from the VSM, however, shows a deleterious effect on the magnetic characteristics. These samples, however, also have a significantly longer heat treatment time that, for the previous samples have shown a deleterious effect on the magnetic properties.

The lower Si contents of G401 and G406 appears to have had a slightly deleterious effect on the magnetic properties as well.

From the XRD analyses it was seen that the G400 material had none of the desired $(Fe,Co)_2B$. In this measurement as well, the G400 sample stands out as it has a significantly more soft magnetic behavior than the rest of the samples with exception for the ones treated with TEOS.

7. Discussion

7.1. LOM

With the data being as statistically unreliable as it is, the grain growth should be taken as qualitative. The particle counting to is statistically unreliable but shows that there is a large number of particles that has shown non-solid characteristics such as the bubbled particles. These are most likely formed during the atomizing process as a result of gas development within the molten droplets. It can also be seen that there is a large number of particles with a microstructure composed of sub-micron grains. These are especially numerous in the smallest size distribution. What has contributed to their unique microstructure is hitherto unknown but one hypothesis is that a number of the particles have suffered undercooling that resulted in a very rapid quenching.

The data collected from the image analysis macro should be regarded as a qualitative comparison between samples and what can be taken from this is that no discernible growth can be seen for these heat treatments and that the grain size seem to be increasing with increasing particle size. This is probably caused by the lower cooling rate allowing the grains to grow further during the solidification process.

7.2. STA

The DSC revealed a very small peak for all the non-milled powders except for the 36-63µm powder which showed no peaks at all. For the milled powders, only the <36µm powder showed a small exothermic peak whereas the rest did not. The peak shown in the <36µm fraction of the non-milled powder is very similar to the one found in the milled sample and can be assumed have the same cause.

Except for the 63-75µm sample that show no peak at all, the rest of the samples show slight exothermic peaks although with a more “smeared” profile. One hypotheses that could potentially explain this behavior is based on the diffusion of heat in particles of different sizes.

The peaks are likely to be a phase transition as the temperature in question represents a region of phase transition in the phase diagram produced by Thermo-Calc. (*see fig. 7, p. 12*) If the transition from one phase to the next represents a very small shift in potential energy, this could explain the small size of the peak. What phases are transitioned between is suggested in the phase diagram to be from $(Fe,Co)_2B$ to (Fe,Co)B.

The reason for the peak only showing up in the smallest fraction could be a result of extremely small particles in the fraction transitioning quickly as they have a more homogeneous temperature profile in the particle. The larger particles, however, begin their transformation from the outside and slowly and continuously transform, producing a smearing effect on the peaks.

The validity of the hypotheses is somewhat tempered by the fact that the peak for the 36-63µm non-milled powder is smaller, or more smeared than for the two larger fractions. No alternative explanation has presented itself, however, making this the only hypothesis at the moment. Exactly what phases are transitioned from and to, is difficult to tell but the theoretical phase diagram does offer a reasonable suggestion.

The comparison with the pure iron analysis supports the hypotheses further as the phase transition in the pure iron has a similar peak profile as the suspected phase transition in the G336 powder. This is, however, far from conclusive evidence as the phase transition yielded an endothermic peak for the Fe and an exothermic peak for G336. This does not exclude the possibility though.

Other than these very small peaks, a continuous change can be seen in the in the DSC. As this shows up in all the the measurements and of, mostly, the same character, this could be attributed to an instrumental error. There is one exception to this; the <36µm un-milled sample has a continuous positive slope. It is possible that this is a result of a continuous growth of the sub-micron particles. This hypotheses is countered by the increase in number of sub-micron particles found in the LOM experiment but as those results are questionable, it remains a possibility.

7.3 Dilatometry

The coinciding of the DSC and the dilatometry suggests a correlation between the two and thus supports the hypotheses explained in the previous section. It also suggests a possible onset temperature for the sintering around 600^{O}C. The accelerated shrinkage around 800^{O}C could be explained by the sintering entering a new stage in the process such as a neck forming in the 600-800^{O}C region and a neck growth or unification of particles at the higher temperatures.

7.4. Chemical analysis

The excess of boron in the G336 material could contribute to the formation of (Fe,Co)B as this phase benefits from a lower amount of boron. The other melts aimed at a stoichiometric composition resulted in compositions closer to target. Slight variations are present but this is to be expected as the raw materials used in the atomization aren't perfectly pure and some cross contamination between melts might have occurred.

The reduction of the oxygen levels, seen in the gas atomized – water quenched samples, was to be expected as an inert gas atomization introduces less oxygen to the powder while in a hot state and thus reduces the amount of oxides being able to form.

7.5. Etching

The lack of correlation between the oxygen level and the variables suggest that etching had no tangible effect on the powder and thus that the oxygen is not localized at the surface of the particles. The DSC analysis of the etched powder show a reduced onset temperature for the exothermic peak, suggesting that the etching could have changed the composition of the sample and thus shifted the phase transition.

To find possible causes for the low grain growth other methods, such as an EDS mapping, should be employed. There may, however, be some large variations in the oxygen concentration from the etching experiments as the concentration is, for one of the samples is ~0.9% and the analysis of the material indicates that the initial oxygen level is only 0.45%. (*see tab. 1*) It is therefor reasonable to conclude that some experimental errors may have occurred.

7.6. SEM

In the EDS mapping for G336 dark inclusions can be seen throughout the microstructure. As darker color is indicative of lighter compounds this could potentially be FeB or some variant of $Fe_{1-x}B_x$. There is, however, an elevated level of Si in the dark precipitates (*see fig. 23*) that might indicate that they may be a result of the elevated levels of Si in the material composition. (*see tab. 1*) The Co and Si focusing in the grain boundaries could potentially be a cobalt silicide ($CoSi_2$, Co_2Si or CoSi) but this is unconfirmed conjecture and should be analyzed further as this could be hindering the grain growth.

From the powder images it can be seen that the milled G336 powders present significant fractioning (*see fig. 25-28*) and, hence, a large amount of fine particulates that agglomerate with the larger particles. This appearance could make it difficult to obtain a crystal growth from the milled powders that would produce single crystal powders with a particle size of <300nm. Though there are a lot of particles that are in the correct size range, the agglomeration will most likely result in a reunification of the particles during a heat treatment that is long enough to obtain a single crystal powder. Thus, the SEM images suggest that the alternative strategy of heat treating for crystal growth prior to breaking the particles up by the grain boundaries could be the better choice for this project.

The SEM image of the G398 powder mostly illustrates the roundness of the particles and explains the feeling of the powder as it has much better flow than the G336 powder. This might be a good candidate for the alternative strategy of having crystal growth first as the particles would be somewhat less likely to agglomerate.

7.7. XRD

The 5/20-milling of the G336 material has shown to yield 100-150Å crystallites and the double milled (5/20 + 5/5) powder ~50Å crystallites. (*see tab. 4*) This is to be expected, as is the increase in internal strain when milled and reduction when relaxed by heat treatment. This is seen in all samples and from the initial size difference in the hydrogen treated powders, the fact that they all yield roughly the same crystallite size after milling suggests an asymptotic behavior of the milled crystallite size.

It should be possible to estimate the number of grains per particle from this by relating it to the particle size. The particle size, however, is not so easily determined for milled powders as they produce a lot of satellite particles, thereby expanding the range of particle sizes. An estimation from the SEM images (*see fig. 25-28*) places the particle sizes in the rang of 0.1-5 µm for the double milled powders and 0.3-3 µm for the single milled (5/20). This places the number of grains per particle at 10-1'000'000 for the double milled and 30-8000 for the single milled powder. These are very rough estimates and a better method for the determining of the particle sizes should be employed in future to minimize the variance. The gigantic variance in the double milled powder is a direct result of the size range from the minuscule satellites to the larger, cracked particles.

Relaxation of the hydrogen treated, milled samples yields a growth that appears to be proportional to the relaxation temperature, just as would be expected. Some variation in this trend can be seen (*see fig. 30-31*) but can be ascribed to variations in the XRD measurements or the profile fitting.

The inverse behavior of the strain to the crystallite size was also to be expected but the inverse spread of the strain measurements was somewhat unexpected. (*see fig. 32-33*) What would be expected is a strain that mimics the inverse behavior of the crystallite size in spread.

The crystallite growth seen for the hydrogen heat treated material (*see fig. 30-31*) did not yield a crystallite size that exceeds the pre-milled state. The growth rate, however, appears significant for the <36µm sample but less so for the 36-63µm sample. As there seems to be significant statistical error in these results (indicated by the inconsistent spread) it is difficult to draw any conclusions from this data. What can be concluded is that there has been a crystal growth, although not quite as rapid as had been hoped for, and if the most conservative of the growth rates is presumed correct, a linear extrapolation places the 200 nm crystallites at 155 hours at 400^{O}C. This, however, assumes a linear behavior which is most likely an oversimplification but the only assumption that can be made with the data currently available.

From the analysis of hydrogen heat treated G336, it can be seen that there is an increase in concentration for Fe_2B with the hydrogen heat treated sample compared to the reference sample. There is also an increase in the Fe_2B concentration from the relaxation heat treatment. The increase from the relaxation can be explained by the phase diagram. (*see fig. 7*) If the sample is heat treated there is an induced diffusion resulting in the more stable phase to grow at the expense of the less stable one.

The increase from the hydrogen heat treatment is most likely a result of the same process. The reference sample, having had less total heat treatment, simply has had less time to transform less stable FeB into Fe_2B as the reference sample was not heat treated at all prior to milling. Notable here, though, is the greater transformation from FeB to Fe_2B with milling and relaxation compared to the hydrogen heat treatment, despite the large difference in heat treatment time and temperature. This suggests that milling plays a vital role in the growth of the desired phase. One hypotheses is that the milling breaks up the grain boundaries and the Si-Co formations that is possibly hindering the grain growth.

The most conclusive result of the XRD of the new melts is the G400 and the G408 materials that show no presence of FeB or Fe_2B but shows instead FeCo and $(Fe,Co)_3B_2$. This can be explained by the reduced amount of boron in the chemical makeup of these two melts. This reduction in boron would render the $(Fe,Co)_2B$ unable to form as there is simply too little boron. It can thus be deduced that the eutectic composition does not yield a better phase composition than the stoichiometric composition.

It should be noted that the milled samples have a larger uncertainty in their XRD analysis as the XRD data from

these samples contained significant noise levels that can skew the results slightly. Still, the pattern of increasing Fe_2B after heat treatment remains, suggesting the heat treatment is turning (Fe,Co)B into $(Fe,Co)_2B$.

7.8 VSM

The soft magnetic behavior evident in the hysteresis graphs (*see fig. 80-92*) could be due to a failing magnetocrystalline anisotropy. This can in turn be due to factors like, not enough of the $(Fe_{0.7}Co_{0.3})_2B$ has formed but has instead formed pure iron phases or (Fe,Co)B phases. It could also be that the $(Fe_{0.7}Co_{0.3})_2B$ just doesn't have enough anisotropy in it self.

As the domain structure is the factor responsible for keeping the magnetization in place after saturation, this could be caused by a domain structure that, far too easily returns to a structure close to the starting structure, or perhaps a pinning of the domains from the start so that a unified domain in the particles is never achieved to star with. The former is most likely though, as the good saturation magnetization would most likely not have been so good if the domains were working in the opposite direction to the magnetizing field.

One possible explanation for the better results of G336 compared to the other samples, could be that it has a better pinning of the domain structure after saturation. The SEM images show the presence of precipitate phases heavy in boron concentration that could possibly be a source of such a pinning. (*see fig. 25-27*)

From the eight samples of G336 tested in the VSM, the sample with the least milling and the least heat treatment time has proven to hold the best magnetic properties. It can also be seen that increased milling appears to have a slight negative effect whereas increased heat treatment results in significant loss of coercivity. The behavior also appears consistent throughout all the samples.

The milling resulting in lowered magnetic properties might be explained by nucleation of magnetic subdomains. The behavior of the heat treated samples, however, is quite counterintuitive as the heat treatment has been shown by XRD to have a positive effect on the concentration of the desired phase. A valid hypotheses as to what the reason for this behavior continue to elude. A continued study of this behavior should yield some more insight.

If the material could be prevented from losing its magnetization through some process and a M_R/M_S ratio of, say 50% could be achieved, the remanence, M_R would be on the order of 500kA/m (or 0.628T). In order to reach the goals set forth at the start of this project of $(BH)_{max}$ of 150kJ/m³, both H_C and M_R must be high. With the M_R at 0.628T, the H_C must then be roughly 240 kA/m, assuming an optimal (square from M_R to H_C) hysteresis. The measured samples all had an H_C less then 30 kA/m and no material will ever reach a prefect hysteresis. The required H_C must thus be significantly higher than 240 kA/m or the M_R must be significantly higher.

The samples that were coated using TEOS showed clearly lower values for all measured values except for the saturation where they instead showed slightly increased values. One might think that this is a result of a hindered diffusion process during the heat treatments but as heat treatments have proven deleterious to the magnetic properties this hypothesis seems disproved. There is, however, no current competing hypothesis.

The samples with lower amounts of silicon (*see tab. 1 and 8*) appears to have a minimal effect on the magnetic properties. Considering the relatively small difference in magnetic properties a conclusion about the effects of silicon on the magnetic properties is premature.

The samples with bubbles in the particle structure appears to have no influence at all on the magnetic properties. This could be an effect of the milling fracturing them resulting in the absence of bubbles in the samples when measured upon. What effect the bubbles could have is, with the collected data, difficult to say but it seems likely to be minimal as the magnetic properties should only depend on the structure and orientation of the grains.

8. Conclusions

Microstructure

- Grain growth in these materials appears to be a slow process as has been seen in the XRD analysis. The spread of the apparent growth rates, however, makes it an unreliable conclusion although it does show an encouraging growth rate for some samples. At least up to the point from which the powders were milled. Beyond that point only the LOM data is available but is also inconclusive.
- The bubbles in the particles appear not to have any effect at all on the magnetic properties as no dependency can be seen in the VSM results.
- The number of grains per particles is still not reliably determined but estimated values show a relatively high number. (Up to 1'000'000) Significant grain growth is thus still required to reduce this to a level where little canceling of the domains remain.

Material chemistry:

- From the phase analysis in the XRD it is reasonable to conclude that the eutectic composition found in the G400 and G408 material yields almost exclusively unwanted phases. The material should therefor have a melt composition as close as possible to the stoichiometry of the wanted phase, $(Fe_{0.7}Co_{0.3})_2B$.
- The phase composition of the materials appear to shift towards the wanted phase when heat treated. It appears not to matter if it is done in inert gas or H_2. This should therefor be taken advantage of in future heat treatments.
- The amount of Si and Co found in the grain boundaries could signify a cobalt silicide having formed. This might not have an affect on anything other than the grain growth but might, for that reason, want to be avoided in the future. No significant effect could be shown on the magnetic properties of the more Si rich powder though.
- Breaking apart the grain boundaries appear to improve the increase in phase purity of the desired phase, supporting the hypotheses of a cobalt silicide hindering the diffusion in the grain boudaries.
- No oxides could be proven to exist on the particle surface but DSC of the etched material did strengthen the hypotheses of the phase transformation at around $550^{O}C$.

Phases of the material

- All melts except for G400 and G408 all have a very high concentration of the wanted phase (>90%) and appear to get even higher concentrations with heat treatment as previously concluded.
- DCS revealed a phase transition at around $550^{O}C$ and it is likely that this is a transition from $(Fe,Co)_2B$ to (Fe,Co)B. If this proves correct in the future and the $(Fe,Co)_2B$ is the one stable at room temperature, future heat treatments should be cooled slowly to allow for compete formation of the unstable phase to the stable phase.

Magnetic properties

- The best hard magnetic properties can be found in the least milled and least heat treated G336 material. There is then found a consistent reduction in magnetic properties as the material is heat treated and/or milled. This is counterintuitive at heat treatments should yield a more pure $(Fe,Co)_2B$ phase and thus better anisotropy and better magnetic properties. No applicable hypotheses has been found but a closer investigation of this is might yield one. The milling, however is explained by the introduction of defects that might have nucleated magnetic subdomains.
- Since all samples measured in the VSM, save G400, had a high concentration of the desired phase, the phase concentration should yield no effect on the VSM results. The main difference between them being

the microstructure, leads to the conclusion that this is the main factor for the variations in these results.

- TEOS treated samples has yielded poor magnetic properties. One hypotheses is that the SiO_2 is interfering somehow with the materials magnetic properties. Precisely how, is not known. The second hypotheses is that the vast increase in heat treatment time follows the rest of the samples suggested path, that magnetic properties deteriorates with increasing heat treatments.

9. Future research outlook

This work could be further researched in many areas that have been initiated in this work and several areas that lie outside the limitations of it. The following points are areas that have presented themselves in one way or another throughout the research done in this thesis.

- The newer melts presented after G336 should be investigated further for more clues regarding the dependency of the magnetic behavior on the different chemical compositions and atomization techniques.
- Other alloys than the ones presented should also be investigated as it is possible that a better anisotropy could be found. The Fe-Co-C alloy is one candidate that has been suggested and shows theoretical promise but there could be others as well.
- There could be other analyses, besides the ones done in this work, that could be of significant interest such as BET to determine the surface area of the particles and comparing to the amount of SiO_2 present after TEOS treatment and thus calculating the thickness of the SiO_2 coating. This might yield clues as to why the TEOS treatment resulted in such poor magnetic porperties.
- The average particle size for all powders should, in future work, be done using a method like BET that can measure on a large number of particles to get a more accurate estimate.
- In the project goals there is a requirement of electrically insulating coating of all the grains in the finished material. This has only been tangentially brought up in this thesis but will eventually become more important as the particles come closer and closer to being single crystals and the magnetic characteristics of the powder improves.
- The need for electrically insulated particles makes the sintering of a the powder problematic as this would make the particles (grains in the finished product) grow and thereby risk becoming to large and ruining the magnetic properties. As the particle microstructure is developed and products are to be made from the powder, a bonding agent might be preferable to sintering. This bonding agent can than also act as an insulator of the particles (grains).
- Using TEOS could, despite the bad VSM results, be relevant for obtaining a strong crystal growth in the spherical, non-milled powder of the new melts. This would allow for long term exposure in the furnace so that the grains may grow as thermodynamics predict. Long term being on the order of a week or two at 900 to 1000C, above the temperature that the DSC shows represents a change in phase, assuming this is the desired phase and not the one below that temperature. The powder must then be cooled very slowly so as to allow for complete transformation of the (Fe,Co)B phase to $(Fe,Co)_2B$.
- The phases that are transitioned between around $550^{O}C$ should be investigated to find exactly what those phases are. Knowing this would aid in the design of the powder treatments to obtain the anisotropic phase. This could be done with an XRD measurement performed while the sample is heated in situ. This would illuminate the suspected phase transitions at around $550^{O}C$ as the precise phases could be determined in XRD analysis.
- As the phase diagram suggests a stable (Fe,Co)2B under $550^{O}C$, a heat treatment should be attempted at a temperature around $500^{O}C$ for a prolonged time such as a two-week period. Long term heat treatment of very finely milled powders might just produce the desired purity of (Fe,Co)2B as well as a healthy crystal growth. If the sample is also milled more vigorously there might be less of the large particles to absorb the small satellites during heat treatment and thereby crating a better basis for the production of single crystal particles in the correct size range.
- The possibility of a cobalt silicide having formed in the grain boundaries should be looked into as well, and potential means of counteracting the formation of it, if it is so. This could tentatively be quantified using a point EDS analysis and comparing the relative amounts of the elements to the stoichiometry of

the most likely silicides.

- The powders treated with TEOS should be investigated in a SEM with EDS mapping to find where the TEOS is located exactly. This could yield vital clues as to the cause of their low coercivity.
- Use an alternative strategy for production of single crystal powder where the crystals are allowed to grow by heat treatment first and then broken apart at the grain boundaries by some process. The challenge will be to break up the particles by the grain boundaries without fracturing the crystals and thus producing a polycrystalline powder again.
- A cross section and EDS mapping of the G398 powder for more complete comparison with the G336 powder should be done. This could also show what effects the altered chemistry has had with regard to Si and Co gathering in the grain boundaries and precipitations.

10. Possible sources of error

LOM:

- Distribution of particles in the pellets not homogeneous and thus having the same level of magnification is not enough to get a reproducible result.
- Manual counting not reliable as the chance of human error is high and the number of particles counted very limited.
- Grain growth assumes that some grains would be consumed by the neighboring grains. This, however would require a much longer heat treatment. Therefor, no conclusion can come from the grain growth test.

STA:

- Trace amounts of air that might have remained during the experiment could affect the results and thrown of the measurements.
- As the peaks are very small and in some cases, almost impossible to see, there is a possibility of misinterpretation.

Dilatometry:

- As with the STA, trace amounts of air might have remained during the experiment and could then affect the results.
- The standard used for the correction file and the actual sample measured on differed slightly in length (<1%) which could potentially yield a slightly larger thermal expansion than what was expected in the correction file.

Etching:

- The practical handling of the chemicals and powder for the etching process might not be optimal and could yield oxygen levels that are not entirely correct when later analyzed.
- The software analyzing the results from the chemical analysis was only recently introduced and handling errors should not be completely discounted.

SEM

- The evaluation of particle size is virtually impossible from the SEM imaging. This should instead be performed using BET or some other method that measures the average of a large number of particles. The SEM images could, however, still be useful as an indicator of the size range.

XRD:

- There is a possibility of erroneous measurements from the preparation of the samples in terms of sample flatness.
- The noise level of the milled samples can have skewed the XRD analysis as the software is less able to accurately fit each part of the graph to the specific phases.

VSM:

- Some samples fell out during the measurements. These were later discarded but there is a possibility of a small part of a sample falling out. This would, however, be immediately visible in the hysteresis loop if a significant portion of the sample fell out.

- The samples were cast in clear nail polish so as to keep the particles from rotating in the strong magnetic field. If some of the sample was not reached by the nail polish, this part might have rotated during measurements and not registered that part of the sample in the hysteresis or at least very weakly. It would, however, still show up as a part of the saturation M_S.

10. References

[1] J. M. D. Coey, *Hard Magnetic Materials: A Perspective*, IEEE Transactions on Magnets (2011); 47, pp.4671-4681.

[2] Conversation with Nils Pahlbäck at Sura Magnets, Sweden

[3] C. Jo, *Magnetic Properties of $Fe_{(1-x)}Co_x$ Nanowires Inside a (6,6) Carbon Nanotube*, Journal of Physics D: Applied Physics; 42 (2009), 6pp.

[4] J. Fidler et. Al & W. Coene et. al., *Magnetocrystalline Anisotropy of Fe_3B, Fe_2B and $Fe_{1.4}Co_{0.6}B$ as Studied by Lorentz Electron Microscopy, Singular Point Detection and Magnetization Measurements*, Journal of Magnetism and Magnetic Materials (1991); 96, pp. 189-196.

[5] A. Iga, *Magnetocrystalline Anisotropy in $(Fe_{1-x}Co_x)_2B$ System*, Japanese Journal of Applied Physics; 9 (1970), pp. 415-416.

[6] Y. Q. Liu, *Thermodynamic Optimization of the Boron-Cobalt-Iron System,* Journal of alloys and Compounds; 509 (2011), pp. 4805-4810.

[7] K. Gunnarsson, Presentation: *Höganäsmöte*; Presented at Höganäs AB, 13-01-10.

[8] B. D. Cullity & C. D. Graham, *Introduction to Magnetic Materials*, 2:nd Ed*;* Wiley (2009).

[9] J. M. D. Coey, *Magnetism and Magnetic Materials*; Cambridge University Press (2010).

[10] Conversation with Yvonne Andersson, Uppsala University.

[11] R. C. O'Handley, *Modern Magnetic Materials – Principles and Applications;* Wiley (1999).

[12] O. Gutfleisch, *Magnetic Materials and Devices for the 21st Century: Stronger, Lighter and More Energy Efficient"*, Advanced Materials; 23 (2011), pp821-842.

[13] R. DeHoff, Thermodynamics in Materials Science, 2nd Ed; Taylor & Francis Group (2006)

[14] G. S. May & S. M. Sze, *Fundamentals of Semiconductor Fabrication;* Wiley (2004)

[15] W. D. Callister, Jr., D. G. Rethwisch, *Fundamentals of Materials Science and Engineering*; Wiley (2008).

[16] R.E. Smallman, A.H.W Ngan, *Physical Metallurgy and Advanced Materials*; 7th ed., Elsevier (2007).

[17] L. Takács et. al., *Mössbauer Study of the Intermetallic Compounds $(Fe_{1-x}Co_x)_2B$ and $(Fe_{1-x}Co_x)B$*, Journal of Physics F: Metal Physics; 5, pp.800-811, 1975.

[18] O. Fabrichnaya, *Thermodynamic properties – Ternary Alloy Systems: Phase Diagrams, Crystallographic Data and thermodynamic data – Iron Systems, Part 1*; Springer (2008)

[19] J. Nowacki et. al., *Structures and properties of Fe-Fe_2B cermets*, Journal of Material Science; 27 (1992), pp.3651-3656.

[20] J. Nowacki, *Polyphase sintering and properties of metal matrix composites*, Journal of Materials Processing Technology; 175 (2006), pp.316-323.

[21] W. R. Osório et. al. *Electrochemical corrosion behavior of gas atomized Al-Ni alloy powders*; Electrochimica Acta, 69 (2012), pp.371-378.

[22] R.M. German, *Powder Metallurgy Science*; 2nd Ed., MPIF (1994).

[23] S. Kontos, Master thesis: *New permanent magnets for environmentally friendly energy production*; Uppsala University (2013).

[24] M. D. Kuzmin, *Towards high performance magnets without rare earths, Journal of Physics: Condensed Matter, 26 (2014), 064205 (5pp.).*

Appendix

A. Phase diagrams

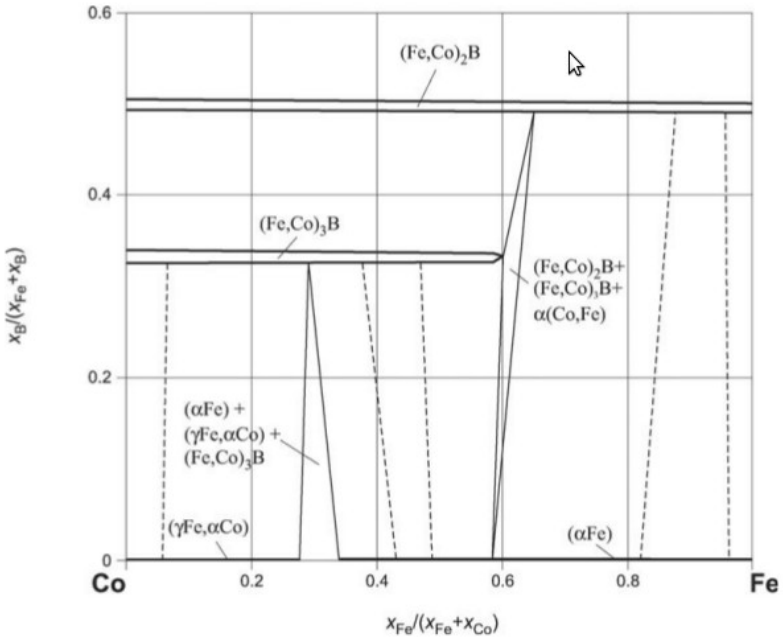

Figure 34: Ternary isothermal at 900^{O}C for Fe-Co-B. [O. Fabrichnaya, Thermodynamic properties – Ternary Alloy Systems: Phase Diagrams, Crystallographic Data and thermodynamic data – Iron Systems, Part 1; Springer (2008)]

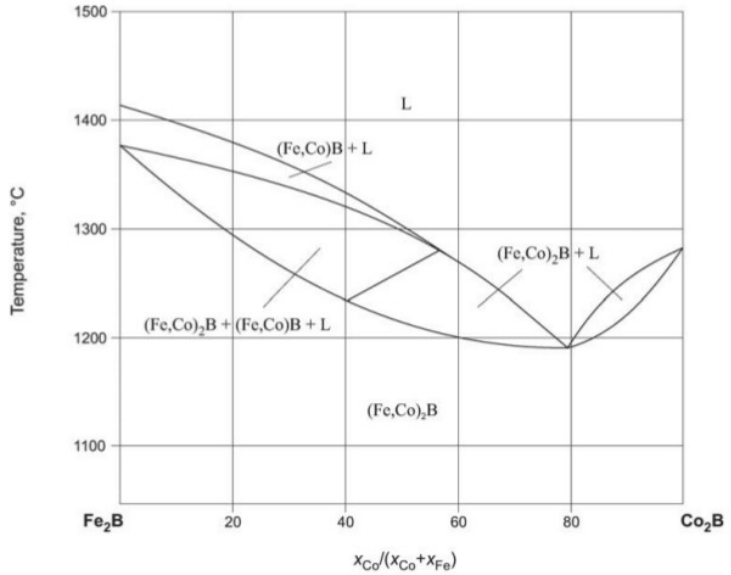

*Figure 35: Phase diagram of Fe2B - Co2B relation showing complete solubility under 1190^{O}C and an initial melting temperature of ~1190^{O}C. [*O. Fabrichnaya, *Thermodynamic properties – Ternary Alloy Systems: Phase Diagrams, Crystallographic Data and thermodynamic data – Iron Systems, Part 1*; Springer (2008), p.15*]*

B. Sieving distributions

Table 9: Particle size distribution from sieving of G336.

Sieving of 500g G336		
Particle fraction [µm]	**Mass [g]**	**Distribution (498.49g)**
>106	69.61	0.14
75-106	63.25	0.13
63-75	28.00	0.06
36-63	59.21	0.12
<36	278.42	0.56
Sum	498.49	1

Table 10: Particle size distribution from sieving of G398.

Sieving of 100g G398		
Particle fraction [µm]	**Mass [g]**	**Distribution (99.73g)**
>106	11.08	0.11
75-106	13.54	0.14
63-75	7.47	0.07
36-63	18.61	0.19
<36	49.03	0.49
Sum	99.73	1

Table 11: Particle size distribution from sieving of G399.

Sieving of 100g G399		
Particle fraction [µm]	**Mass [g]**	**Distribution (99.79g)**
>106	7.62	0.08
75-106	6.98	0.07
63-75	3.59	0.04
36-63	9.90	0.10
<36	71.70	0.72
Sum	99.79	1.00

Table 12: Particle size distribution from sieving of G400.

Sieving of 100g G400		
Particle fraction [µm]	**Mass [g]**	**Distribution (99.74g)**
>106	10.97	0.11
75-106	10.43	0.10
63-75	5.37	0.05
36-63	13.65	0.14
<36	59.32	0.59
Sum	99.74	1.00

Table 13: Particle size distribution from sieving of G401.

Sieving of 100g G401		
Particle fraction [µm]	**Mass [g]**	**Distribution (99.84g)**
>106	10.14	0.10
75-106	8.59	0.09
63-75	4.18	0.04
36-63	11.20	0.11
<36	65.73	0.66
Sum	99.84	1.00

Table 14: Particle size distribution from sieving of G406.

Sieving of 100g G406		
Particle fraction [µm]	**Mass [g]**	**Distribution (99.58g)**
>106	17.38	0.17
75-106	16.24	0.16
63-75	8.02	0.08
36-63	18.70	0.19
<36	39.24	0.39
Sum	99.58	1.00

Table 15: Particle size distribution from sieving of G407.

Sieving of 100g G407		
Particle fraction [µm]	**Mass [g]**	**Distribution (99.54g)**
>106	15.50	0.16
75-106	14.75	0.15
63-75	7.16	0.07
36-63	17.47	0.18
<36	44.66	0.45
Sum	99.54	1.00

Table 16: Particle size distribution from sieving of G408.

Sieving of 100g G408		
Particle fraction [µm]	**Mass [g]**	**Distribution (99.74g)**
>106	16.65	0.17
75-106	16.29	0.16
63-75	8.13	0.08
36-63	17.16	0.17
<36	41.51	0.42
Sum	99.74	1.00

C. LOM

C.1. Casting and polishing recipe

Recipe for Bakelite die pressing:

- 2ml power + 5ml "*UT FINA MET*"-Bakelite powder mixed well and poured into the press. (1ml powder can also be used but then the "UT FINA MET" should also be halved.)
- 7.5ml "Bakelite Phenocure" - powder poured evenly into the press over the mix. (More if less mix)
- Compacting under heat for 9:30 min.

Recipe for polishing :

The step names in the polishing are designations for different roughness used with the Struers Abrapol-10 setup.

Table 17: Polishing recipe

Step	Time
1. "Piano"	1 min
2. "Allegro"	6 min
3. "MD/DP – Mol	5 min
4. "NAP"	30 sec

C.2. LOM images

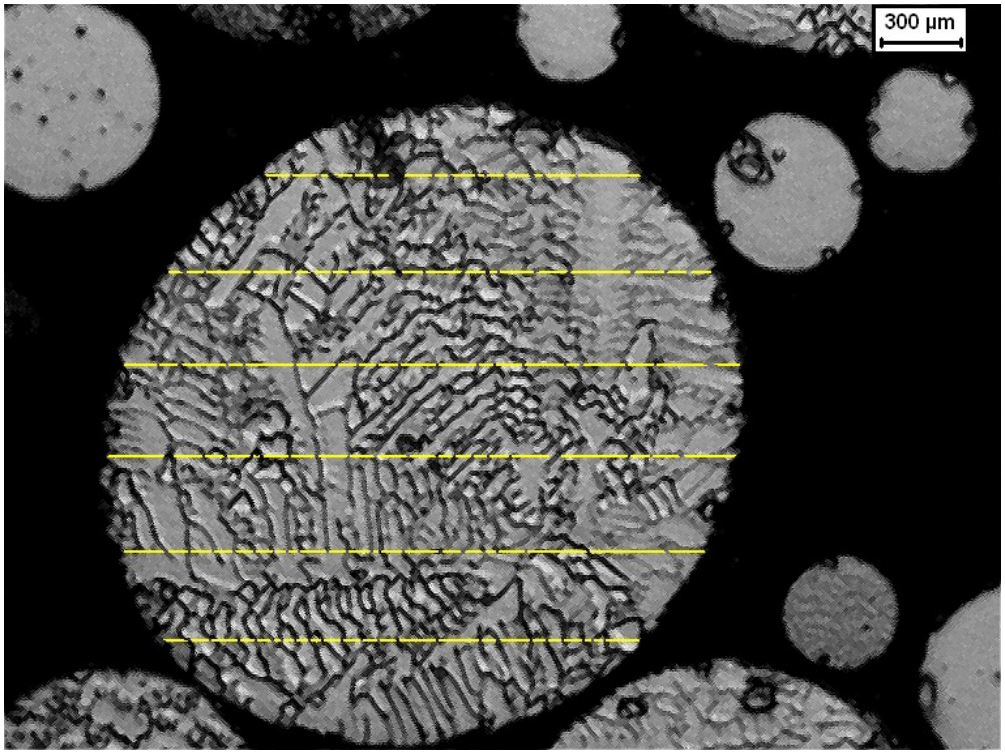

Figure 36: Example of grain counting by use of LOM macro.

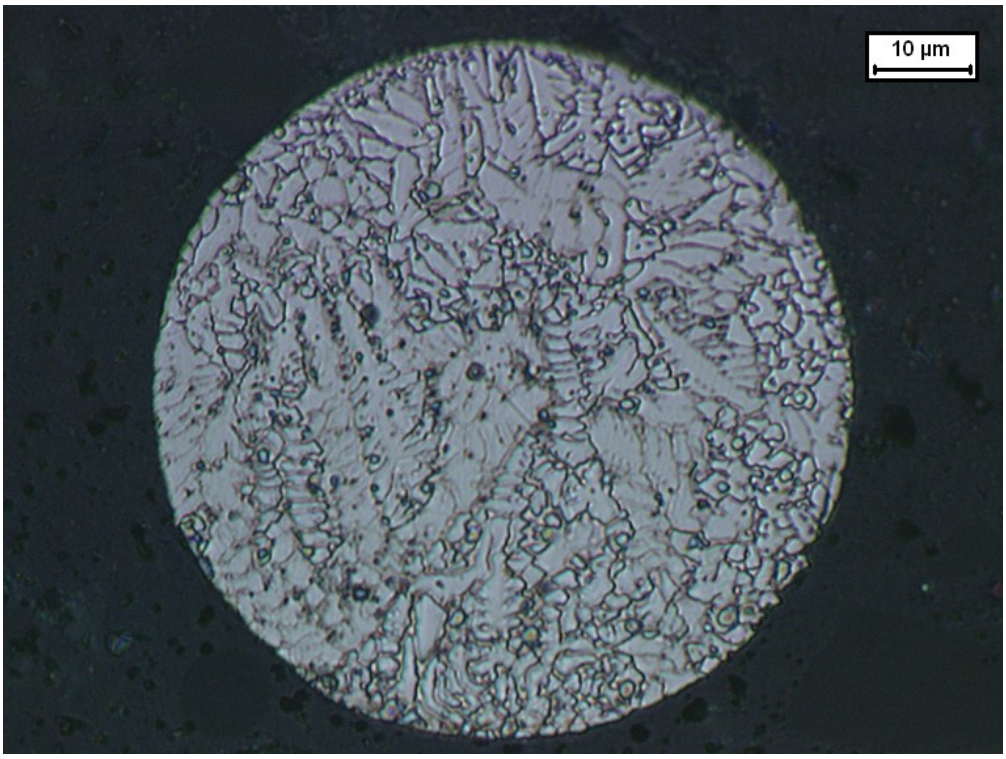

Figure 37: Example of typical microstructure of the G336 particles.

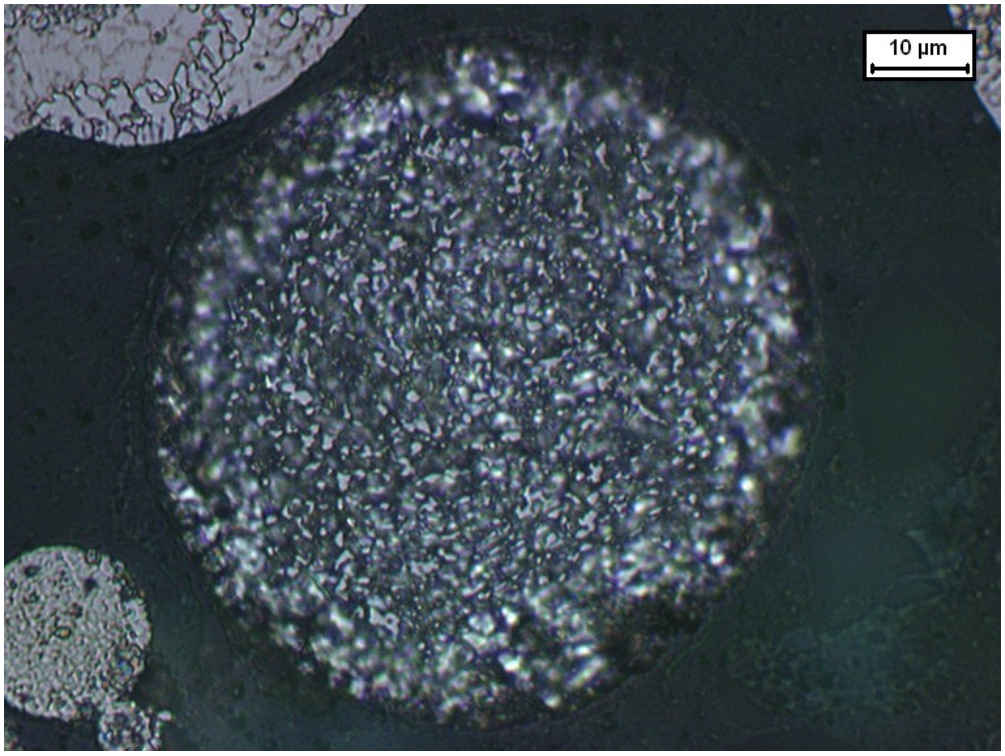

Figure 38: Example of a particle with very fine, sub-micron microstructure in G336.

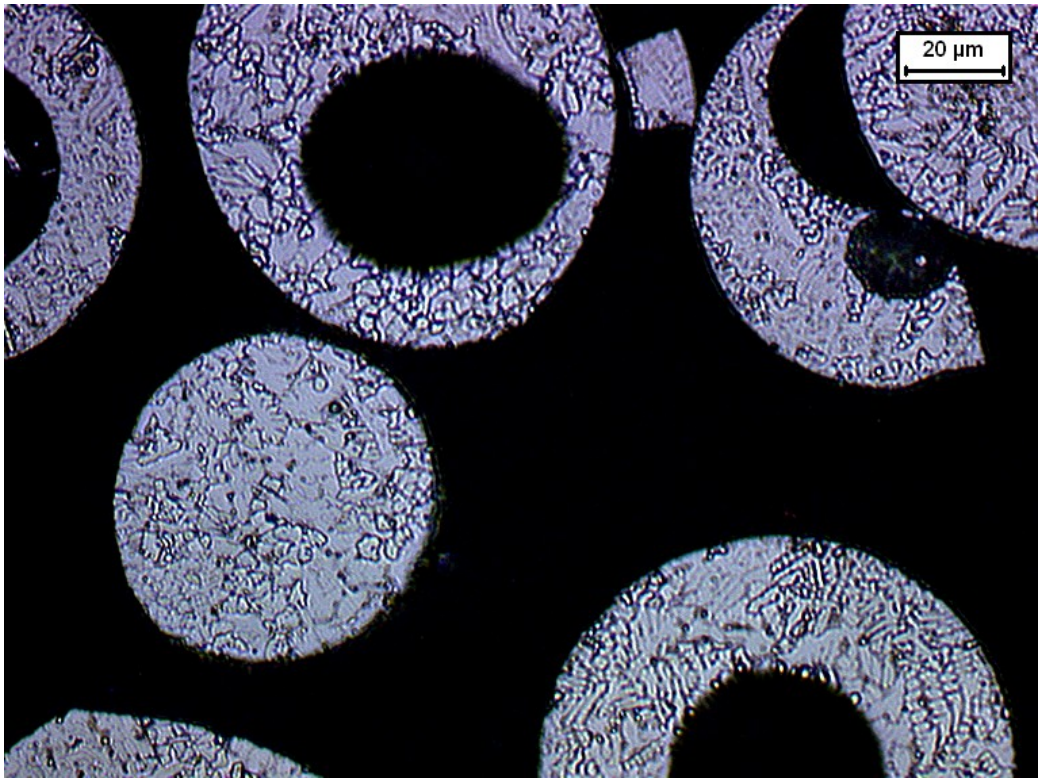

Figure 39: Example of typical bubbled particles in the G336 material, 75-106µm fraction.

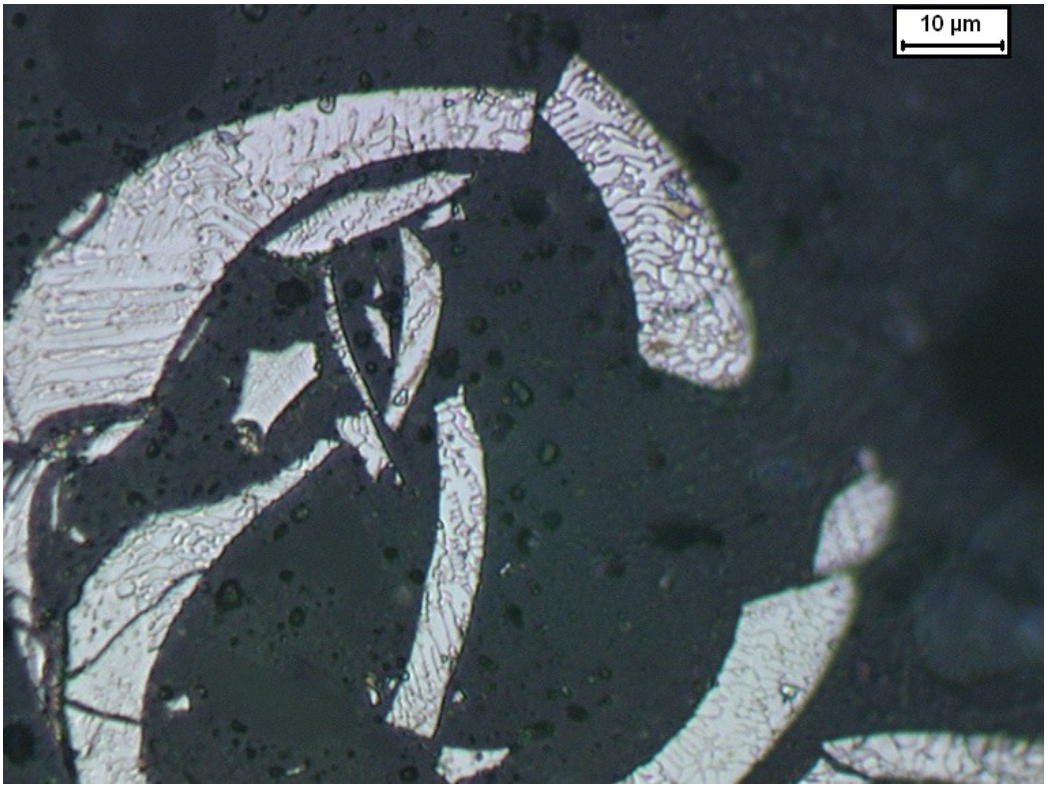

Figure 40: Example of fractured particle in the G336 material, 75-106µm.

C.3. Tables of LOM data

Table 18: Results from manual particle counting in LOM.

Non heat treated

Particle description	36	63	75	150
Solid particles	256	81	48	81
Super fine microstructure	38	17	7	9
Particles w. bubbles	21	52	23	38
Fragmented particles	13	26	29	52
Total	328	176	107	180

Particle description	36	63	75	150
Solid particles	0.78	0.46	0.45	0.45
Super fine microstructure	0.12	0.10	0.07	0.05
Particles w. bubbles	0.06	0.30	0.21	0.21
Fragmented particles	0.04	0.15	0.27	0.29
Total	1	1	1	1

Table 19: Results from manual particle counting in LOM.

8h @ 700OC

Particle description	36	63	75	106
Whole particles	140	94	103	93
Super fine microstructure	81	23	20	18
Particles w. bubbles	26	43	71	76
Fragmented particles	5	12	37	41
Total	252	172	231	228

Particle description	36	63	75	106
Whole particles	0.56	0.55	0.45	0.41
Super fine microstructure	0.32	0.13	0.09	0.08
Particles w. bubbles	0.10	0.25	0.31	0.33
Fragmented particles	0.02	0.07	0.16	0.18
Total	1	1	1	1

Table 20: Results from manual particle counting in LOM.

16h @ 700OC

Particle description	36	63	75	106
Whole particles	53	59	55	48
Super fine microstructure	95	21	13	16
Particles w. bubbles	20	51	59	59
Fragmented particles	4	17	46	66
Total	172	148	173	189

Particle description	36	63	75	106
Whole particles	0.31	0.40	0.32	0.25
Super fine microstructure	0.55	0.14	0.08	0.08
Particles w. bubbles	0.12	0.34	0.34	0.31
Fragmented particles	0.02	0.11	0.27	0.35
Total	1	1	1	1

Table 21: Calculation of number of grains per particle from the LOM analysis.

	Non HT				8h				16h			
Particle	36	63	75	106	36	63	75	106	36	63	75	106
Grain	1.36	1.73	2.22	3.36	1.48	1.95	1.97	3.75	1.5	1.93	2.35	2.22
GPP	18548	48293	38559	31398	14392	33722	55180	22585	13824	34782	32507	108858

Table 22: Grain counting results from the LOM macro of non-heat treated G336, <35µm.

Particle	# grains in particle	Acc. # grains	Av. intercept length [µm]
1	113	113	1.3
2	98	211	1.3
3	119	330	1.3
4	96	426	1.3
5	70	496	1.3
6	52	548	1.3
7	67	615	1.4
8	85	700	1.4
9	85	785	1.4
10	69	854	1.4
11	39	893	1.4
12	85	978	1.4
13	75	1053	1.4
14	65	1118	1.4
15	114	1232	1.4
Average	82.13		1.36

Table 23: Grain counting results from the LOM macro of non-heat treated G336, 36-63µm.

Particle	# grains in particle	Acc. # grains	Av. intercept length [µm]
1	96	96	1.7
2	107	203	1.7
3	117	320	1.7
4	91	411	1.6
5	94	505	1.7
7	81	586	1.7
8	51	637	1.7
9	95	732	1.7
10	83	815	1.7
11	81	896	1.8
12	91	987	1.8
13	86	1073	1.8
14	57	1130	1.8
15	88	1218	1.8
16	77	1295	1.8
Average	86		1.7

Table 24: Grain counting results from the LOM macro of non-heat treated G336, 63-75µm.

Particle	# grains in particle	Acc. # grains	Av. intercept length [µm]
1	122	122	2.1
2	114	236	2.1
3	141	377	2.1
4	126	503	2.2
5	111	614	2.2
6	103	717	2.3
7	100	817	2.3
8	117	934	2.3
9	78	1012	2.3
10	125	1137	2.3
11	79	1216	2.3
12	75	1291	2.3
13	77	1368	2.2
14	143	1511	2.2
15	119	1630	2.2
Average	109		2.2

Table 25: Grain counting results from the LOM macro of non-heat treated G336, 75-106µm.

Particle	# grains in particle	Acc. # grains	Av. intercept length [µm]
1	94	94	3.6
2	43	137	3.3
3	58	195	3.3
4	53	248	3.3
5	69	317	3.4
6	56	373	3.4
7	106	479	3.5
8	66	545	3.4
9	38	583	3.4
10	33	616	3.4
11	106	722	3.3
12	68	790	3.3
13	43	833	3.3
14	67	900	3.3
15	118	1018	3.3
Average	68		3.4

Table 26: Grain counting results from the LOM macro of 8h heat treated G336, <36µm.

Particle	# grains in particle	Acc. # grains	Av. intercept length [µm]
1	91	91	1.5
2	68	159	1.4
3	48	207	1.4
4	22	229	1.4
5	76	305	1.5
6	53	358	1.5
7	58	416	1.5
8	58	474	1.5
9	34	508	1.5
10	47	555	1.5
11	71	626	1.5
12	36	662	1.5
13	31	693	1.5
14	46	739	1.5
15	59	798	1.5
Average	53		1.48

Table 27: Grain counting results from the LOM macro of 8h heat treated G336, 36-63µm.

Particle	# grains in particle	Acc. # grains	Av. intercept length [µm]
1	63	63	1.7
2	43	106	1.6
3	35	141	1.7
4	58	199	1.9
5	69	268	2.1
6	133	401	2.0
7	62	463	1.9
8	66	529	2.0
9	90	619	2.0
10	93	712	2.0
11	66	778	2.0
12	99	877	2.0
13	81	958	2.1
14	61	1019	2.1
15	82	1101	2.1
Average	73		1.95

Table 28: Grain counting results from the LOM macro of 8h heat treated G336, 63-75µm.

Particle	# grains in particle	Acc. # grains	Av. intercept length [µm]
1	122	122	1.7
2	124	246	1.8
3	135	381	1.9
4	122	503	2.0
5	115	618	2.0
6	112	730	2.0
7	131	861	2.0
8	126	987	2.0
9	108	1095	2.0
10	95	1190	2.0
11	113	1303	2.0
12	99	1402	2.0
13	105	1507	2.0
14	120	1627	2.0
15	131	1758	2.1
Average	117		1.97

Table 29: Grain counting results from the LOM macro of 8h heat treated G336, 75-106µm.

Particle	# grains in particle	Acc. # grains	Av. intercept length [µm]
1	91	91	3.6
2	74	165	3.5
3	105	270	3.5
4	55	325	3.6
5	63	388	3.6
6	85	473	3.7
7	60	533	3.7
8	106	639	3.8
9	88	727	3.8
10	68	795	3.8
11	96	891	3.9
12	131	1022	3.9
13	101	1123	3.9
14	75	1198	4
15	123	1321	4
Average	88		3.75

Table 30: Grain counting results from the LOM macro of 16h heat treated G336, <36µm.

Particle	# grains in particle	Acc. # grains	Av. intercept length [µm]
1	68	68	1.4
2	55	123	1.4
3	60	183	1.4
4	73	256	1.6
5	47	303	1.6
6	39	342	1.5
7	50	392	1.5
8	29	421	1.5
9	42	463	1.5
10	80	543	1.5
11	38	581	1.5
12	31	612	1.5
13	45	657	1.6
14	61	718	1.5
15	52	770	1.5
Average	51		1.50

Table 31: Grain counting results from the LOM macro of 16h heat treated G336, 36-63µm.

Particle	# grains in particle	Acc. # grains	Av. intercept length [µm]
1	75	75	1.5
2	79	154	1.7
3	117	271	1.9
4	127	398	1.9
5	97	495	2.0
6	92	587	2.0
7	101	688	2.0
8	78	766	2.0
9	63	829	2.0
10	82	911	1.9
11	105	1016	2.0
12	100	1116	2.0
13	79	1195	2.0
14	89	1284	2.0
15	116	1400	2.0
Average	93		1.93

Table 32: Grain counting results from the LOM macro of 16h heat treated G336, 63-75µm.

Particle	# grains in particle	Acc. # grains	Av. intercept length [µm]
1	136	136	2.0
2	127	263	2.4
3	146	409	2.3
4	129	538	2.3
5	135	673	2.3
6	127	800	2.4
7	117	917	2.4
8	93	1010	2.4
9	128	1138	2.4
10	120	1258	2.4
11	139	1397	2.3
12	128	1525	2.3
13	133	1658	2.5
14	143	1801	2.5
15	156	1957	2.4
Average	130		2.35

Table 33: Grain counting results from the LOM macro of 16h heat treated G336, 75-106µm.

Particle	# grains in particle	Acc. # grains	Av. intercept length [µm]
1	157	157	2.0
2	88	245	2.1
3	145	390	2.2
4	147	537	2.2
5	115	652	2.2
6	113	765	2.3
7	135	900	2.3
8	160	1060	2.2
9	97	1157	2.2
10	120	1277	2.2
11	71	1348	2.3
12	105	1453	2.3
13	127	1580	2.3
14	138	1718	2.3
15	130	1848	2.3
Average	123		2.23

D. STA graphs

D.1. Non-milled

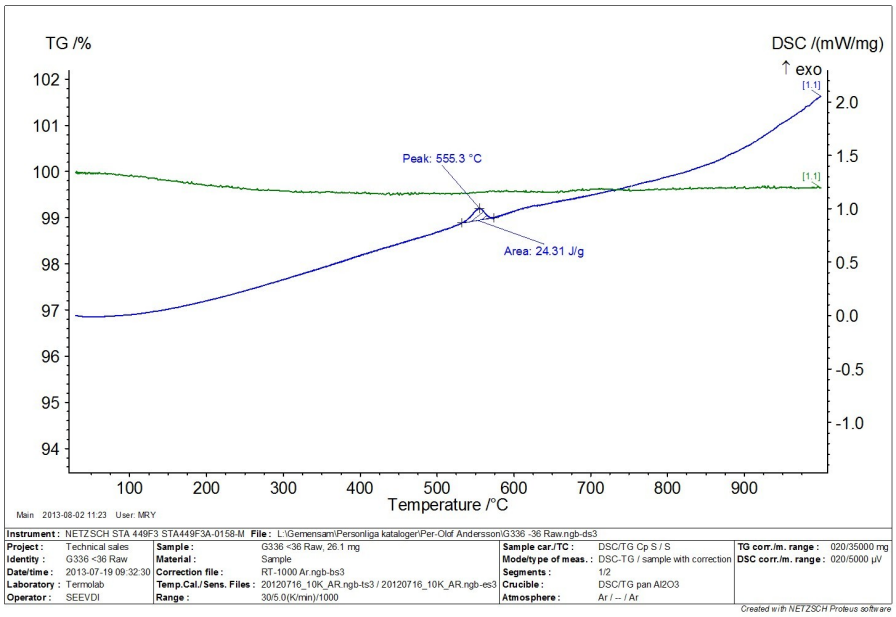

Figure 41: STA of non-milled G336 at <36µm showing the exothermic peak.

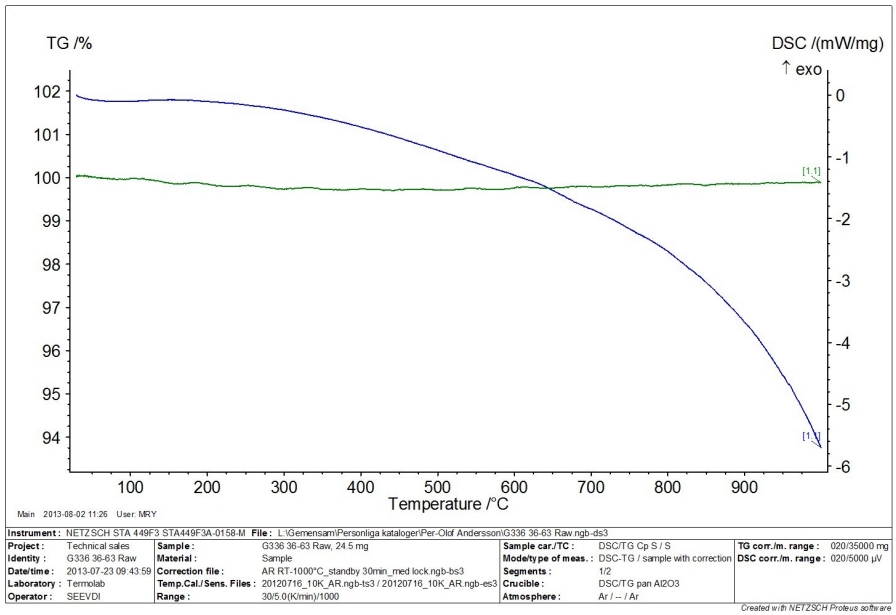

Figure 42: STA of non-milled G336 at 36-63µm.

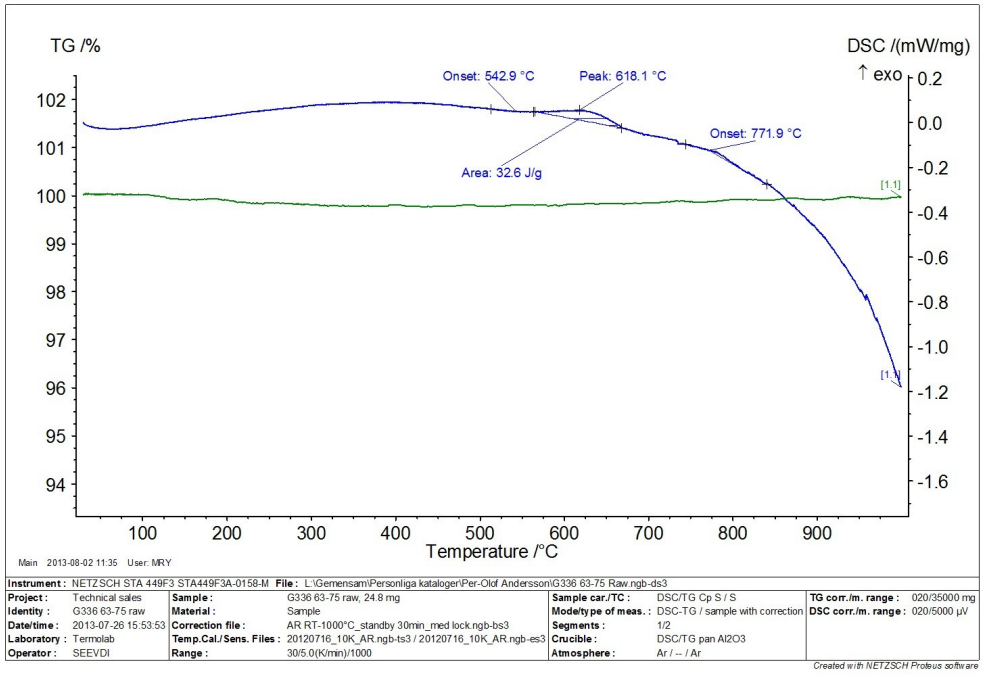

Figure 43: STA of non-milled G336 at 63-75µm showing a similar, more smeared exothermic peak.

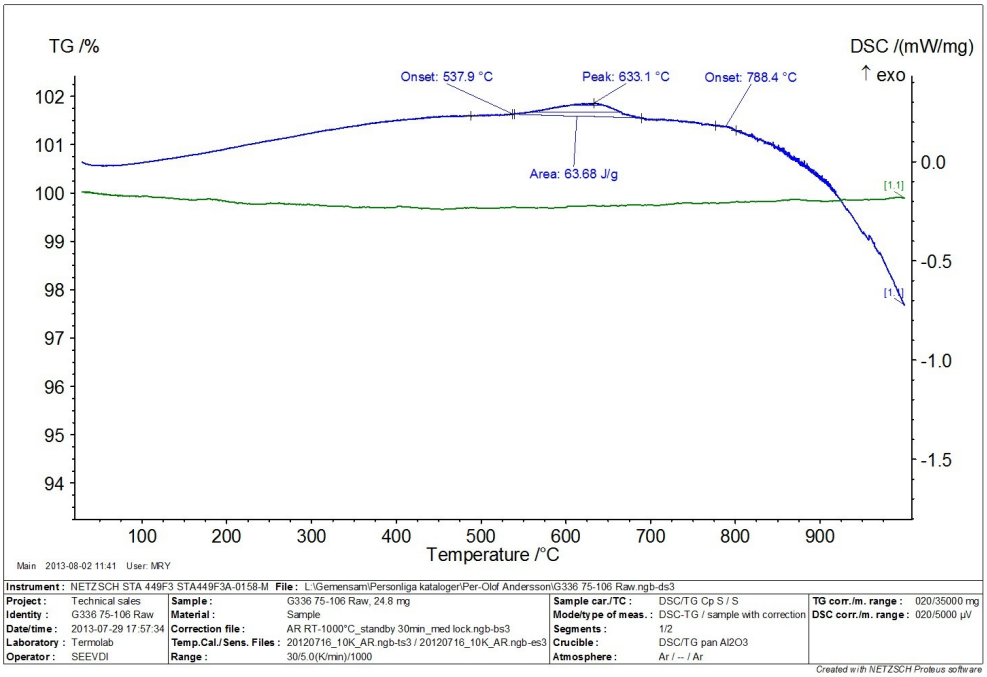

Figure 44: STA of non-milled G336 at 75-106µm showing a smaller, more smeared exothermic peak.

D.2. Milled

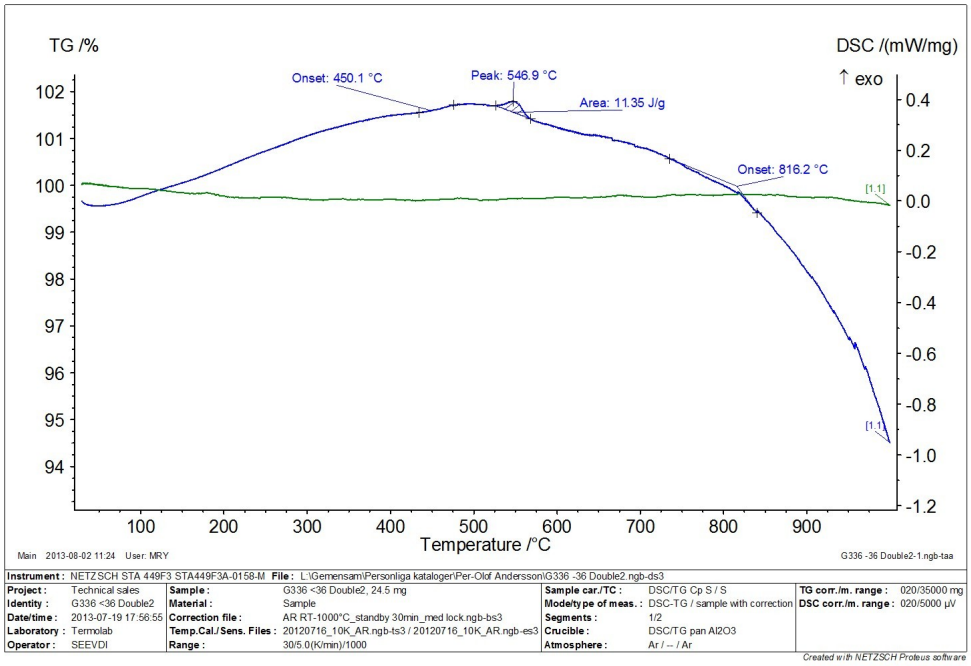

Figure 45: STA of milled G336 at <36µm showing the exothermic peak.

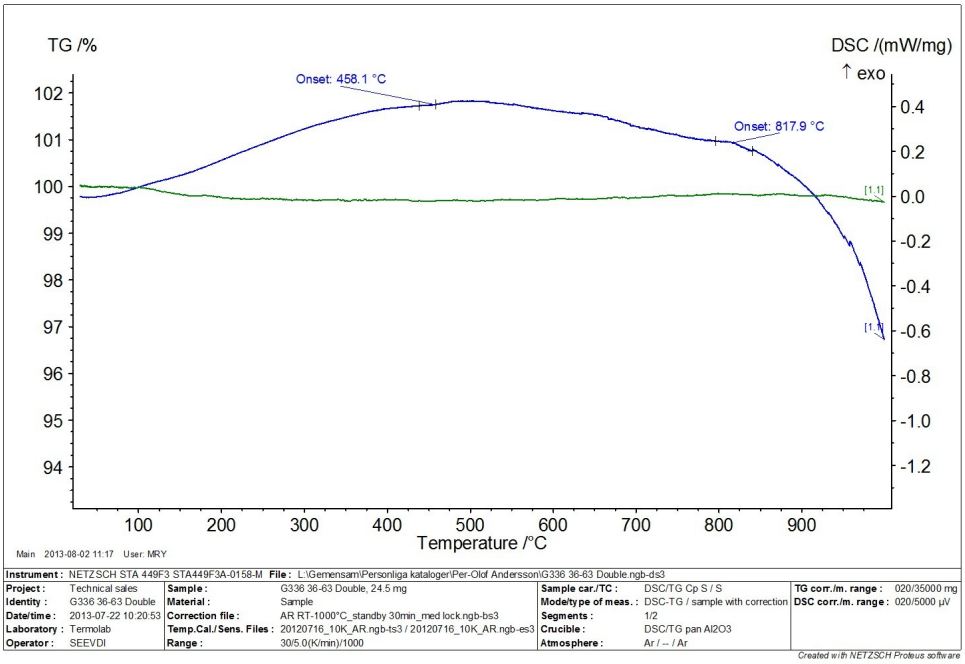

Figure 46: STA of milled G336 at 36-63µm hinting at a small exothermal bulge at 850^{O}C.

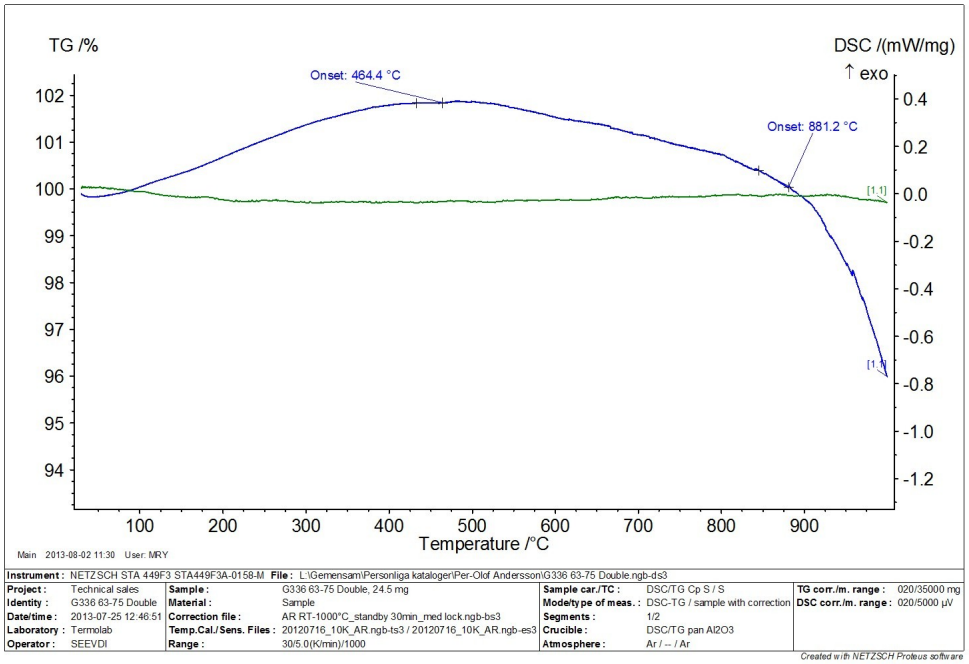

Figure 47: STA of milled G336 at 63-75µm.

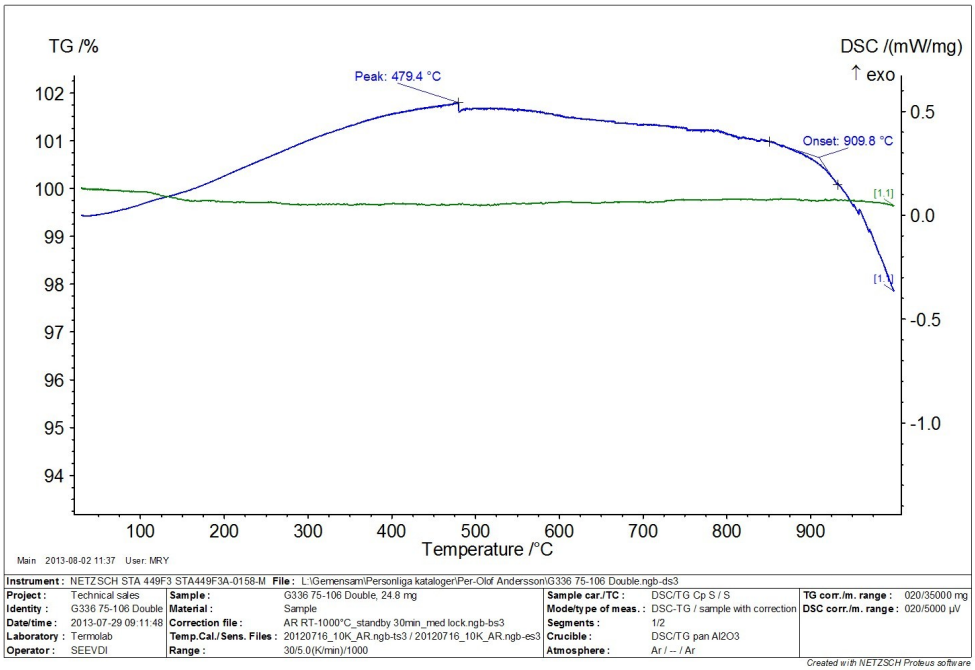

Figure 48: STA of milled G336 at 75-106µm. The small notch around 450^{O}C is assumed to be a measurement error.

E. SEM

E.1. Casting and polishing recipe

This recipe was used in the SEM imaging of the double milled G336 powder. It has conductive graphite in the powder mix as well as iron powder in the bulk material so as to provide the sample with a greater conductivity and thereby reducing the charging effect.

Recipe for Bakelite die pressing:

- 2ml power, 1ml graphite and 5ml EPOMET Bakelite powder is mixed well and poured into the press.
- 7.5ml “Bakelite Phenocure” and 2 ml pure iron powder poured evenly into the press over the mix. (More if less mix from step one)
- Compacting under heat for 9:30 min.

Recipe for polishing :

The step names in the polishing are designations for different roughness used with the Struers Rotopol-22 setup with Struers Rotoforce-4.

Table 34: Polishing recipe for viewing double milled powders in SEM.

Step	Time	Force [N]	Speed [rpm]
#320	1 min	15	150
9µ	3 min	15	150
3µ “MOL”	6 min	15	150
3µ “MOL”	6 min	10	150
1µ “NAP”	30 sec	10	150

E.2. SEM images

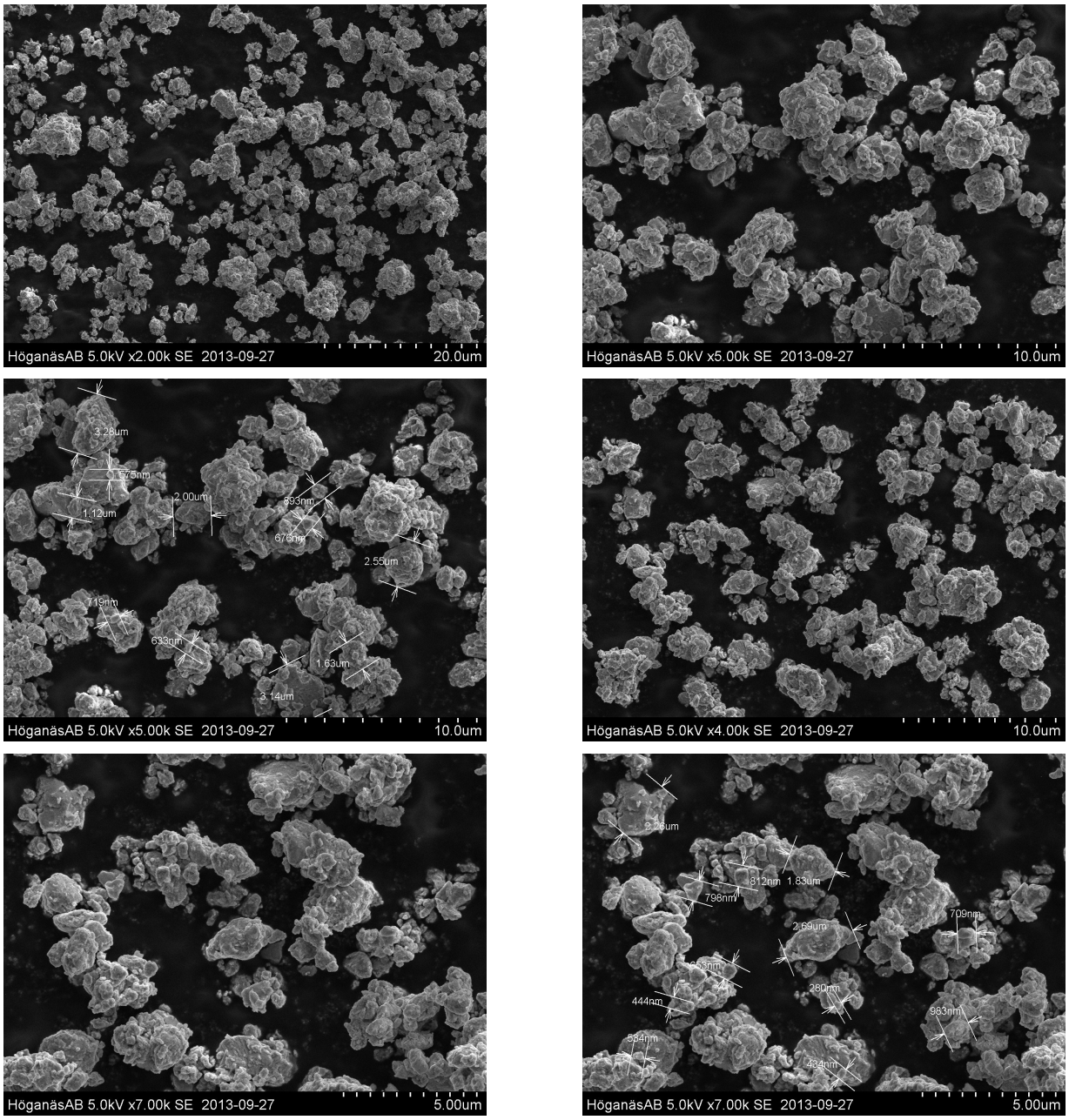

Figure 49: Milled (5/20) G336 powder of the 63-75µm fraction before annealing.

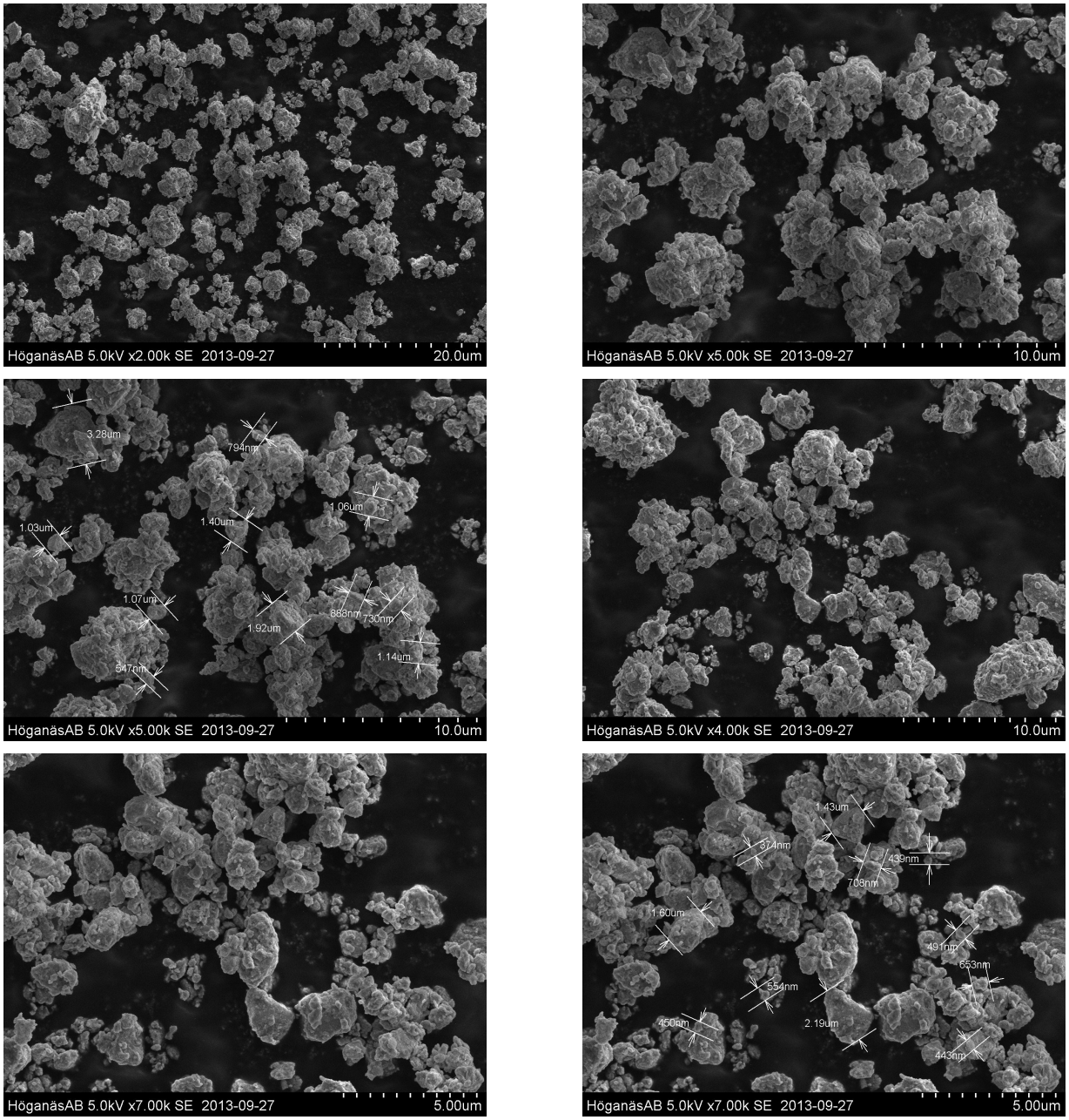

Figure 50: Milled (5/20) G336 powder of the 36-63µm fraction before annealing.

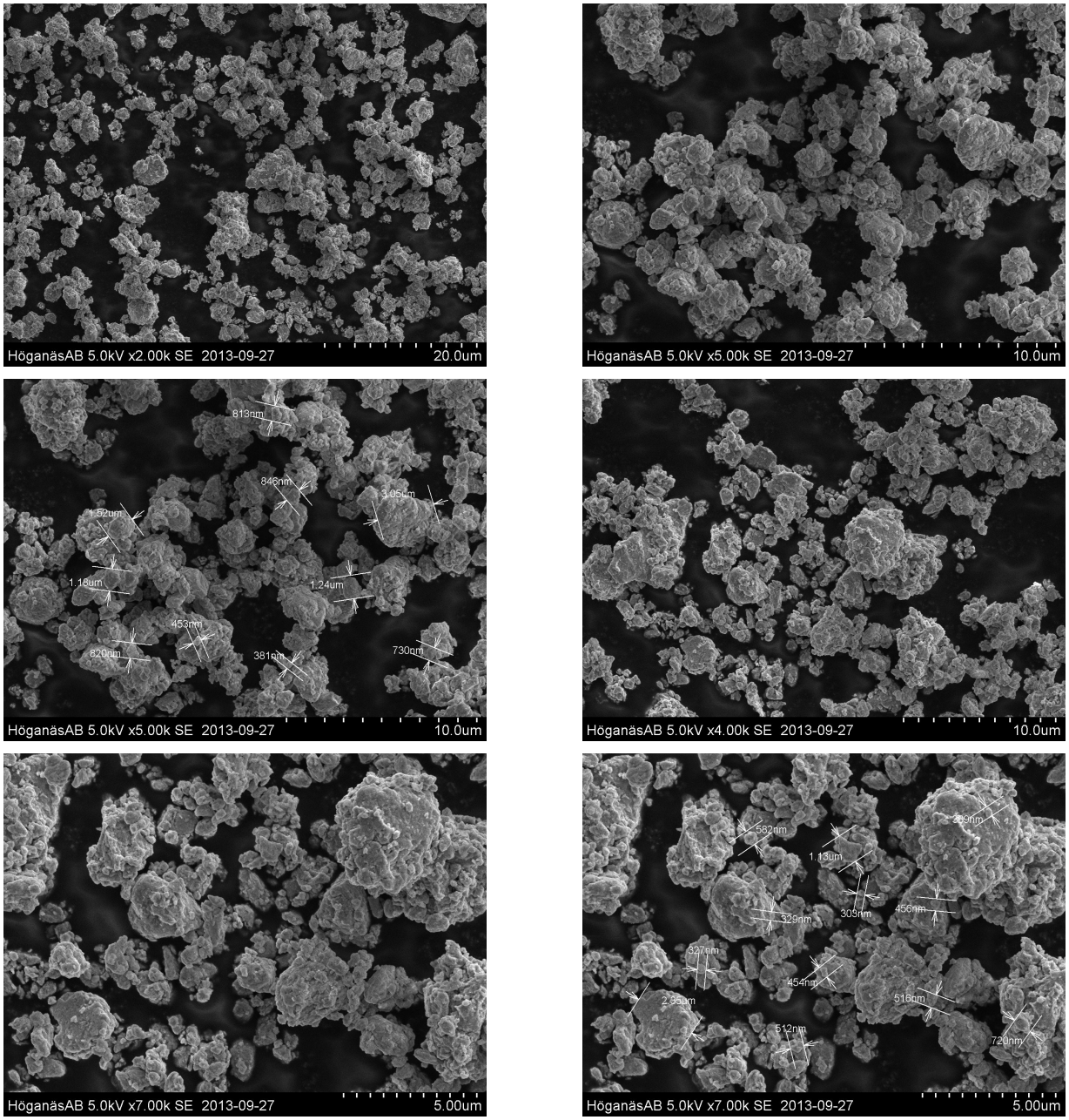

Figure 51: Milled (5/20) G336 powder of the -36µm fraction before annealing.

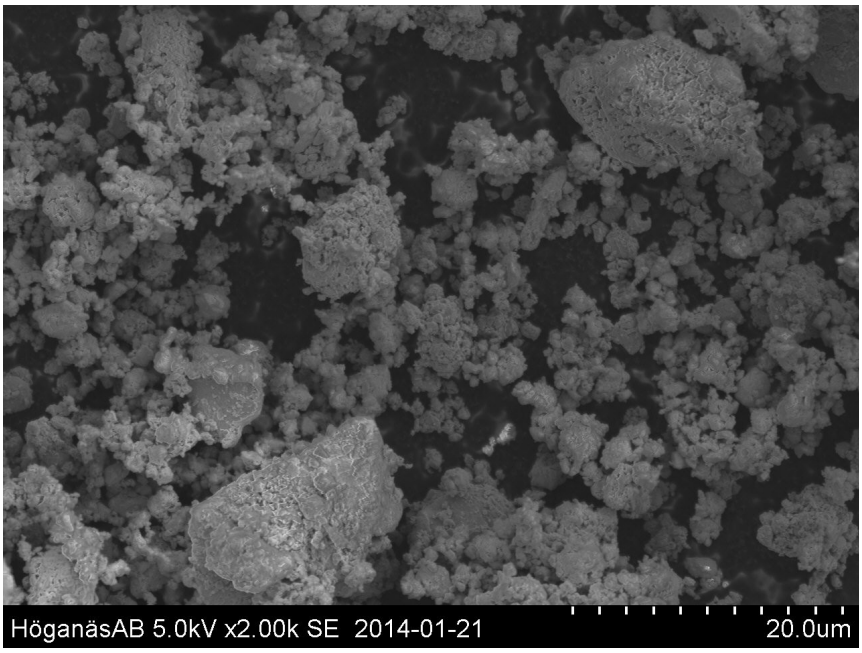

Figure 52: SEM image of milled (5/20 + 5/5) G336 powder showing the particle surface and shape.

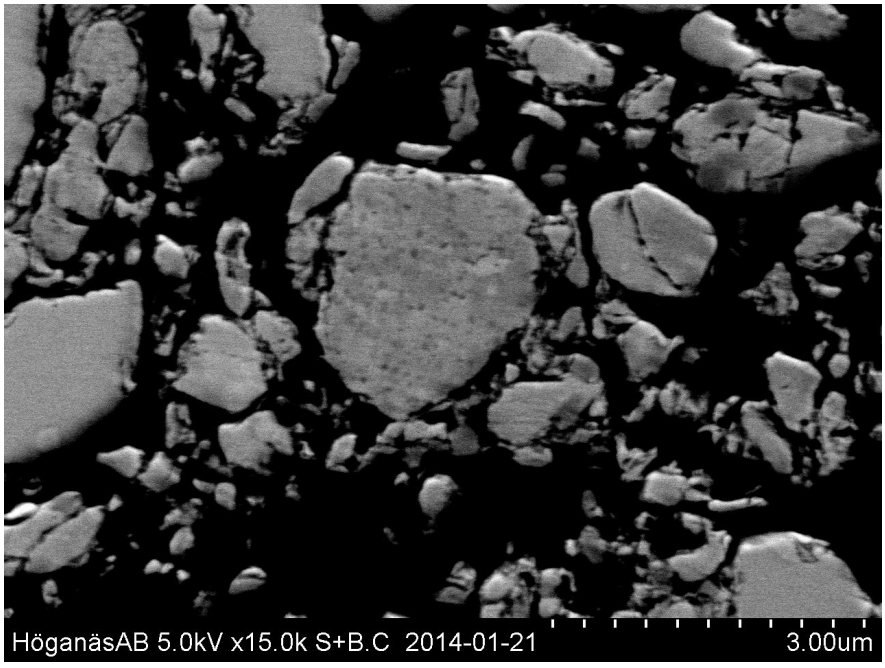

Figure 53: SEM image of milled (5/20 + 5/5) G336 powder showing a cross section of the particles.

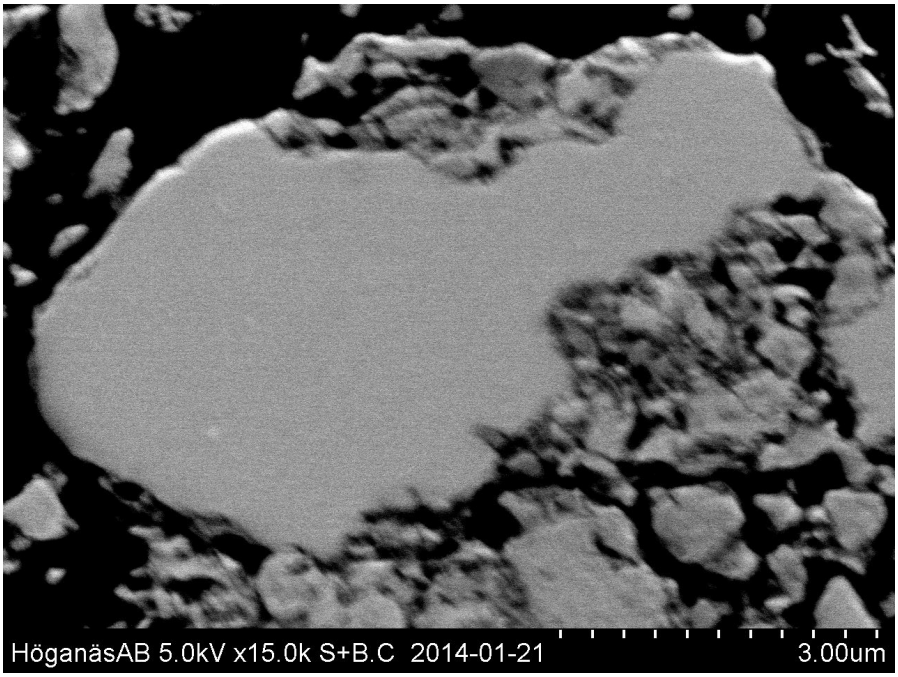

Figure 54: SEM image of milled (5/20 + 5/5) G336 powder showing a cross section of a seemingly single crystalline particle.

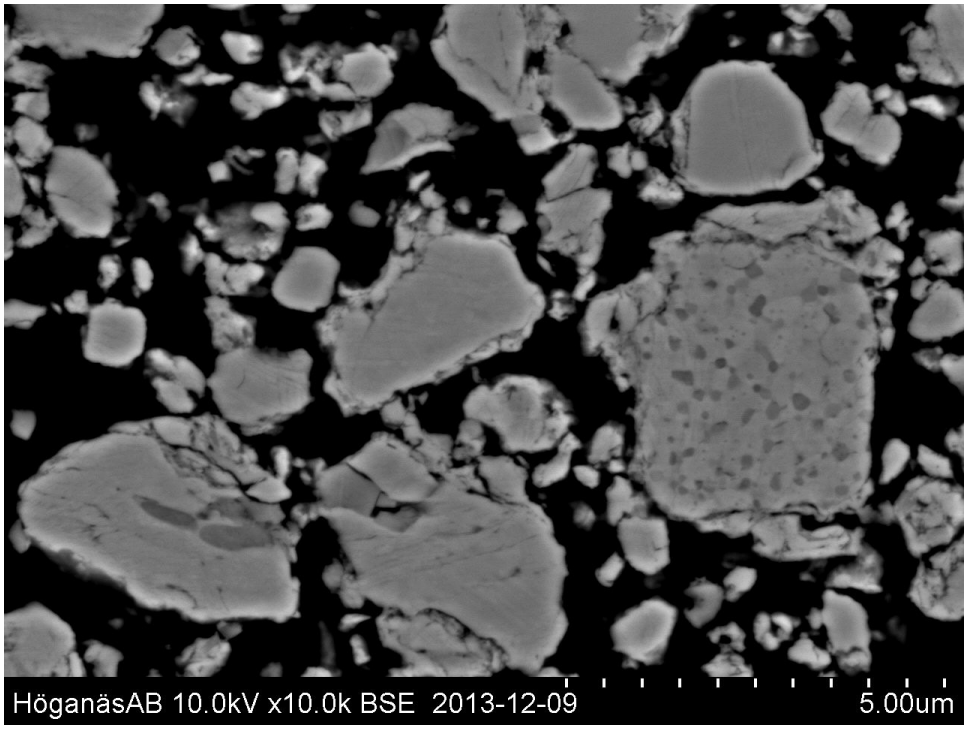

Figure 55: SEM image of milled (5/20) G336 powder showing a cross section of particles with clear inclusions of a dark phase.

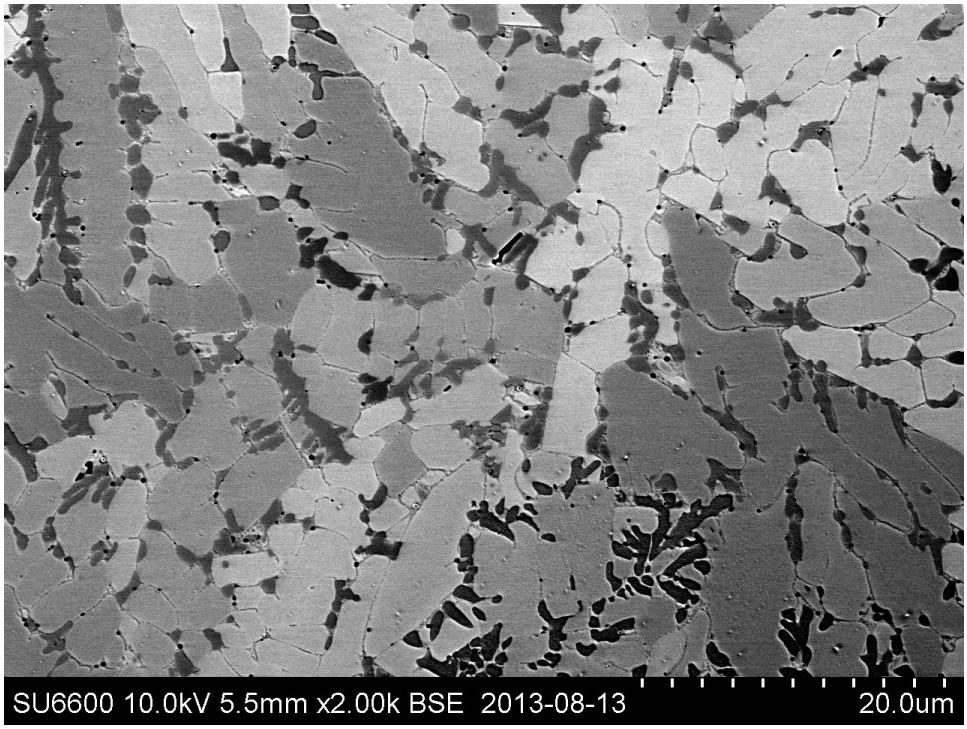

Figure 56: SEM image of the G336 material, 75-106µm fraction, showing boron rich dark gray inclusions.

F. XRD

F.1. Stress and strain results

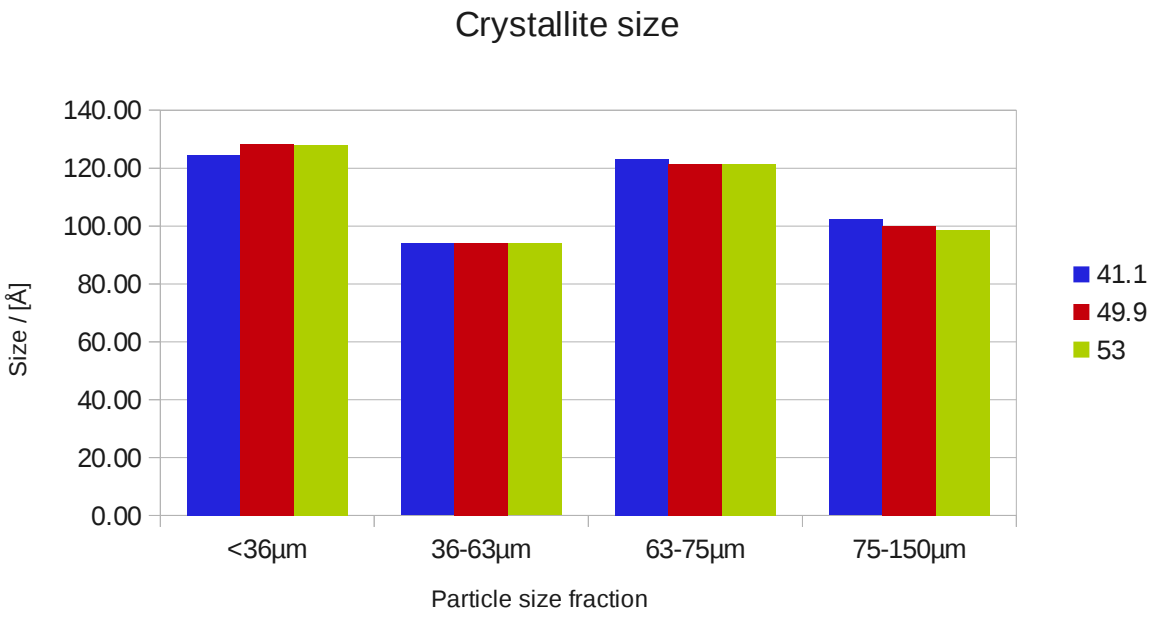

Figure 57: Crystallite sizes for the four powder fractions of G336 after 5/20-milling.

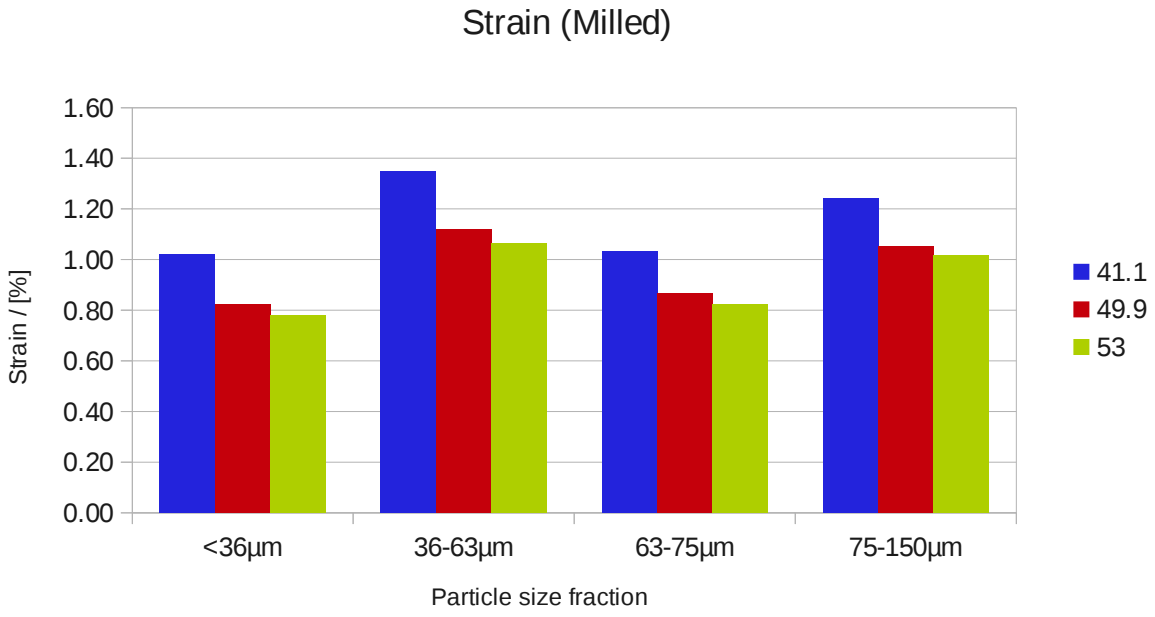

Figure 58: Strain for the four powder fractions of G336 after 5/20-milling.

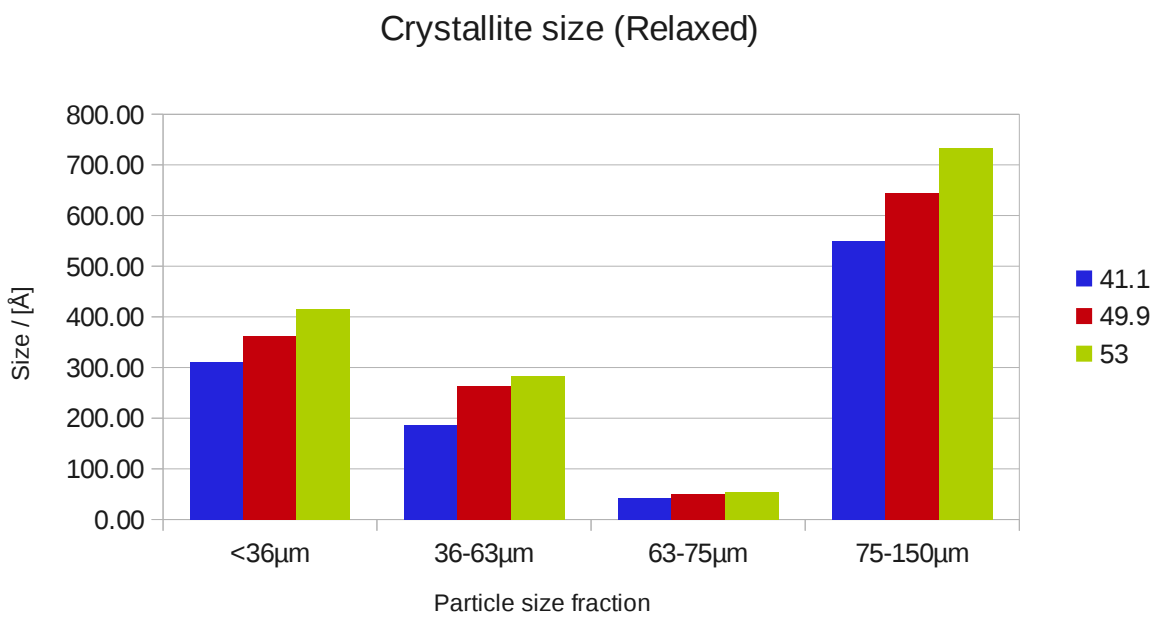

Figure 59: Crystallite size for the four powder fractions of G336 after relaxation at 700^{O}C for 1h.

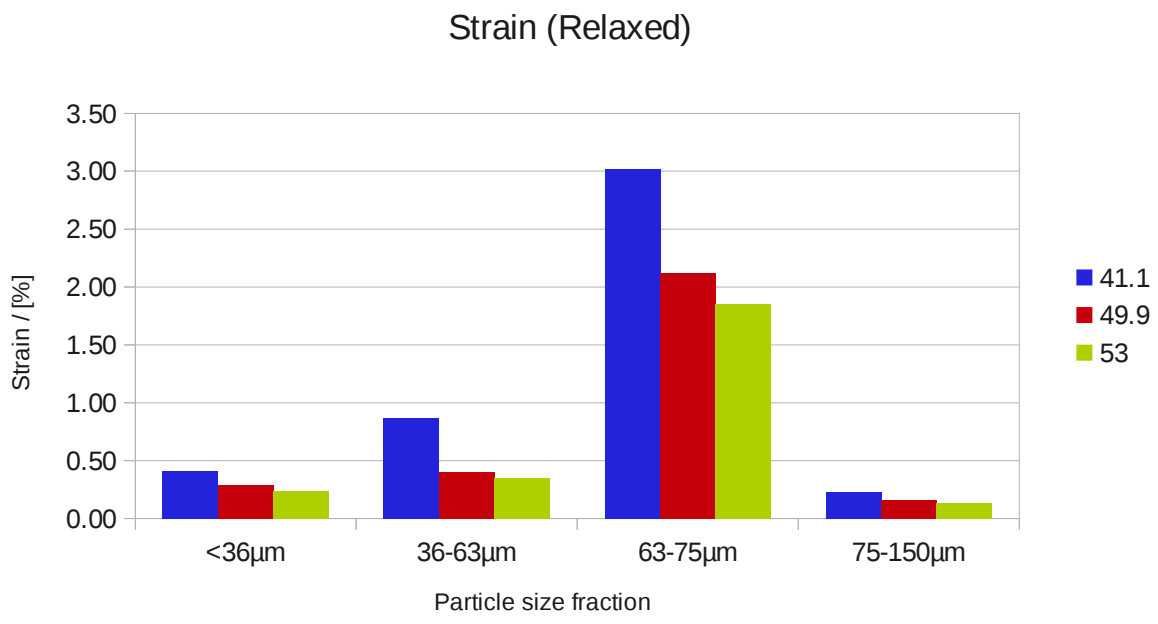

Figure 60: Strain for the four powder fractions of G336 after relaxation at 700^{O}C for 1h.

F.2. Fitted graphs

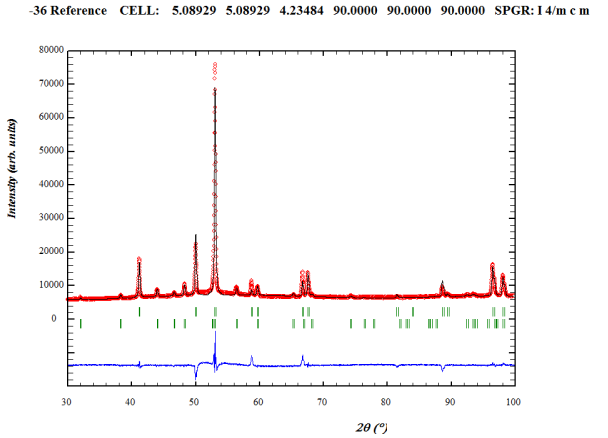

Figure 61: -36µm reference (no H_2 heat treatment) sample.

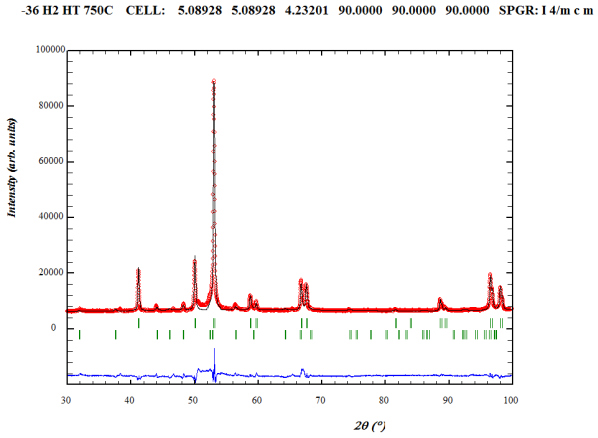

Figure 62: -36µm sample, H2 heat treated at 750^{O}C.

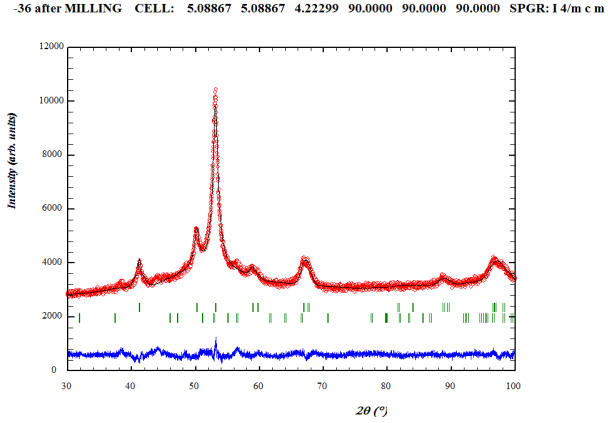

Figure 63: Milled -36µm reference sample.

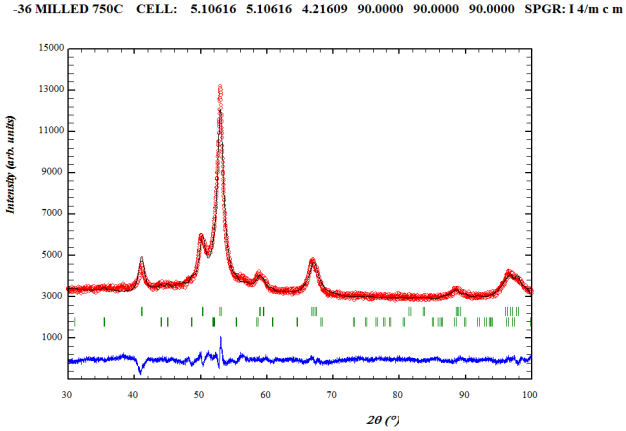

Figure 64: Milled -36µm sample, H_2 heat treated at 750^{O}C.

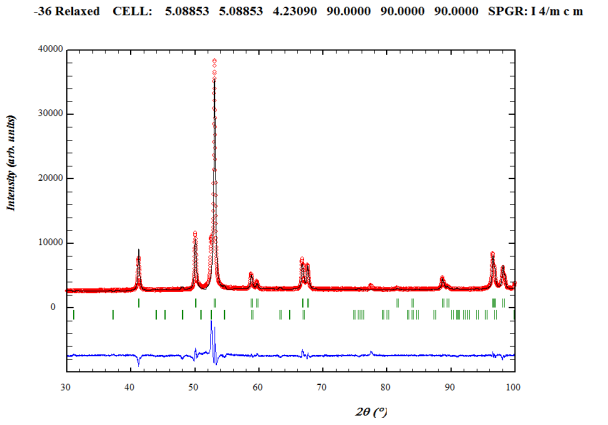

Figure 65: Relaxed -36µm reference sample.

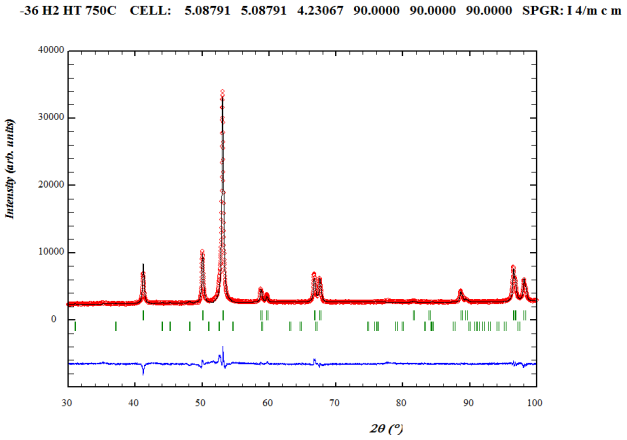

Figure 66: Relaxed -36µm sample, H_2 heat treated at 750^{O}C.

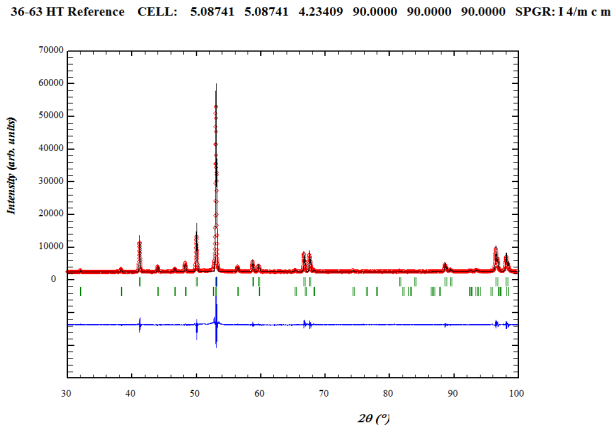

Figure 67: 36-63µm reference (no H2 heat treatment) sample.

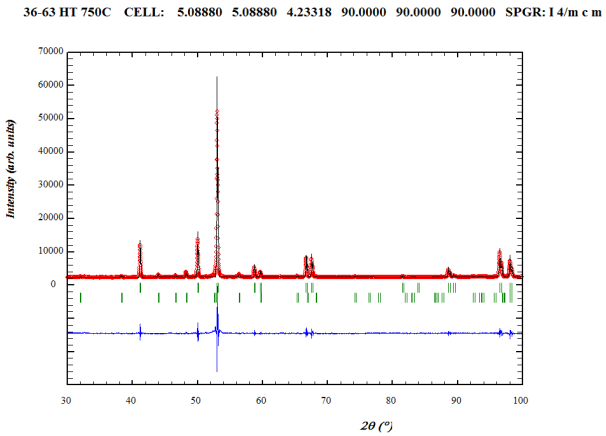

Figure 68: 36-63µm sample, H2 heat treated at 750^{O}C.

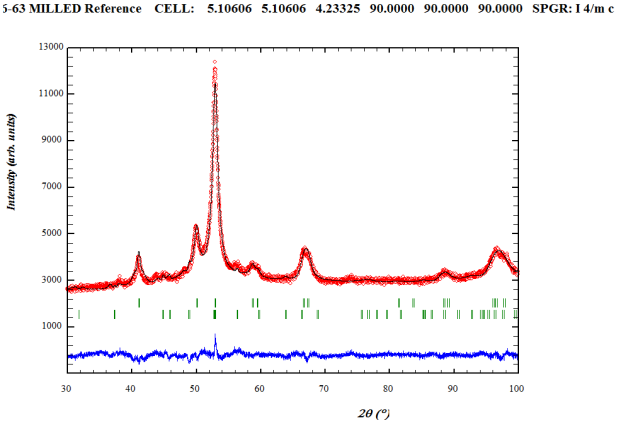

Figure 69: Milled 36-63µm reference sample.

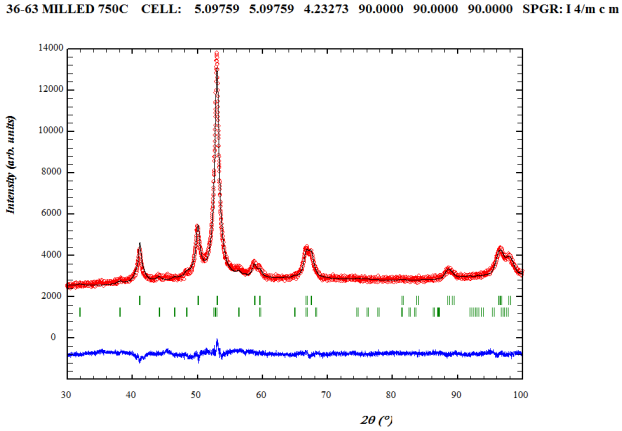

Figure 70: Milled 36-63µm sample, H2 heat treated at 750OC.

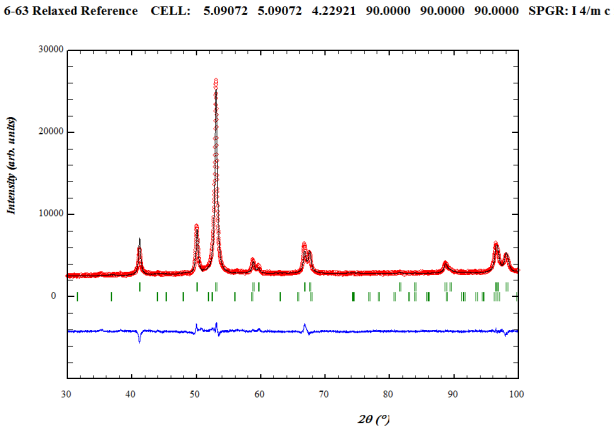

Figure 71: Relaxed 36-63µm reference sample.

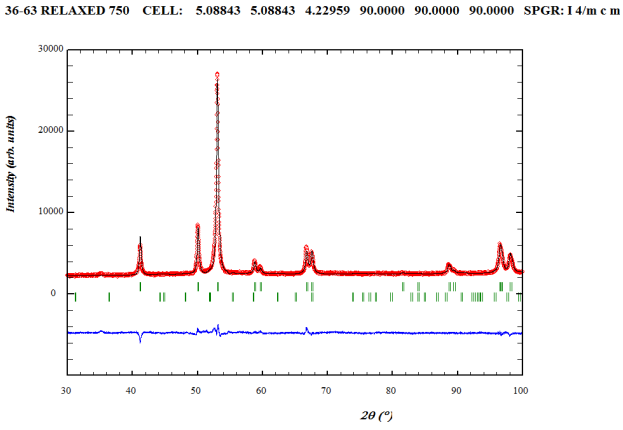

Figure 72: Relaxed 36-63µm sample, H_2 heat treated at 750^{O}C.

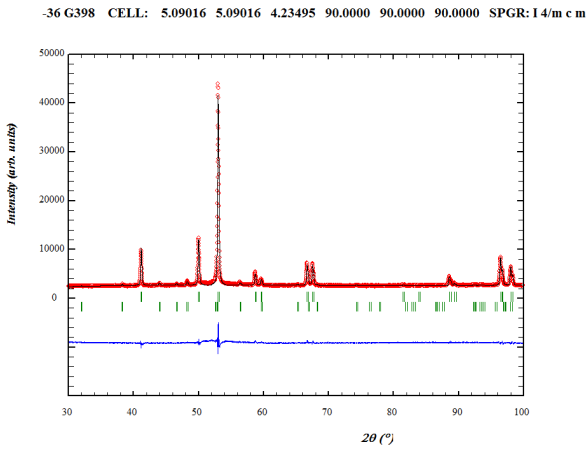

Figure 73: -36µm sample of G398.

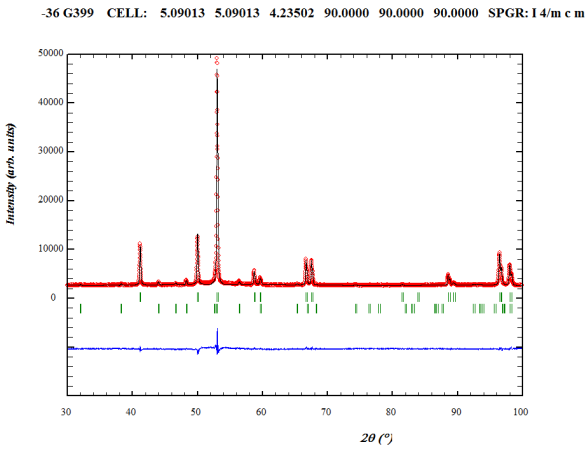

Figure 74: -36µm sample of G399.

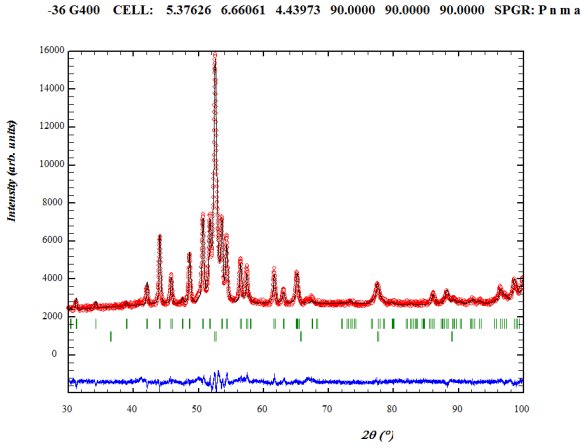

Figure 75: -36µm sample of G400.

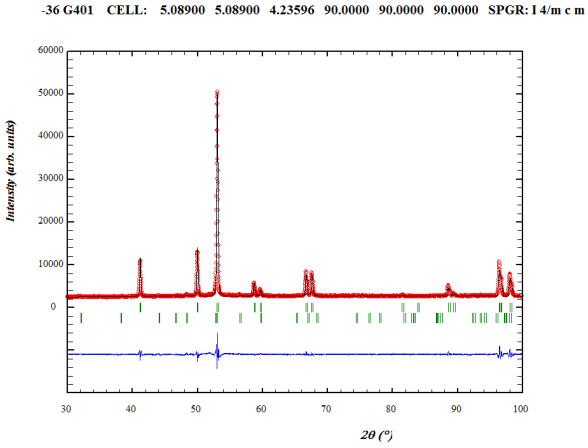

Figure 76: -36µm sample of G401.

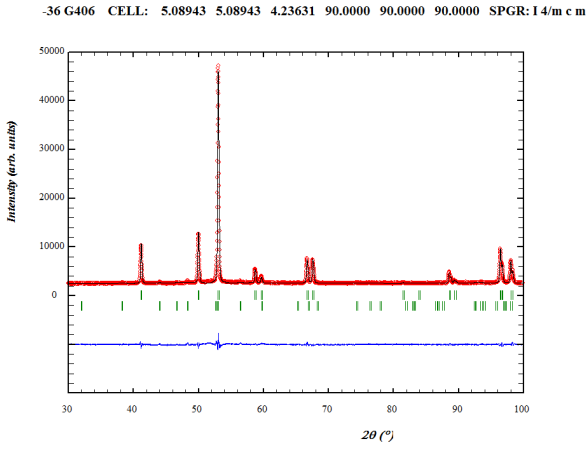

Figure 77: -36µm sample of G406.

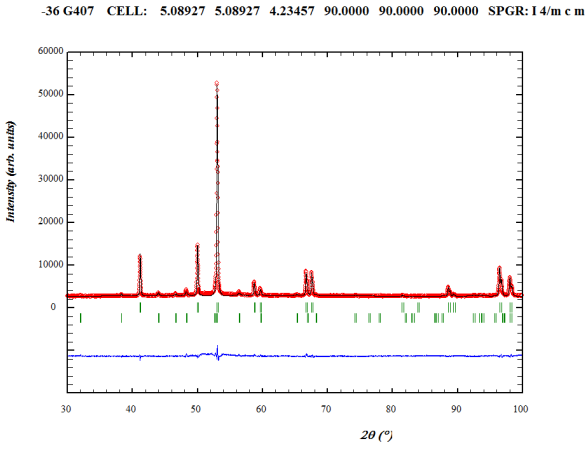

Figure 78: -36µm sample of G407.

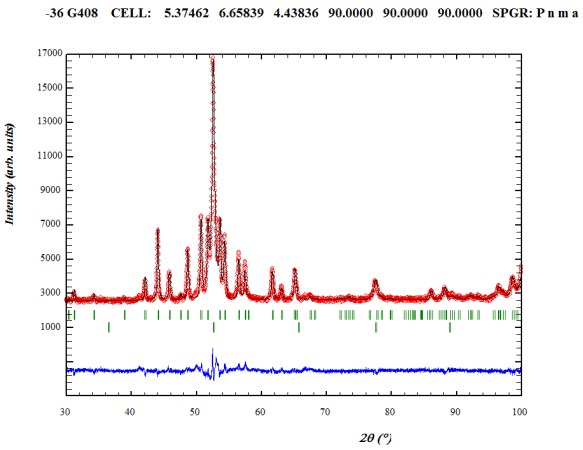

Figure 79: -36µm sample of G408.

G. VSM hysteresis plots

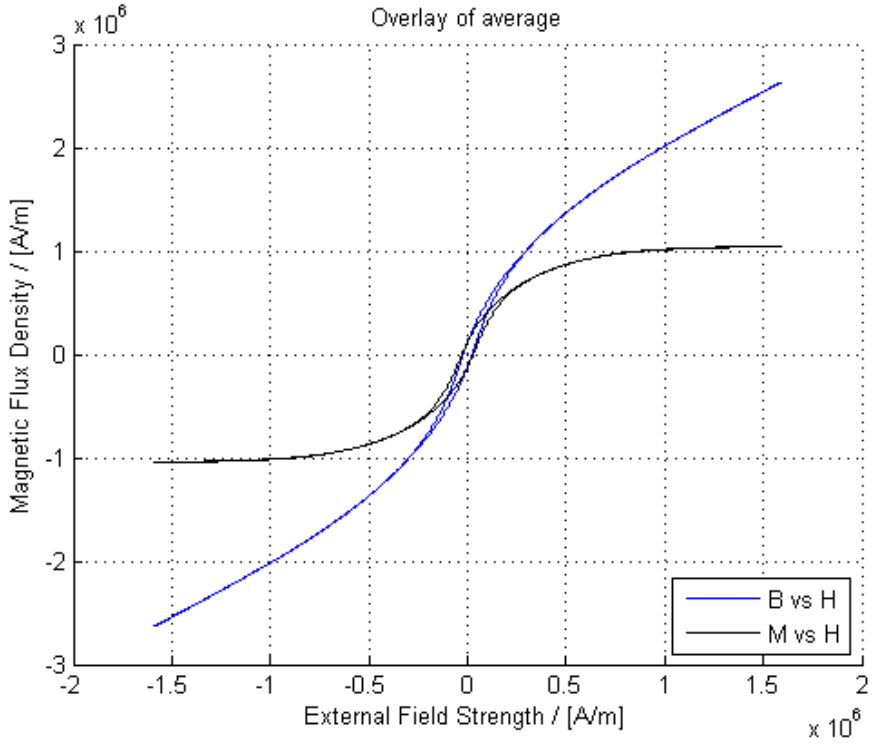

Figure 80: Hysteresis plot from VSM sample 1.

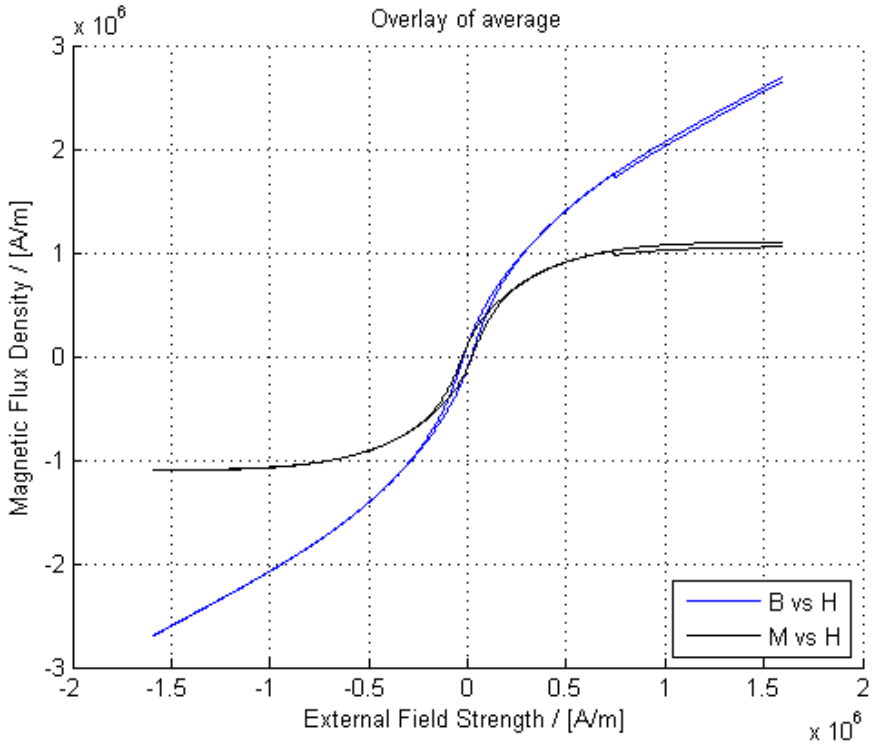

Figure 81: Hysteresis plot from VSM sample 2.

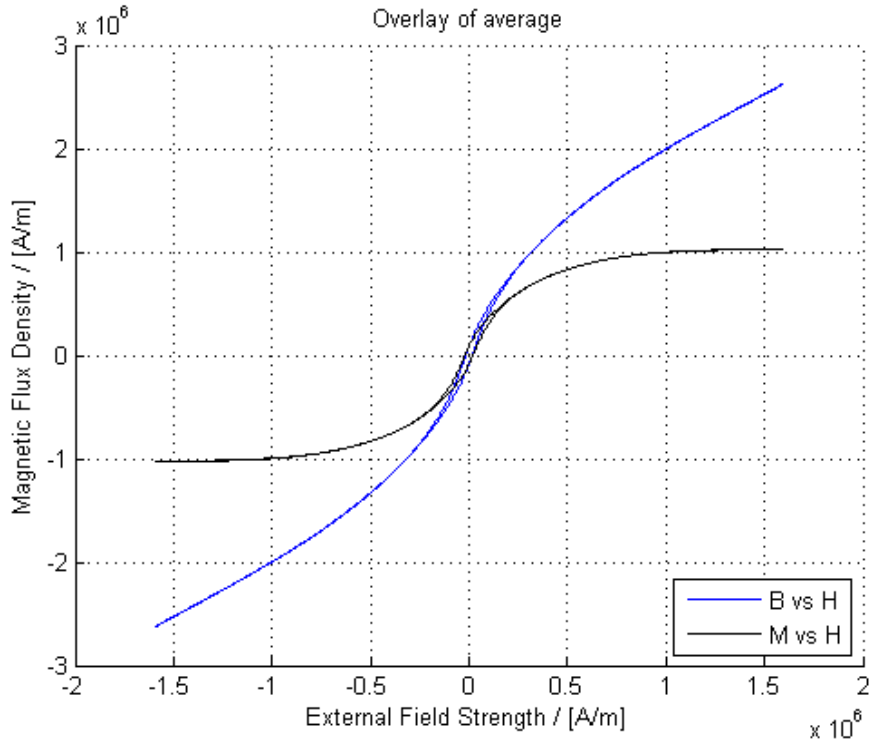

Figure 82: Hysteresis plot from VSM sample 3.

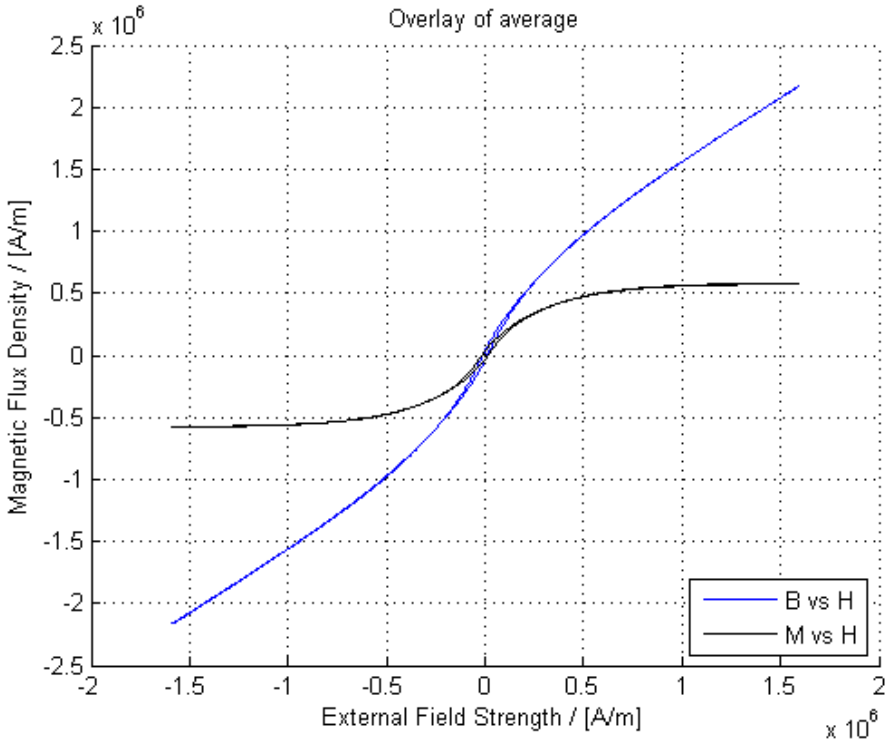

Figure 83: Hysteresis plot from VSM sample 4.

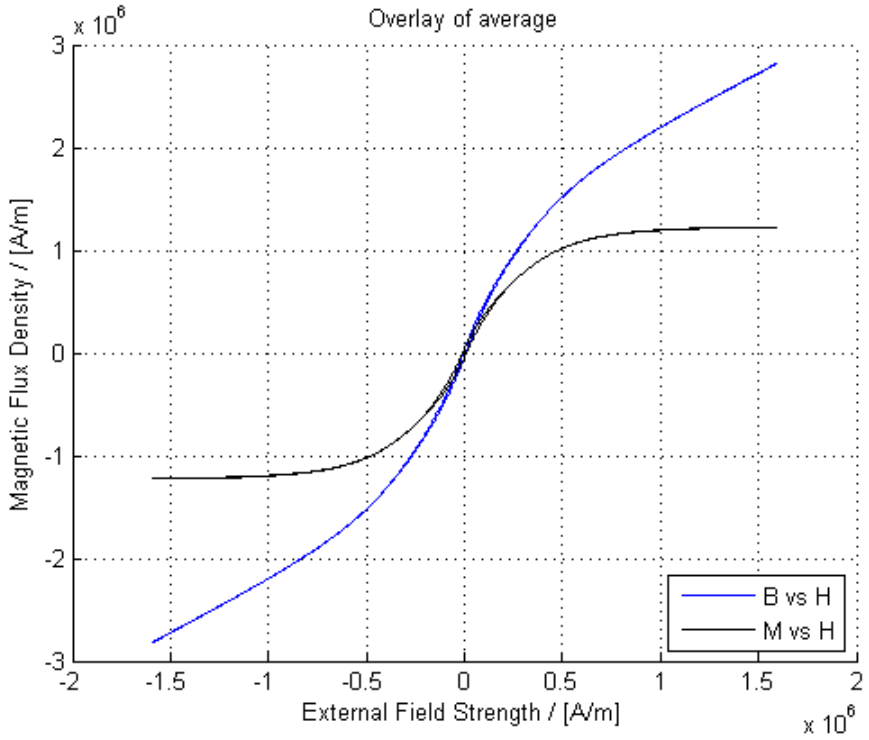

Figure 84: Hysteresis plot from VSM sample 5.

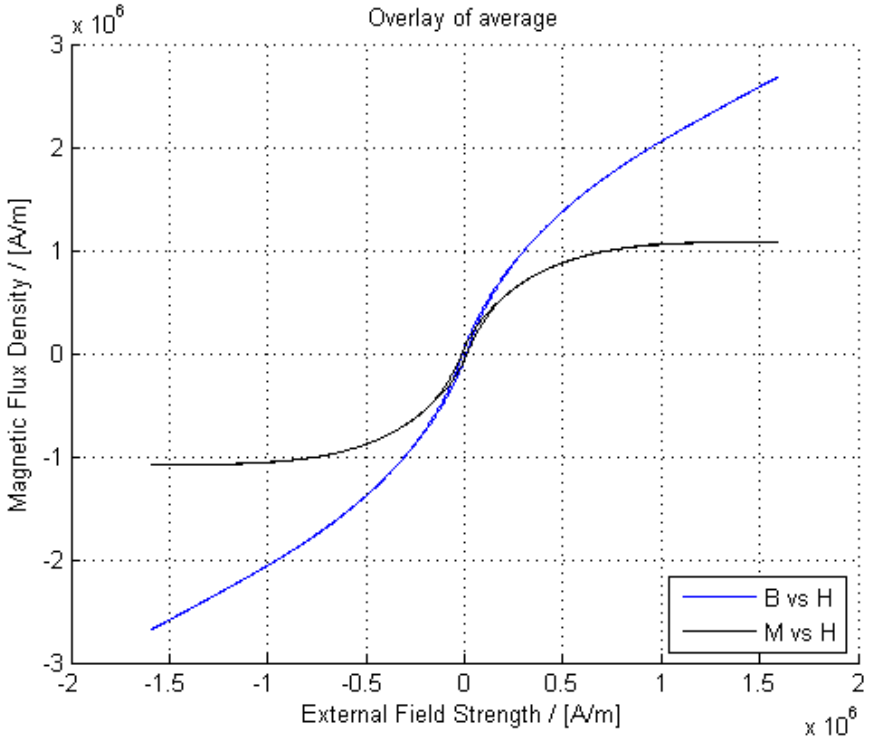

Figure 85: Hysteresis plot from VSM sample 6.

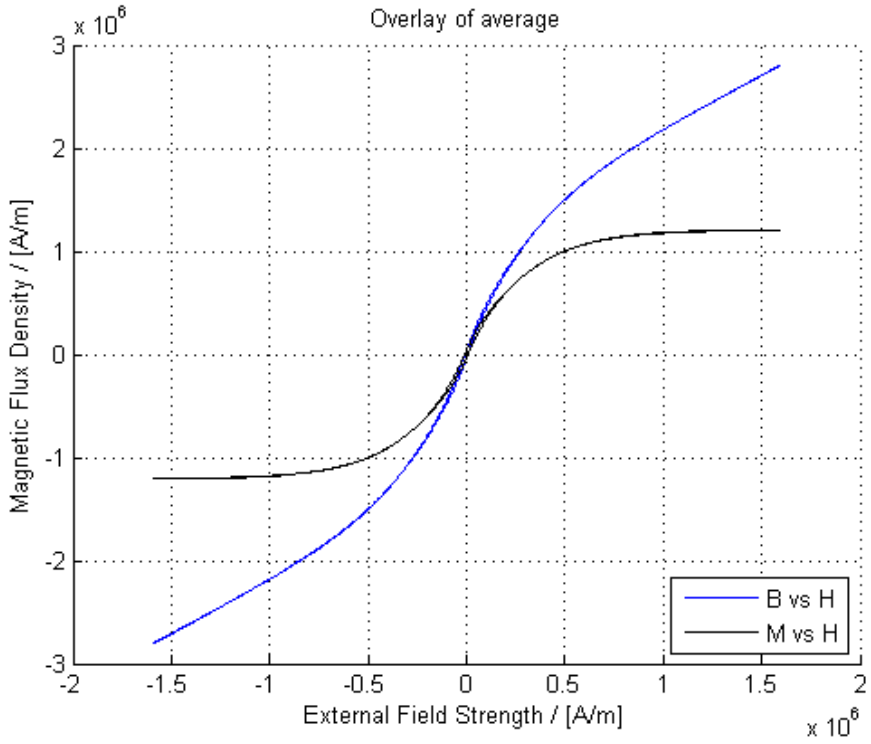

Figure 86: Hysteresis plot from VSM sample 7.

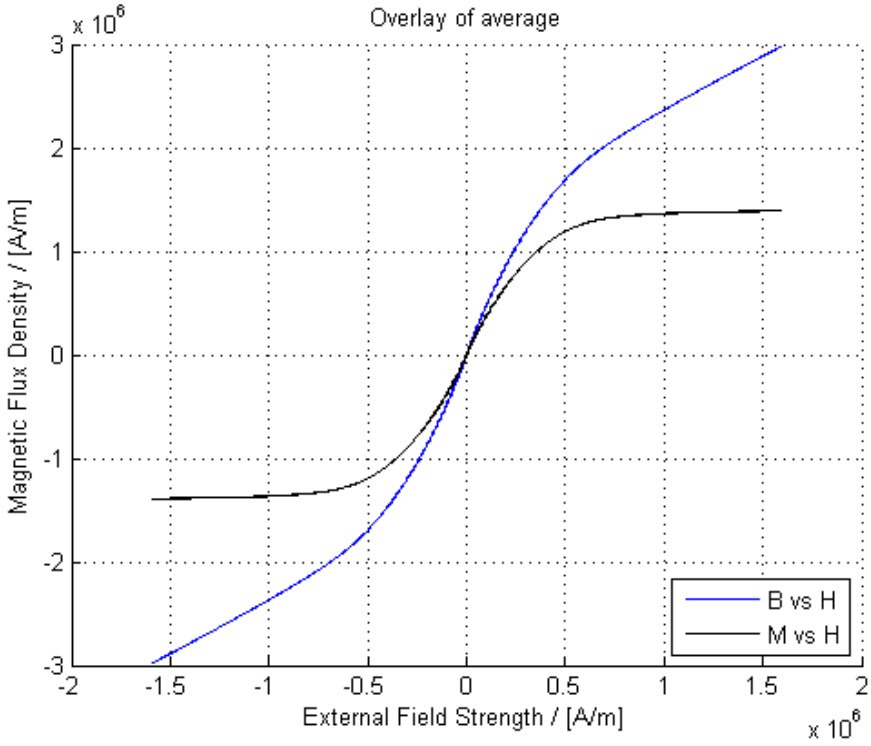

Figure 87: Hysteresis plot from VSM sample 8.

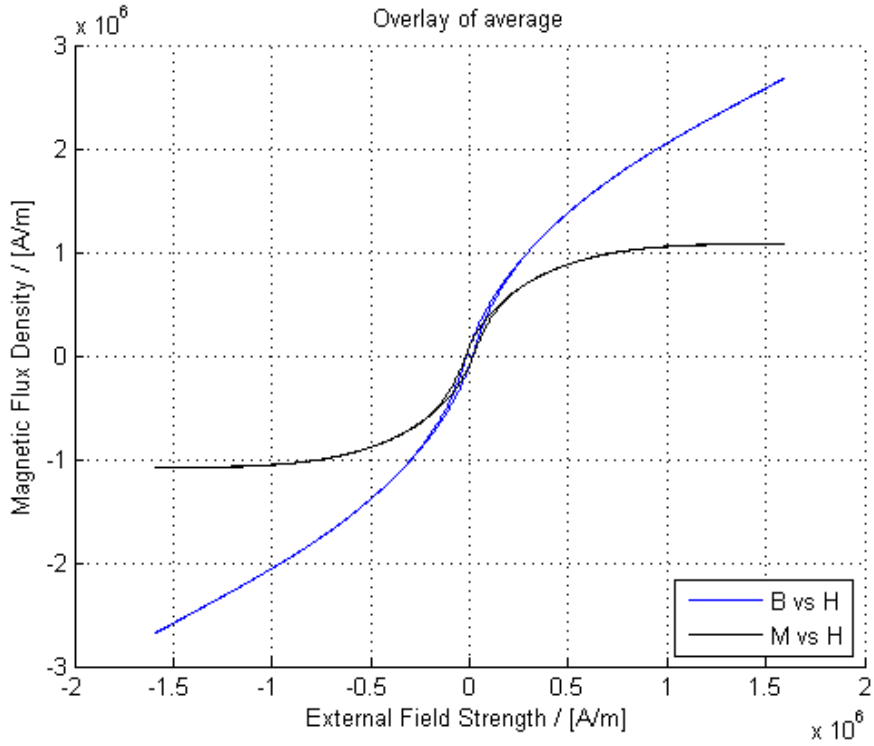

Figure 88: Hysteresis plot from VSM sample 9.

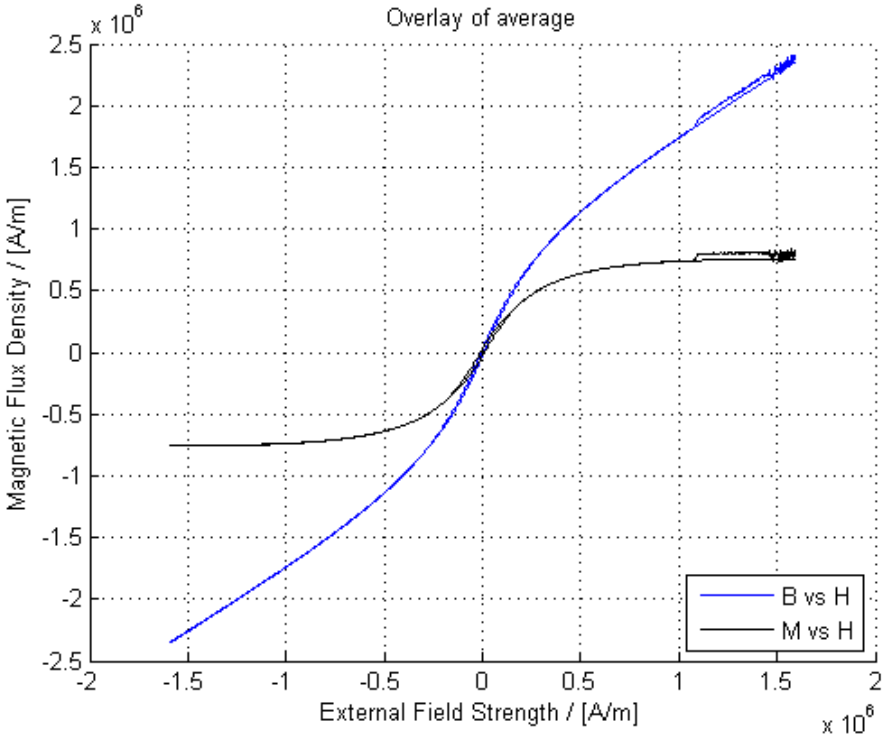

Figure 89: Hysteresis plot from VSM sample 10.

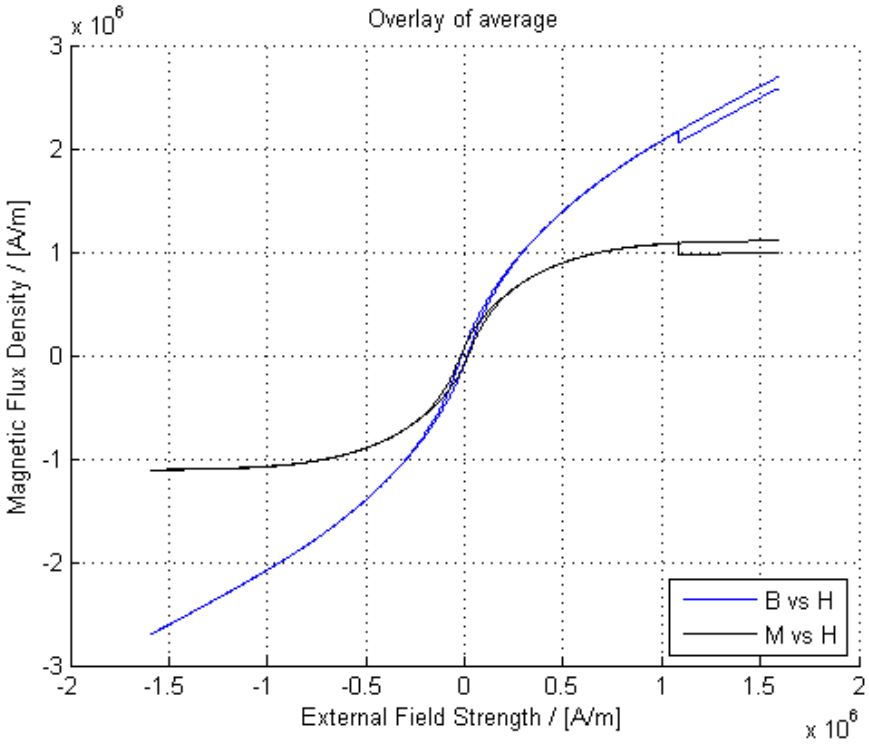

Figure 90: Hysteresis plot from VSM sample 11.

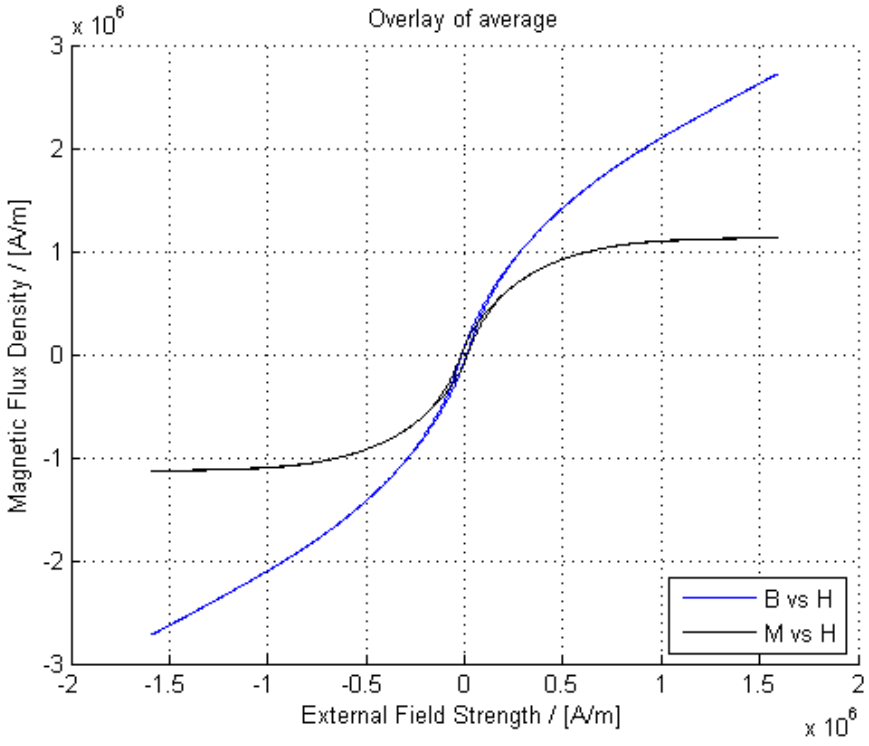

Figure 91: Hysteresis plot from VSM sample 12.

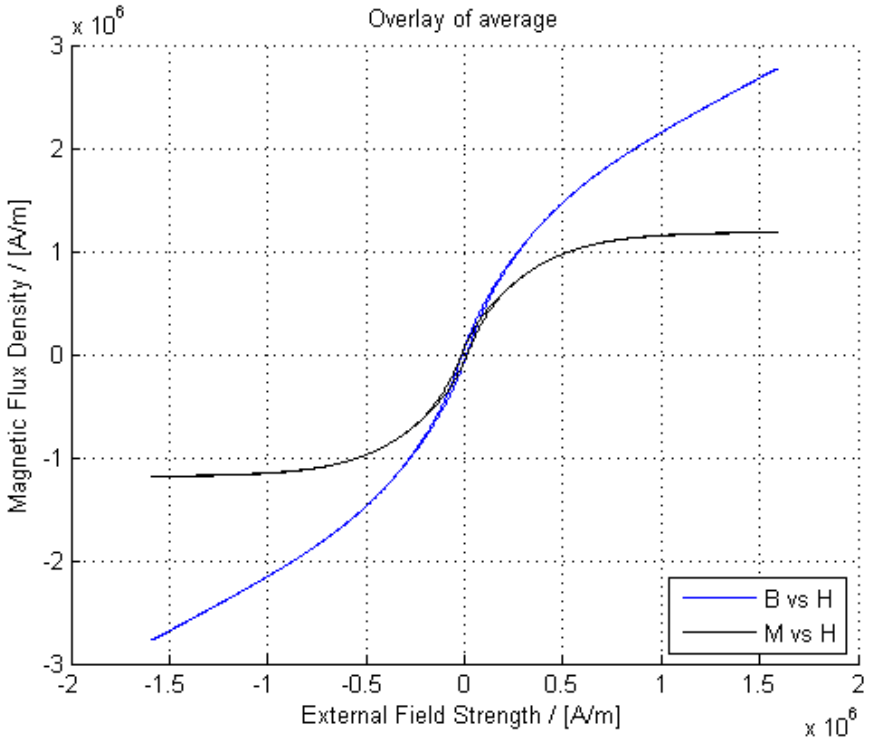

Figure 92: Hysteresis plot from VSM sample 13.

J. Derivation of equations

The following derivation is adapted from Coey [9], p. 467.

Equation 1 states that

$$B = \mu_0 (M + H)$$

and thus

$$BH = \mu_0 (M + H) H$$

Now, equation 4 states that, for H it holds that

$$H = -NM$$

and thus we find

$$BH = \mu_0 (M - NM) \cdot (-NM)$$

The demagnetizing factor *N* is, at best, 0.5. This yields

$$BH = \mu_0 \frac{M^2}{4}$$

As the maximum M is found at saturation we find

$$(BH)_{MAX} = \mu_0 \frac{{M_S}^2}{4}$$

□
